Electrostatic Microactuators Fabricated by Vertical Trench Isolation Technology

Edin Sarajlic

The research described in this thesis was carried out at the Transducers Science and Technology Group of the MESA$^+$ research institute, University of Twente, The Netherlands. It was performed within the framework of the STW project 'micro Scanning Probe Array Memory (μSPAM)'.

Promotiecommissie

Voorzitter:	prof.dr.ir. J van Amerongen	Universiteit Twente
Secretaris:	prof.dr.ir. A.J. Mouthaan	Universiteit Twente
Promotor:	prof.dr. M.C. Elwenspoek	Universiteit Twente
Assistent promotor:	Dr.ir. G.J.M. Krijnen	Universiteit Twente
Leden:	prof.dr. H. Fujita	University of Tokyo
	prof.dr. M. Gijs	EPFL Lausanne
	Dr.ir. L. Abelmann	Universiteit Twente
	prof.ir. H.M.J.R. Soemers	Universiteit Twente
	prof.dr.ir. J.B. Jonker	Universiteit Twente

CIP-GEGEVENS KONINKLIJKE BIBLITHEEK, DEN HAAG

Sarajlic, Edin
Electrostatic microactuators fabricated by vertical trench isolation technology
Ph.D. Thesis, University of Twente, Enschede, The Netherlands

ISBN 90-365-2212-9

Print: Wöhrmann Print Service, Zutphen, The Netherlands

ELECTROSTATIC MICROACTUATORS FABRICATED BY VERTICAL TRENCH ISOLATION TECHNOLOGY

PROEFSCHRIFT

ter verkrijging van
de graad van doctor aan de Universiteit Twente,
op gezag van de rector magnificus,
prof.dr. W.H.M. Zijm,
volgens het besluit van het College voor Promoties
in het openbaar te verdedigen
op vrijdag 13 mei 2005 om 16.45 uur

door

Edin Sarajlic
geboren op 5 april 1970
te Tuzla

Dit proefschrift is goedgekeurd door de promotor:

prof.dr. M.C. Elwenspoek

en de assistent promotor:

Dr.ir. G.J.M. Krijnen

Voor Lamia en Aida

Contents

Chapter 1

Introduction

Abstract

The research described in this thesis is focused on the development of microactuators, which are required for fast and accurate positioning of a recording medium in a new magnetic memory based on scanning probe technology, so called micro Scanning Probe Array Memory (μSPAM). In this chapter, the μSPAM concept is briefly introduced and the preliminary target specifications for positioning of the recording medium are given. A survey of electrostatic micromotors based on the stepping motion, which we believe are promising candidates to perform this demanding positioning task, is given. A general idea behind vertical trench isolation is briefly described. This advanced silicon micromachining technique is thoroughly explored in this thesis as an attractive platform for fabrication of electrostatic microactuators. At the end of this introductory chapter, a complete outline of the thesis is given.

1.1 GENERAL INTRODUCTION

The research described in this thesis focuses on the development of high performance microactuators characterized by large output force (mN range), large stroke (hundreds of μm's), high resolution (nm range), high speed (mm/s range) and low power consumption. Possible applications of microactuators with such unprecedented performance characteristics are numerous and include data storage, microassembly, microscopy, robotics and optical systems. In this work we are primarily concerned with application of these microactuators for fast and accurate positioning of a recording medium in a probe-based data storage system.

In our opinion, a microactuator design that is highly suitable for probe-based data storage application is the *electrostatic linear stepper micromotor with a built-in mechanical leverage*. This type of a microactuator utilizes electrostatic actuation, which is an attractive driving principle at micro scale due to advantageous scaling, low power consumption and fast response. A large displacement range is obtained by adding small steps in sequence using the stepping motion. Additionally, a built-in mechanical leverage is employed to produce high-resolution motion in combination with a large output force.

In general, the feasibility and performance of microactuators are associated with the possibilities and limitations of available microfabrication methods. Therefore, great attention in this thesis is given to the development of novel micromachining techniques suitable for the fabrication of electrostatic microactuators. The micromachining methods developed and used in this work are mostly based on *vertical trench isolation*. The vertical trench isolation employs trenches refilled with dielectric material to create, in a single conductive layer, electrical insulation between mechanically joined components. This sophisticated electrical insulation allows the simplification of fabrication and design of entirely new types of microactuators, as well as the improvement in performance of the existing ones.

In this introductory chapter, preliminary target specifications are presented for microactuators intended for positioning of a recording medium in a probe-based data storage system. Furthermore, a survey of electrostatic linear stepper

micromotors and a brief introduction to the vertical trench isolation are given. The chapter ends with a complete outline of the thesis.

1.2 MICRO SCANNING PROBE ARRAY MEMORY (µSPAM)

Performance goals chosen for our microactuators are motivated by their potential use in magnetic memory based on scanning probe technology, which is currently in development at the MESA$^+$ Research Institute [1,2]. The memory, named micro Scanning Probe Array Memory (µSPAM), will combine high storage capacity with low power consumption and small size. The µSPAM concept is schematically illustrated in Figure 1.1.

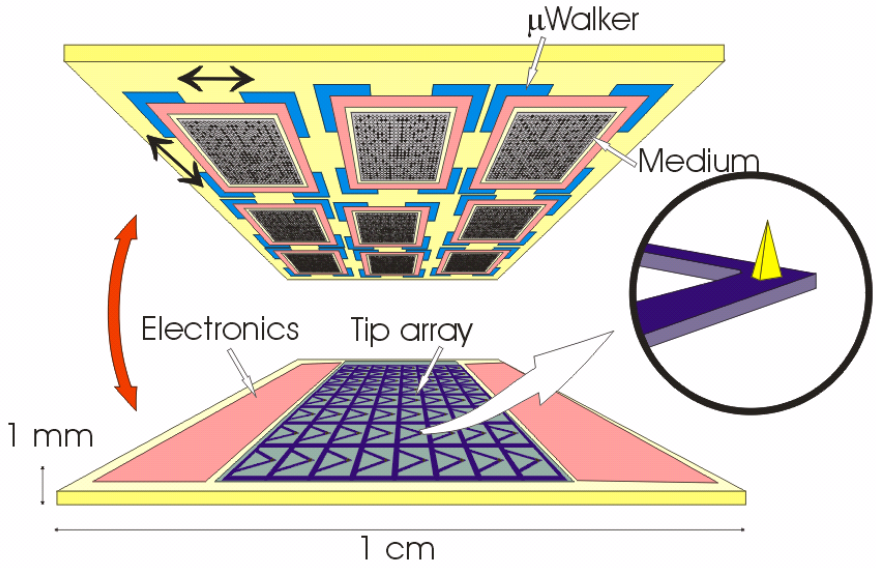

Figure 1.1: Micro Scanning Probe Array Memory (µSPAM) concept (courtesy of L. Abelmann and M. Bolks).

The basic principle behind µSPAM is to access the recording magnetic medium located on a movable tile with a stationary array of a large number of micromechanical probes by positioning the medium tile in two translational directions. In contrast to other groups working in the probe storage field [3-5], a large number of medium tiles with an integrated positioner is employed to increase concurrency and reduce power consumption. An 8 x 8 tile configuration with a total area of 1 cm x 1 cm is used. The area, occupied by a single tile, is approximately 1 mm x 1 mm.

A successful implementation of the μSPAM concept requires a large number of small positioners capable of two-axis planar motion with demanding performance characteristics. Target specifications for a medium positioner are summarized in Table 1.1.

Table 1.1: Preliminary target specifications of a medium positioner designated for the micro Scanning Probe Based Memory.

Parameter	Value
Available area	1 mm x 1 mm
Displacement range	± 50 μm in X, ± 50 μm in Y
Resolution	<100 nm
Speed (read/write)	>1 mm/s
Seek speed	>40 mm/s
Force	1 mN

The small dimensions of a medium tile impose limitations on the size of the positioners. A positioner should be completely placed underneath the medium tile to increase the effective recording area. In the μSPAM concept, only a small area of approximately 1 mm x 1 mm is available for the placement of a complete positioner. The positioner should move the medium tile at least ± 50 μm in both X and Y directions. The area of 100 μm x 100 μm is the scanning range of each individual micromechanical probe. This scanning range must be covered with a resolution better than 100 nm, in order to access densely packed magnetic bits. Hence, positioners with a large dynamic range (> 1000), which is the ratio between displacement range and resolution, are needed. Assuming a data rate of 10 kbits/s per probe and 100 nm pitched magnetic bits [2] a positioning speed higher than 1 mm/s is required during reading and writing of data. In order to reduce the access time (< 2.5 ms) the seek speed should be over 40 mm/s. Furthermore a relative large force is desired to allow large acceleration of the medium tile making the positioning system fast, insensitive for the earth gravitation and more shock tolerant. A preliminary target specification is set to 1 mN, corresponding to the force necessary to accelerate a 1mg tile (approximately 1 mm x 1 mm x 0.5 mm tile made of silicon) with 100g (~ 1000 m/s^2).

Considering the required large number of positioners and the small available area per positioner, microactuators fabricated by micromachining technology are a logical choice for positioning of the recording medium in the μSPAM.

1.3 ELECTROSTATIC LINEAR STEPPER MICROMOTORS

A microactuator is a small-scale device fabricated by micromachining technology, which transforms non-mechanical energy into mechanical energy. Many types of microactuators have been suggested and successfully developed. An extensive survey on microactuators is given in the literature [6-8].

Microactuators employ diverse actuation principles according to the requirements of particular applications. A widely applied principle on the micrometer scale is electrostatic actuation. Electrostatic actuation is an attractive principle for microactuators because electrostatic forces scale favourably [9-11]. In general, the energy density of an electrostatic actuator increases as the size of the actuator is reduced. Furthermore, the breakdown strength of air increases with decreasing gap separation allowing large electric fields between electrodes. These large electric fields enable electrostatic motors with energy densities comparable with that in conventional magnetostatic motors. Additionally, electrostatic microactuators are essentially voltage driven. Fast voltage switching in combination with a small actuator size allows fast response and low power consumption. Finally, one of the most important reasons behind the widespread use of electrostatic microactuators is their compatibility with silicon micromachining methods.

A large electric field achievable in narrows gaps allows realization of electrostatic microactuators with relative large output force [12]. However, a large electric field drops off quickly by increasing the spacing between electrodes, which limits the displacement range of electrostatic microactuators with large output force. Consequently, electrostatic microactuators with a large displacement range, e.g. comb drives [13], generally produce a low output force.

Electrostatic linear micromotors based on stepping motion [14-17] are a solution for generating both a relatively large output force and a relatively large displacement range. These micromotors employ a large force, short stroke microactuator to produce a small step and a clamping mechanism to add small steps in sequence, thereby creating large displacements. The theoretical unlimited

displacement range of these micromotors is in practice restricted by the dimension of the guidance. The clamping and the propulsion are separated in stepper micromotors, allowing an individual optimisation of these two mechanisms. Accordingly, more accurate positioning, higher reliability and larger output force are expected for stepper motors compared with other stepping motion micromotors such as scratch drives, inertial drives and impact micromotors (see [18] for a complete overview of different stepping motion micromotors). These advantages of stepper micromotors come at the expense of increased complexity of the driving signal.

First electrostatic linear stepper micromotors [14-16] were realized using the conventional surface micromachining process. The clamping and the propulsion mechanism of these micromotors remained stationary and only a movable shuttle was displaced during the operation. Arrays of electrostatic gap-closing actuators were used for the propulsion. The clamping was achieved by applying a voltage difference between the active clamp and the shuttle [14] or by employing separate clamp actuators [15,16]. The maximum output force of few μN and maximum displacement range of tens of μm were demonstrated with these motors.

An improved electrostatic stepper micromotor employing high-aspect-ratio gap-closing actuators [17] was created in monocrystalline silicon using Silicon On Insulator (SOI) micromachining. A maximum force of 260 μN at 33 V and a travel range of 80 μm were demonstrated with micromotor measuring 3 mm x 1 mm. A maximum speed of 4 mm/s, corresponding with a cycling frequency of 1kHz and an average step size of 4 μm, was reported. The motor was driven over 23.6 million cycles without any performance deterioration. However, a further performance improvement of this micromotor in terms of larger output force per area and higher stepping resolution necessary for μSPAM would require a downscaling that is far beyond the capabilities of two-micron lithography.

An electrostatic linear stepper micromotor with a built-in mechanical leverage is an alternative approach to generate both a large output force in a small area and a high positioning resolution [18, 19]. This, so called, shuffle motor converts normal deflection of an elastic plate into a small powerful step. Two electrostatic clamps are employed to enable bidirectional stepping motion. The shuffle motor performs a walking motion, in which both the clamps and the propulsion

mechanisms are moved around. A prototype of the shuffle motor was successfully driven at 0.1 mm/s corresponding with a maximum stepping frequency of 1.16 kHz and an average step size of 85 nm. The maximum cycling frequency was limited by the drive electronics. At a plate voltage of 25 V and a clamp voltage of 40 V, an output force of 43 μN was achieved, which is much lower than the theoretically predicted force of 0.6 mN. This discrepancy was attributed to the use of modulated AC-voltage actuation, which was necessary in order to avoid motor failure by charging effects (on the plate and clamps).

In the brief overview, presented above, the feasibility of stepping motion on the micro scale was demonstrated. At the same time, it shows that it is rather challenging to realize a micromotor with high performance characteristics as required for the medium positioning in a μSPAM. In this thesis, we propose and investigate different electrostatic linear stepper micromotors with a built-in mechanical leverage, which are in our opinion the most promising candidates to perform this positioning task. In addition to design considerations, special attention is given to the development of appropriate microfabrication methods.

1.4 VERTICAL TRENCH ISOLATION

Electrostatic microactuators utilize the electrostatic force between stationary and movable mechanical structures with dimensions and separations in the micrometer or even sub-micrometer range. A practical realization of electrostatic microactuators requires microfabrication methods that allow an effective electrical insulation between microstructures, which are mechanically linked by rigid or flexible connections.

A departure from the in conventional surface micromachining [20] widely used approach of stacking of multiple dielectric and conductive layers connected by vertical conduction parts is the use of vertical trench isolation. Vertical trench isolation, schematically shown in Fig. 1.2, employs trenches refilled with dielectric and/or poor conducting materials to create electrical insulation between mechanically connected parts in a single conductive layer.

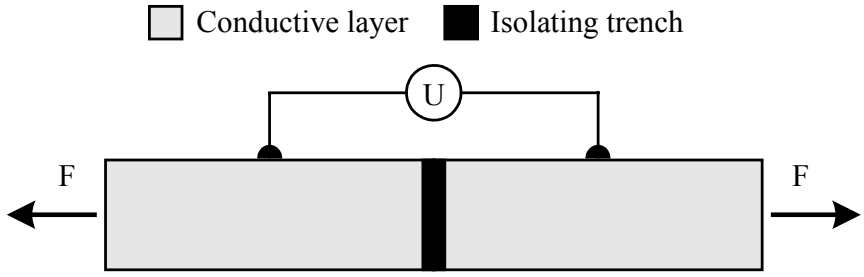

Figure 1.2: An isolating trench refilled with dielectric material assures both electrical insulation and mechanical integrity.

Vertical trench isolation was initially developed for the fabrication of high-aspect-ratio monocrystalline accelerometers and their full integration with on-chip electronics [21, 22]. Several important features of isolating trenches are recognized. Isolating trenches can serve as:

- electrical insulation between microstructures and the on-chip electronics as well as isolation between individual microstructures;
- lateral anchoring of microstructures;
- mechanical support for embedded interconnects connecting microstructures with on-chip electronics;

These advanced features make vertical trench isolation an attractive technology platform for the fabrication of microelectromechanical systems (MEMS).

In this thesis we further explore the use of vertical trench isolation for MEMS fabrication, specifically the fabrication of electrostatic microactuators. In particular, we are intrigued by the possibility of creating multiple electrical domains on movable micromechanical parts. Electrical isolation on the movable parts allows simplification of fabrication and improvement of the performance of existing electrostatic microactuators and design of entirely new devices.

1.5 THESIS OUTLINE

The research presented in this thesis is focused on the development of microactuators, which are required for fast and accurate positioning of a recording medium in a probe-based data storage system. Electrostatic linear stepper micromotors with a built-in mechanical leverage are investigated as potential candidates to perform this demanding positioning task, which is far beyond the

reach of most microactuators. In order to allow the fabrication of microactuators with significantly improved performance characteristics emphasis is given on the development of new micromachining methods, which are mainly based on vertical trench isolation.

In the following a chapter-by-chapter overview of the thesis is given.

In **Chapter 2** we explore the use of trench isolation in surface and SOI-based micromachining. By adding extra features to a basic trench isolation process new design opportunities are created.

In **Chapter 3** we present a bulk micromachining method based on a combination of vertical trench isolation and plasma release, which allows the fabrication of high aspect ratio MEMS in standard monocrystalline silicon wafers.

In **Chapter 4** we report on a bulk micromachining technology that employs a backside etch to release micromechanical structures with integrated vertical trench isolation, allowing the fabrication of high aspect ratio, monocrystalline structures with a large non-perforated area in a low-cost standard silicon wafer.

In **Chapter 5** we present a bulk micromachining technology, based on vertical trench isolation, for fabrication of two-level MEMS in a standard monocrystalline silicon substrate.

In **Chapter 6** we introduce a selective refill method which allows *single-mask* fabrication of high-aspect-ratio MEMS with integrated vertical trench isolation in standard monocrystalline silicon or in SOI substrates.

In **Chapter 7** we describe a simple parallel processing method, fully compatible with standard micromachining, for fabrication of addressable three-dimensional (3D) nanometer-sized structures, such as wires, wire frames and dots.

In **Chapter 8** we report on a bidirectional electrostatic linear stepper motor with the high overall performance characteristics, and the highest force and power densities ever published so far for electrostatic microactuators.

In **Chapter 9** we present the first electrostatic linear stepper micromotor with two translational degrees-of-freedom.

In **Chapter 10** we introduce an electrostatic linear stepper micromotor, which employs both a built-in mechanical transformation and a large number of contraction beams working in parallel to generate a large output force and high-resolution step.

In **Chapter 11** we draw general conclusions and give recommendations for the future work.

1.6 REFERENCES

1 Abelmann L and Lodder C 1999 Probe recording, arrays and self-assembly *MESA+ Internal Report* University of Twente, The Netherlands

2 Bolks M et al 2001 Micro Scanning Probe Array Memory (μSPAM) *Proc. 2nd PROGRESS workshop* (Utrecht, The Netherlands)

3 Vettiger P et al 1999 Ultrahigh density, high-data-rate NEMS-based AFM data storage system *Microelect. Eng.* **46** 11-17

4 Carley L R et al 2000 Single-chip computers with microelectromechanical systems-based magnetic memory *J. of Applied Physics* **87** 6680-5

5 Kim C H, Jeong H M, Jeon J U and Kim Y K 2003 Silicon micro XY-stage with a large area shuttle and no etching holes for SPM-based data storage *J. Microelectormech. Syst.* **12**(4) 470-478

6 Dario P, Valleggi R, Carozza M C, Montesi M C and Cocco M 1992 Microactuators for Microrobots: a critical survey *J. Micromech. Microeng.* **2** 141-157

7 Fujita H 1998 Microactuators and micromachines *Proceedings of the IEEE* **86**(8) 1721-1732

8 Thielicke E and Obermeier E 2000 Microactuators and their technologies *Mechatronics* **10** 431-455

9 Fujita H and Omodaka A 1987 Electrostatic actuators for micromechatronics *Proceedings IEEE Micro robots and Teleoperators Workshop* (Hyannis, USA)

10 Lang J H, Schlecht M F and Howe R T 1987 Electric micromotors: electromechanical characteristics *Proceedings IEEE Micro robots and Teleoperators Workshop* (Hyannis, USA)

11 Trimmer W 1989 Microrobots and micromechanical systems *Sensors Actuators* A **19**(3) 267-287

12 Fearing R S 1998 Powering 3 dimensional microrobots: Power density limitations *Tutorial on Micro Mechatronics and Micro Robotic*, ICRA

13 Tang W C, Lim M G and Howe R T 1989 Laterally driven polysilicon resonant microstructures *Proceedings IEEE Micro Electro Mechanical Systems* 53-59

14 Yeh R, Kruglick E J J and Pister K S J 1996 Surface-micromachined components for articulated microrobots *J. Microelectormech. Syst.* **5**(1) 10-17

15 Tas N R, Sonnenberg A H, Sander A F M and Elwenspoek M 1997 *Proc. IEEE Workshop on Micro Electro Mechanical* Systems (Nagoya, Japan) pp 216-220

16 Baltzer M, Kraus T and Obermeir E 1997 A linear stepping actuator in surface micromachining technology for low voltages and large displacements *Int. Conf. on Solid State Sensors and Actuators* (TRANSDUCERS 97) (Yokohama, Japan) 781-784

17 Yeh R, S Hollar and Pister K S J 2001 Single-mask, large force and large displacement electrostatic linear inchworm motors *Int. Conf. on Micro Electro Mechanical Systems* (MEMS 2001) (Interlaken, Switzerland) 260-264

18 Tas N 2000 Electrostatic Micro Walkers *PhD Thesis* (University of Twente, The Netherlands) ISBN 90-36514355

19 Tas N, Wissink J, Sander L, Lammerink T and Elwenspoek M 1998 Modeling, design and testing of the electrostatic shuffle motor *Sensors Actuators* A **70**(3) 171-178

20 Bustillo J M, Howe R T and Muller R S 1998 Surface micromachining for microelectromechanical systems *Proceedings of the* IEEE **86**(8) 1552-1574

21 Brosnihan T J 1998 An SOI based, fully integrated fabrication process for high-aspect-ratio microelectromechanical systems *PhD Thesis* Department Of Mechanical Engineering (University of California, USA)

22 Brosnihan T J, Bustillo J M, Pisano A P and Howe R T 1997 Embedded interconnect and electrical isolation for high-aspect-ratio, SOI inertial instruments *Int. Conf. on Solid State Sensors and Actuators* (TRANSDUCERS 97) (Chicago, USA) 637-640

Chapter 2

Vertical trench isolation for surface and SOI-based micromachining

Abstract

Vertical trench isolation employs trenches refilled with dielectric material to create electrical insulation between mechanically joined components in a single conductive layer. This chapter explores the use of trench isolation in surface and SOI-based micromachining for advanced MEMS fabrication, particularly the fabrication of electrostatic microactuators. By adding extra features to a basic trench isolation process new design opportunities, like isolation structures and isolating bumps, are created. The isolation structures can be employed as flexible or rigid connections between movable or fixed components or can serve to prevent the short-circuiting by maintaining the end distance between movable electrodes. The isolating bumps reduce stiction during release and operation, prevent short-circuiting due to an out-of-plane displacement and can serve as etch holes at the same time. The trench isolation technology is demonstrated in a fabrication process of an actuator consisting of a large number of elastic electrodes connected in parallel and in series and by a novel low volume, large force (> 1 mN) and nanometer resolution electrostatic actuator for low displacement applications.

2.1 INTRODUCTION

Microelectromechanical systems (MEMS) often require electrical isolation between mechanically interconnected structures implemented within a minimum number of layers and processing steps. A departure from the conventional surface micromachining approach [1] of stacking of multiple dielectric and conductive layers connected by vertical conduction paths is the use of vertical trench isolation.

Vertical trench isolation employs trenches refilled with dielectric or poor conducting materials to create electrical insulation between mechanically connected microstructures in a single conductive layer. In this way, distinct electrical domains can be created on fixed and even on movable micromechanical parts.

Trench isolation was for the first time used in a CMOS-compatible micromachining process for fabrication of single-crystal-silicon inertial sensors [2,3]. This process, based on Silicon On Insulator (SOI) substrates, has allowed fabrication of high-aspect-ratio accelerometers and its full integration with on-chip electronics through embedded interconnects. A fully integrated, single chip accelerometer [4], manufactured using the SOI-based trench isolation technology, has demonstrated improved sensitivity, an order of magnitude better than similar accelerometers fabricated by surface micromachining technology.

The SOI-based trench isolation technology, initially developed for fabrication of inertial sensors, is also highly suitable for other types of MEMS. A resonantly excited 2D micro scanning mirror [5] is successfully realized using this technology.

In this chapter we further explore the use of vertical trench isolation for MEMS fabrication with emphasis on fabrication of electrostatic microactuators. Important design and processing issues for successful fabrication of released micromechanical structures with integrated vertical trench isolation are discussed. Starting with a basic two-mask trench isolation process (Fig. 2.1), as suggested by Brosnihan [2], new design features are added while the fabrication process stays virtually unchanged. These additions make the trench isolation technology an even more attractive technology platform for MEMS fabrication allowing large freedom

of design. As a demonstration of the capabilities of the technology, an electrostatic micro-actuator consisting of a large number of elastic electrodes connected in parallel and in series [6-8], to produce large forces and large displacement was successfully fabricated and operated. Furthermore, a novel electrostatic actuator for low displacement and large force applications is presented proving the large innovation potential of the trench isolation technology.

2.2 VERTICAL TRENCH ISOLATION TECHNOLOGY

The fabrication steps of a basic trench isolation process are shown in Fig. 2.1.

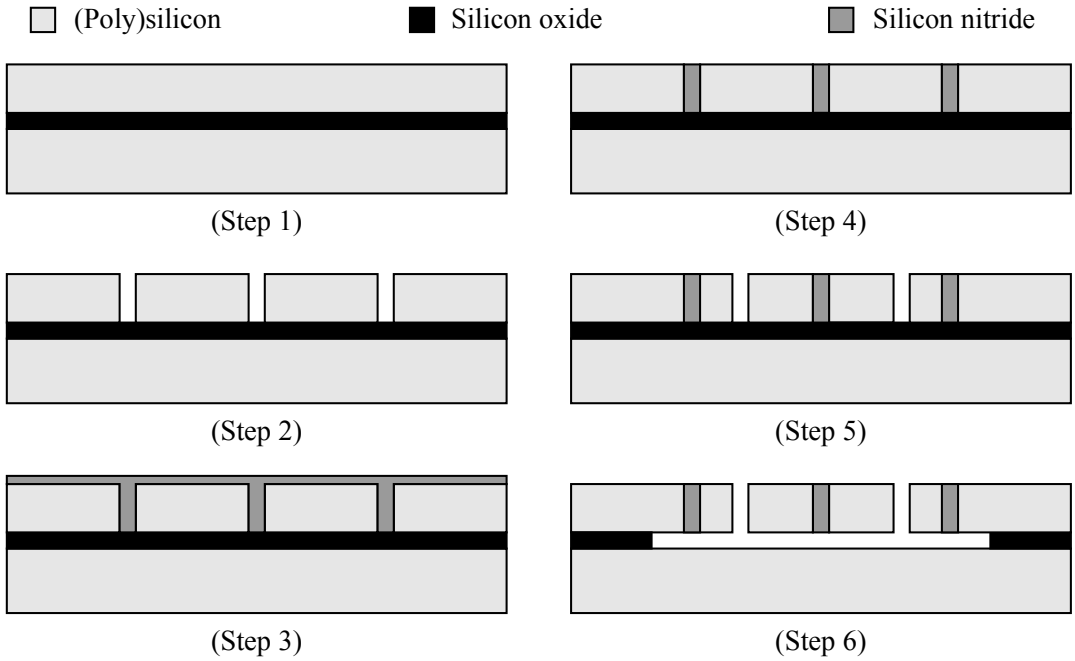

Figure 2.1: A basic trench isolation process for fabrication of mechanical coupled/electrical isolated microstructures.

The two-mask fabrication process starts on a wafer with a doped (poly)silicon device layer on the top of the sacrificial silicon oxide layer (*Step 1*). Use of an SOI wafer allows for high aspect ratios monocrystalline silicon structures, truly valuable in some applications. However, it is worth mentioning that one is not limited to SOI micromachining. The basic trench isolation process can also be

employed as a part of a more complex surface micromachining sequence such as the one used for fabrication of electrostatic stepper micromotors in Chapter 8.

In the next fabrication step, Deep Reactive Ion Etching (DRIE) is employed to define isolating trenches in the conductive device layer (*Step 2*). The silicon oxide layer, which has a high etch selectivity to (poly)silicon, serves as etch stop. Subsequently, a low stress silicon nitride layer is deposited on the patterned surface using Low Pressure Chemical Vapour Deposition (LPCVD) (*Step 3*). The isolating trenches are completely refilled with the deposited material. Silicon nitride is used as a refill material because of favourable electrical insulating properties and highly conformal deposition. Furthermore, silicon nitride has a low etch rate in aqueous hydrofluoric acid (HF), which is commonly employed to dissolve sacrificial silicon oxide in order to release microstructures. The deposited silicon nitride layer is removed from the top surface by a maskless RIE using CHF_3 plasma chemistry (*Step 4*). The deposited material in the refilled trenches is preserved. The removal process leaves a flat surface profile, which allows further processing including a potential integration of electronic circuits [2-4]. In a second DRIE step, the structural layout is defined (*Step 5*). Finally, microstructures are released by dissolving the sacrificial oxide layer using HF or buffered HF (BHF) etch solutions (*Step 6*). This two-mask fabrication process allows fabrication of released structures mechanically connected and electrically separated by a refilled isolation trench. Large fracture strength and high electrical resistance are reported [2] between test components connected by an isolating trench refilled with silicon nitride.

2.3 DESIGN AND PROCESSING ISSUES

2.3.1 Isolation layout

A trench refilled with an isolating material creates electrical insulation between microstructures and at the same time assures mechanical integrity. Microstructures, which are mechanically connected with rigid or even flexible connections, can be easily mutually electrically insulated in this way. Distinct electrical domains can be achieved even on movable parts opening new design opportunities.

Trench isolation requires a small wafer area due to its vertical nature. Isolating trenches can be arranged into two basic configurations, which are illustrated in Fig. 2.2.

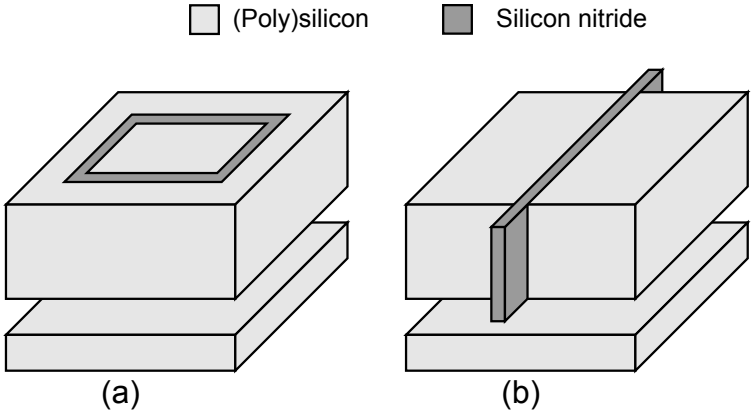

Figure 2.2: Two basic trench configurations: (a) An insulated material island, (b) A conductive part divided into two electrically separated regions.

In the first configuration, a refilled trench encloses a complete region creating an electrically insulated material island in a conductive part. In the second configuration, an isolating trench divides a conductive part into two electrically separated regions. The length of the isolating trench, in the second configuration, must be larger than the width of the part in order to compensate for possible mask misalignments. A protruding part of the isolating trench is fully exposed to the etch plasma during the structural etching step (*Step 5*). This results in a complete removal of the silicon around the refilled trench creating a reliable electrical isolation.

2.3.2 Trench etching and refill

Once an isolation layout is chosen, a trench etching (*Step 2*) followed by an appropriate trench refill (*Step 3*) has to be performed. Deep trenches with a perfectly vertical etch profile are preferred to allow a voidless trench refill and complete removal of the (poly)silicon from the sidewalls of the refilled trenches [2]. Large deviations, both positive and negative, from the perfectly vertical trench profile result in an undesirable deterioration of electrical or mechanical properties of the trench isolation, as illustrated in Fig. 2.3.

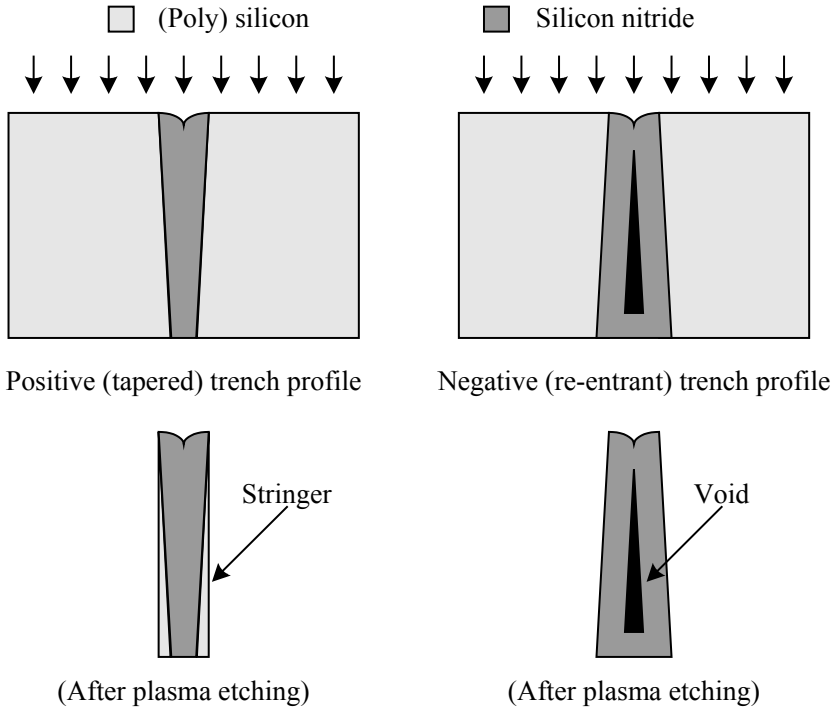

Figure 2.3: Electrical and mechanical properties of trench isolation depend on trench profile (a) Positive (tapered) profile, (b) Negative(re-entrant) profile.

Exposed trenches with a strong positive profile, refilled with a silicon nitride which has a high etch selectivity relative to (poly)silicon, serve unintentionally as an etching mask during the structural etch (*Step 5*) leaving (poly)silicon on the sidewalls of the refilled trench. The remaining (poly)silicon on the sidewalls, so called stringer, can cause an electrical short-circuiting and ultimately device failure. On the other hand, a strong negative profile allows complete removal of the (poly)silicon from the sidewalls but a complete refill is not achievable. The incomplete refill leaves a void or a keyhole, which causes a degradation of the mechanical strength of the refilled trench.

The thickness of the (poly)silicon device layer determines the maximum height of fabricated microstructures. However, the maximum achievable depth of isolating trenches limits the maximum height of microstructures with a proper vertical electrical insulation. Maximum trench depth is determined by trench width and maximum achievable aspect ratio of the etch process. Accordingly, a large

width allows fabrication of deep trenches. However, a small trench width is preferable in order to avoid an excessive deposition time during the refill step (*Step 3*). To completely refill a trench a layer with thickness of at least half of the trench width must be deposited. At the interconnection of two trenches a width is larger and the deposited layer must be even thicker. Not only the deposition time increase but the time to remove a layer from the top surface (*Step 4*) increases as well. Furthermore, a very thick deposited layer with a high intrinsic stress can make further processing difficult or even impossible. In practice, the maximum width of the isolation trenches should be limited to 5 μm [9].

Diverse materials or combination of materials can be used to refill the trenches. Basic requirements for the refill material are: (1) good electrical insulating properties, (2) highly conformal deposition and (3) compatibility with the rest of fabrication process. Silicon nitride solely or in combination with undoped polysilicon [2] is already successfully used as a refill material from which the later one is especially advantageous for wide trenches. A thin layer of silicon nitride is used to achieve electrical isolation and the polysilicon layer, with relatively low intrinsic stress and a high deposition rate, to completely refill the trenches. Other materials or combination of refill materials, which satisfy these three basic requirements, are possible as well.

2.3.3 Embedded interconnects

After trench refill (*Step 3*) and subsequent removal of the refill material from the top surface (*Step 4*) the wafer remains flat and smooth allowing further processing including a potential integration of electronic circuits. An additional planarization step, e.g. by Chemical Mechanical Polishing (CMP), may be necessary to insure VLSI compatibility of the wafer [2].

Interconnects made of polysilicon or aluminium [2-4] can be incorporated as part of the same electronic integration process or at the cost of two additional masks. The first mask to open, in a passivation layer, contact windows (vias) to the conductive (poly)silicon layer and the second one to pattern an interconnection layer, as schematically given in Fig. 2.4. In this situation, isolating trenches serve also as a mechanical support for the electrical interconnects.

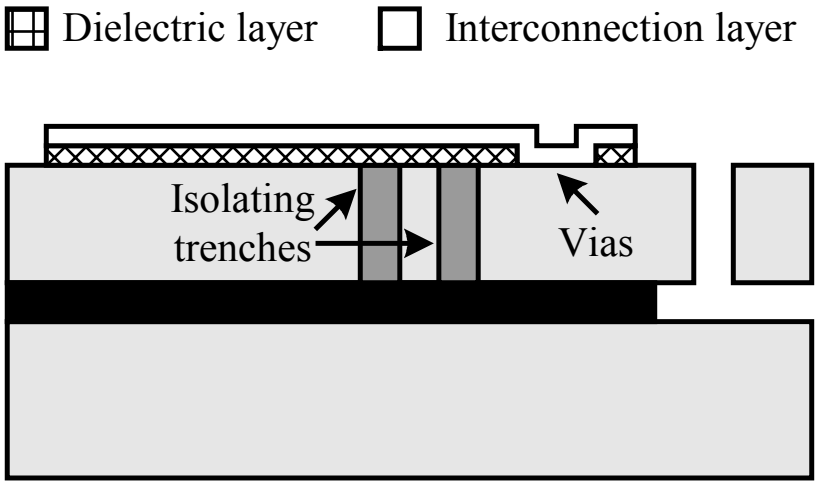

Figure 2.4: Cross section of a part with embedded interconnects.

The embedded interconnects provide an electrical connection between the distinct isolated regions, enable fully integration with on-chip electronics by connecting the integrated circuits to the structure region and allow multiple level electrical interconnects to be realized.

2.4 TECHNOLOGY FEATURES

2.4.1 Molded isolating structures

The basic trench isolation process, given in Fig. 2.1, employed to mechanically interconnect two distinct electrical regions can also be used to create other isolation structures without additional processing steps. (Poly)silicon molds refilled with silicon nitride, shown in Fig. 2.5 (left), are fully exposed to the etch plasma during the structural etching step (*Step 5*). The etch rate of silicon nitride is significantly lower than the etch rate of (poly)silicon resulting in a complete removal of (poly)silicon around the molded structures. After the release, freestanding isolating structures made of silicon nitride are realized.

The height of the freestanding isolating structure h_i depends on the thickness of the (poly)silicon device layer t_d and the selectivity of the (D)RIE process and is given by:

$$h_i = t_d(1 - \frac{v_i}{v_d}) \qquad (2.1)$$

where v_i and v_d are etching rates of the silicon nitride and the (poly)silicon, respectively.

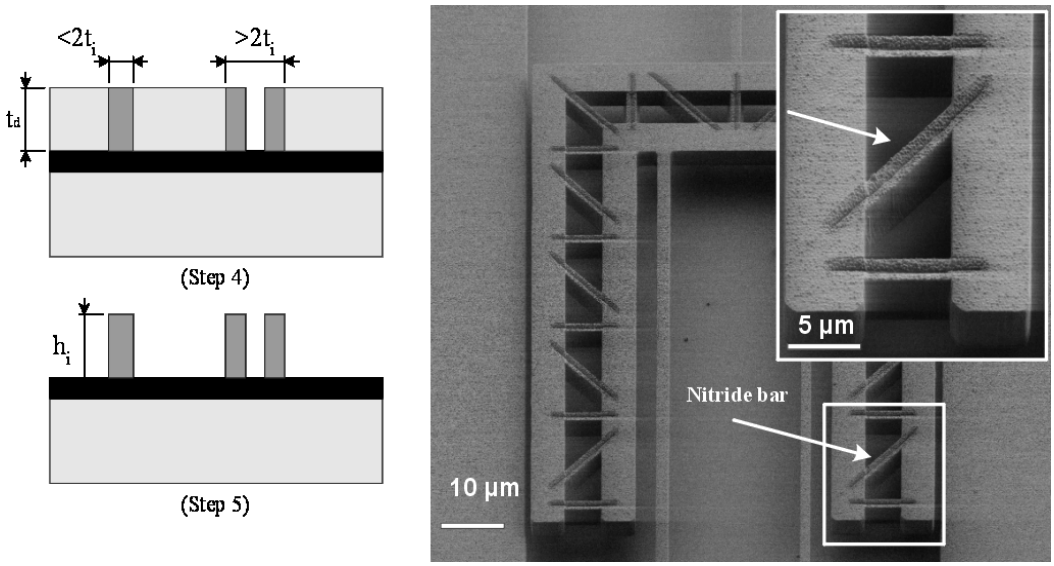

Figure 2.5: (left) Process outline for molded isolation structure, (right) SEM micrograph of silicon nitride bars embedded in doped polysilicon components forming a rigid truss.

The thickness of freestanding isolating structures depends on the width of trenches used for molding. A mold narrower then a double thickness of the deposited isolation layer (< $2t_i$) creates a structure with the thickness equal to the width of the mold. Otherwise the thickness of molded structures is equal to the thickness of the isolation layer t_i. Isolation structures can serve as flexible or rigid connections between movable or fixed conductive components. A manufactured framework, composed of silicon nitride bars embedded in doped polysilicon components forming a rigid truss, is shown in Fig. 2.5 (right).

The application of molded isolating structures is not limited to the mechanical connection of distinct conductive components. Different mechanical, electrical and thermal properties between silicon nitride and (poly)silicon can be exploited to generate new opportunities in MEMS design. In the subsequent section isolating structures are used to maintain a minimum distance between movable electrodes.

2.4.2 In-plane isolation: stoppers

In-plane movable components driven by electrostatic forces often require electrical insulation to prevent short circuiting caused by accidental or intentional physical contact. Silicon nitride sidewalls acting as insulating layers between movable components can be obtained by deposition of a thin silicon nitride layer prior to the release step (*Step 6*) and subsequent directional etching step. However, a silicon nitride layer covering a large electrode surface can give rise to charge accumulation leading to device malfunctioning or complete device failure. A considerable reduction of charge accumulation can be achieved by replacing continuous isolation layers by a set of properly spaced, small area isolating stoppers [10].

The molded isolating structures, presented in the previous section, can be effectively used for short-circuit protection. A schematic view of isolation structures employed as stoppers in a gap closing actuator with two movable electrodes is shown in Fig. 2.6 (left).

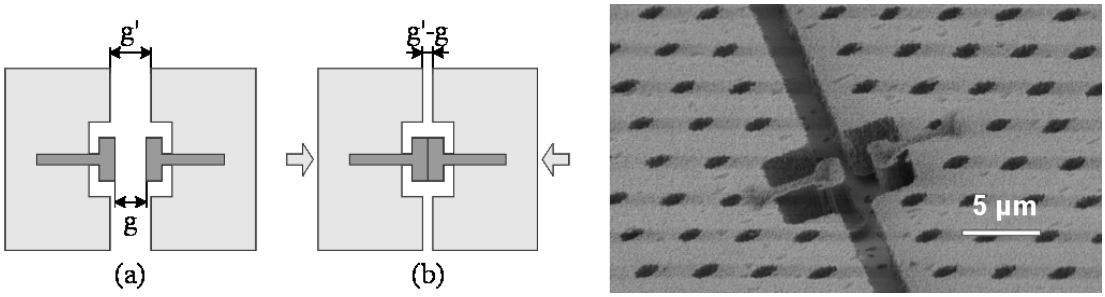

Figure 2.6: (left) A schematic view of isolating stoppers, (right) SEM micrograph of polysilicon electrodes with isolating stoppers made of silicon nitride. The isolating stoppers prevent the shortening between the movable electrodes regardless of the present mask misalignment (»1 µm).

The distance between the isolating stoppers *g*, defined in the first photolithography mask, is smaller then the separation between the movable electrodes *g*', defined in the second mask. Accordingly, contact only occurs between the isolating stoppers while the electrodes stay always at a distance equal or larger than *g*'-*g*. Proper designed isolating stoppers maintain the end distance between electrodes regardless of a possible mask misalignment. The minimum

controllable end-distance between the electrodes depends on the quality of the photolithography process, etching profile and the footing effect [11]. A SEM micrograph of two movable polysilicon electrodes with isolating stoppers is shown in Fig. 2.6 (right).

2.4.3 Out-of-plane isolation: bumps

By applying a short isotropic etch of the sacrificial silicon oxide prior to the deposition of the isolation layer (*Step 3*) small dents are created below the device layer. During successive conformal deposition of silicon nitride these dents are refilled producing isolating bumps, as shown in Fig. 2.7 (left).

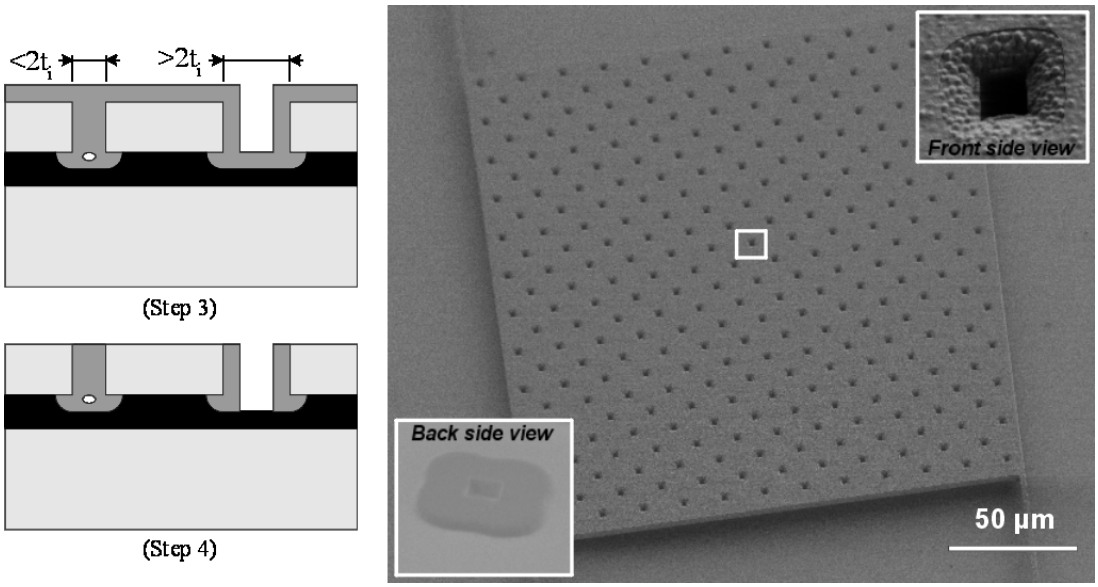

Figure 2.7: (left) Process outline for isolating bumps, (right) SEM micrograph of a released plate with hollow isolating bumps

By reduction of contact area these bumps can prevent stiction of components during release or during operation. Conducting parts exhibiting out-of-plane motion can benefit from the isolating bumps to prevent short-circuiting. The silicon nitride coating at the bottom of a hole larger then double the thickness of the deposited silicon nitride layer ($> 2t_i$) is removed during a maskless RIE step (*Step 4*) resulting in a hollow bump allowing sacrificial etching to take place through the bump, thus serving additionally as an etching hole. An SEM picture of a released plate with hollow bumps is shown in Fig. 2.7 (right). Hollow isolating

bumps are successfully employed for voltage-controlled clamps in electrostatic stepper micromotors (Chapter 8- Chapter 10).

2.5 APPLICATIONS

2.5.1 Force arrays

By connecting a large number of driving units in parallel and in series a large force and large displacement actuator, known as *Force Array Actuator* or *Distributed Electrostatic Micro Actuator* (*DEMA*), can be achieved [6-8]. Each driving unit consists of two wave-like [6] or parallel [7,8] electrodes, which can be elastically deformed by applying a voltage. The driving units can be operated simultaneously giving a smooth motion [6,7] or by a selective biasing of individual units resulting in a stepping motion [8]. Working principle of a force array actuator is illustrated in Fig. 2.8. on an actuator with a number of parallel electrodes connected in series.

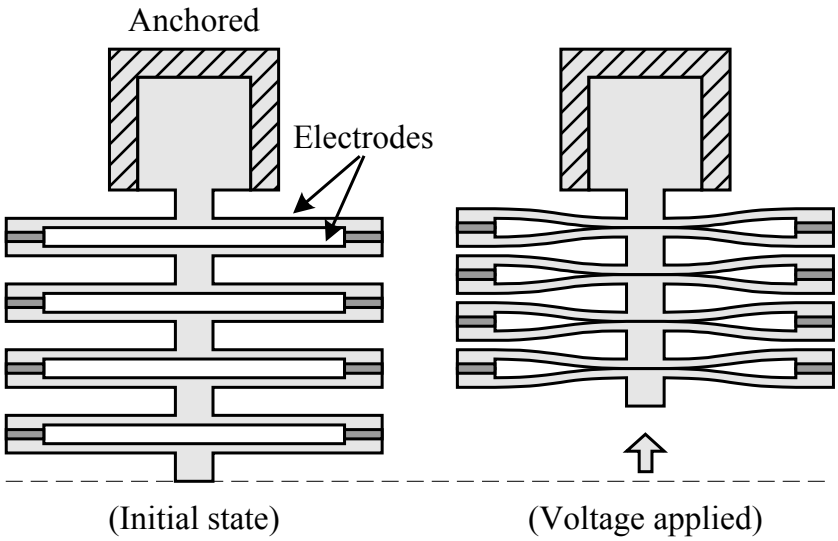

Figure 2.8: Working principle of a force array actuator.

A successful fabrication of this type of actuators demands electrical isolation between mechanically connected components. Several fabrication methods are already proposed: electroplating of copper in combination with photoresist [6], dual-mask processing of polyimide followed by directional evaporation of a bilayer [7] and a selective chemical vapor deposition of tungsten [8].

We have used the trench isolation technology to simplify fabrication of a force array actuator. A doped, 5 µm thick polysilicon layer on top of the sacrificial silicon oxide layer is used as the starting material. The fabricated array, shown in Fig. 2.9, consists of eight driving units serially connected. Each unit has two parallel electrodes 200 µm long, 2 µm thick and separated by a distance of 2 µm. The electrodes are joined together by isolating structures enabling selective biasing. Thin silicon nitride sidewalls are used to prevent short-circuiting between electrodes. The fabricated actuator was successfully operated and a maximal displacement of 4 µm was observed.

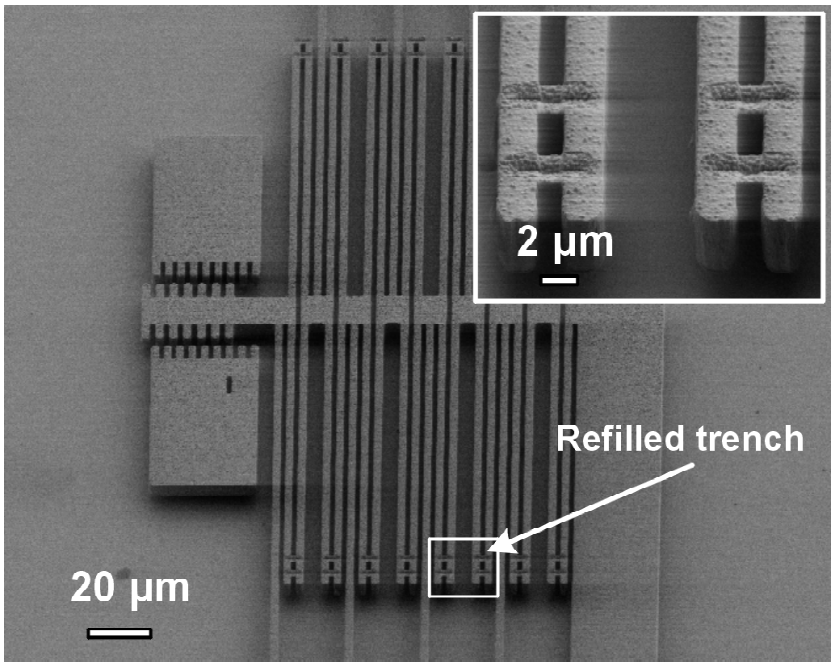

Figure 2.9: SEM micrograph of a force array actuator with eight driving units serially connected. Each unit consists of two parallel electrodes joined together by trench isolation.

The trench isolation technology yields several advantages compared to the originally proposed fabrication processes [6-8]. Besides simplicity of the fabrication process based on well-documented materials and processes, improvement on actuators performance is expected due to the attainable high-aspect ratios, outstanding mechanical properties of single crystal silicon and possibility of integration with electronics.

2.5.1 Contraction beams actuator

Micromotors based on the stepping motion can provide a large displacement by adding small steps in sequence. Stepper motors usually employ low displacement actuators to generate a single step. A novel electrostatic microactuator [12] for low displacement applications is fabricated using the trench isolation technology. This actuator, schematically given in Fig. 2.10, consists of parallel conducting beams which are perpendicular to the substrate and which are mechanically interconnected but electrically separated. On application of a voltage difference the beams deflect laterally inducing a powerful longitudinal contraction. Due to a built-in mechanical transformation [13] a large force and high-resolution displacement can be produced within a low actuator volume.

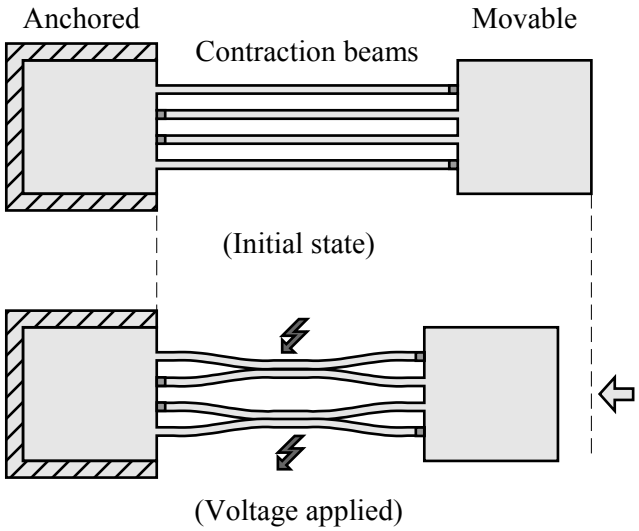

Figure 2.10: Working principle of a contraction beams actuator.

An electrostatic contraction beams actuator, fabricated using vertical trench isolation, is shown in Fig. 2.11. A doped, 5 µm thick polysilicon layer on top of the sacrificial silicon oxide layer is used as a device material. A thin layer of silicon nitride on the sidewalls is used to prevent short-circuiting between two parallel beams at pull-in. A large force (> 1 mN) with a controllable nanometer resolution step (< 15 nm) was measured for an actuator containing 16 parallel beams, 200 µm long, 2 µm thick with 2 µm distance between. The actuator fits in a volume of 200 x 62 x 5 µm and is operated by a voltage of 70 V.

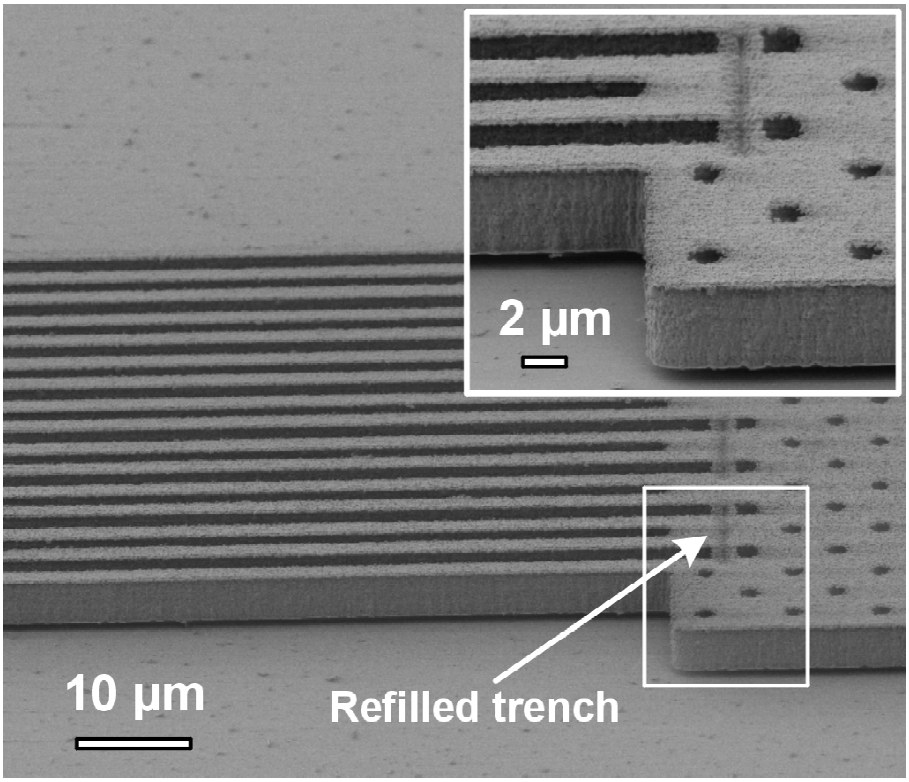

Figure 2.11: SEM micrograph of a contraction beam actuator. This electrostatic microactuator employs trench isolation technology for electrical insulation between neighbouring polysilicon beams

Another typical application for the new actuator includes the contraction/elongation body of a stepper motor as demonstrated in Chapter 10. Additionally, the actuator can be applied for vibration excitation or friction measurements [14].

2.6 CONCLUSIONS

New functions have been added to a trench isolation technology by rather small modifications and/or additions to the technology and by proper design while keeping the fabrication process rather simple. By employing trenches as mold, silicon nitride isolation structures are created. The isolation structures can be employed as flexible or rigid connections between movable or fixed conductive components or to prevent the short-circuiting between movable electrodes. Using isotropic etching in the sacrificial oxide layer isolation bumps are created. The isolation bumps can reduce stiction, prevent the short-circuiting due to a vertical

displacement and serve simultaneously as etch holes. The trench isolation technology complemented with the above-mentioned features is a powerful platform for MEMS fabrication. Besides possibilities for simplification of fabrication and improvement of performance of existing devices, the technology allows designers to create new types of MEMS. An electrostatic actuator consisting of a large number of parallel electrodes connected in parallel and in series are successfully fabricated and operated. The trench isolation technology presented here reduces the complexity of the originally proposed fabrication processes, allows improvement of the performance of this type of actuators by using high aspect ratio structures and/or by integration of electronics. Furthermore, a novel electrostatic microactuator has been fabricated using this technology. The novel actuator, which occupies small volume (200 μm x 62 μm x 5 μm), is able to produce a large force (> 1 mN) and a controllable nanometer resolution step. Typical applications for the new actuator can include the contraction/elongation body of a stepper motor, vibration excitation or friction measurements.

2.7 REFERENCES

1 Bustillo J M, Howe R T and Muller R S 1998 Surface micromachining for microelectromechanical systems *Proceedings of the IEEE* **86**(8) 1552-1574

2 Brosnihan T J 1998 An SOI based, fully integrated fabrication process for high-aspect-ratio microelectromechanical systems *PhD Thesis* Department Of Mechanical Engineering, University of California, USA.

3 Brosnihan T J, Bustillo J M, Pisano A P and Howe R T 1997 Embedded interconnect and electrical isolation for high-aspect-ratio, SOI inertial instruments *Int. Conf. on Solid State Sensors and Actuators* (TRANSDUCERS 97) (Chicago, USA) 637-640

4 Lemkin M A, Juneau T N, Clark W A, Roessig T A and Brosnihan T J 19xx A low-noise digital accelerometer using integrated SOI-MEMS technology *Int. Conf. on Solid State Sensors and Actuators* (TRANSDUCERS 99) (Sendai, Japan) 1294-1297

5 Schenk H, Dürr P, Kunze D, Lakner H and Kück H 2001 A resonantly excited 2D-micro-scanning-mirror with large deflection *Sensors Actuators* A **89** 104-111

6 Minami K, Kawamura S and Esashi M 1993 Fabrication of Distributed Electrostatic Micro Actuator (DEMA) *J. Microelectromech. Syst*. **2**(3) 121-127

7 Jacobson J D, Goodwin-Johansson S H, Bobbio S M, Bartlett C A and Yadon L N 1995 Integrated force arrays: Theory and modeling of static operation *J. Microelectromech. Syst*. **4**(3) 139-150

8 Chen L Y, Santos E J P and MacDonald N C 1993 Serial-parallel isolated capacitive microactuators *Int. Conf. on Solid State Sensors and Actuators* (TRANSDUCERS 93) (Yokohama, Japan) 84-87

9 de Boer M J, Tjerkstra R W, Berenschot J W, Jansen H V, Burger G J, Gardeniers J G E, Elwenspoek M and van den Berg A 2000 Micromachining of buried micro channels in silicon *J. Microelectromech. Syst*. **9**(1) 94-103

10 Wibbeler J, Pfeifer G and Hietschold M 1998 Parasitic charging of dielectric surfaces in capacitive microelectromechanical systems (MEMS) *Sensors Actuators* A **71** 74-80

11 Arnold J C and Sawin H H 1991 Charging of pattern features during plasma etching *J. Appl. Phys.* **70**(10) 5314-5317

12 Sarajlic E, Berenschot E, Krijnen G and Elwenspoek M 2003 Low volume, large force (>1mN) and nanometer resolution, electrostatic microactuator for low displacement applications *Nanotechnology Conference and Trade Show* (NANOTECH 2003) (San Francisco, USA) **1** 637-640

13 Tas N, Wissink J, Sander L, Lammerink T and Elwenspoek M 1998 Modeling, design and testing of the electrostatic shuffle motor *Sensors Actuators* A **70** 171-178

14 de Boer M P, Redmond J M and Michalske T A 1998 A hinged-pad test structure for sliding friction measurement in micromachining *SPIE conf. Materials and Device Characterization in Micromachining* (Santa Clara, USA) vol **3512** (SPIE) 241-250

Chapter 3

Advanced plasma release and vertical trench isolation

Abstract

A bulk micromachining technology, which combines advanced plasma processing to etch, passivate and release micromechanical structures in a single plasma system and vertical trench isolation to obtain electrical insulation between released microstructures, is presented in this chapter. The technology, suitable for full integration with on-chip electronics, allows MEMS fabrication in a standard silicon wafer. High aspect ratio monocrystalline silicon MEMS with integrated vertical trench isolation on fixed and even on movable parts can be realized. The presented bulk micromachining technology is an attractive platform for both fabrication and rapid prototyping of MEMS. This is due to a short processing time, a large freedom of design, a high process flexibility and a low-cost of the starting standard silicon substrate relative to SOI substrates. Several example microstructures demonstrating the capabilities of this technology have been successfully fabricated.

3.1 INTRODUCTION

Many classes of MEMS devices, both sensors and actuators, take advantage of well-established electrical and superior mechanical properties of single-crystal silicon [1] in combination with a relatively large device height to improve device performance. A widespread method for the fabrication of high-aspect-ratio, monocrystalline silicon MEMS is the use of SOI wafers.

An SOI compatible trench isolation technology, introduced in Chapter 2, gives opportunities to further improve performance of MEMS. This technology employs trenches refilled with a dielectric material to obtain electrical isolation between mechanically connected components. Distinct electrical domains can be defined on fixed and even on movable parts allowing large freedom of design. Besides possibilities for simplification of the fabrication and improvement of the performance of existing devices, the SOI-based trench isolation technology allows design of entirely new MEMS.

Main drawbacks of the SOI-based trench isolation technology for fabrication of high-aspect-ratio, monocrystalline silicon MEMS are associated with the use of SOI wafers: a relatively high cost of the wafer, fixed thickness of the device layer, a limited thickness of the buried oxide layer, the notching effect [2] and a sacrificial oxide layer etch required to release structures.

Several methods of bulk micromachining [3-7] based on standard silicon wafers are proposed as an alternative to the standard SOI technology. All these methods employ Deep Reactive Ion Etching (DRIE) to pattern, a passivation layer to protect and plasma isotropic etching to release structures in the bulk material. Different techniques are used to electrically isolate the released structures from the bulk material: by metallization [3,4], by creating silicon islands surrounded by electrically insulating silicon oxide [5], by use of aluminium interconnects to fasten released components [6] or by employment of suspended thermal silicon oxide isolation segments [7]. In addition to an electrical isolation from the bulk material, the isolation technology employing the suspended thermal oxide segments [7] can provide an electrical isolation between mechanically connected structures, exploiting all benefits of the SOI compatible trench isolation

technology and avoiding at the same time the drawbacks associated with the use of SOI wafers.

This chapter introduces a bulk micromachining technology for fabrication of high-aspect-ratio single-crystal silicon MEMS in standard silicon wafers by combining suspended trench isolation with an advanced plasma processing technique, the Black Silicon Method (BSM) multi-step one-run process [8]. A significant advantage of this process is that etching, passivation and release of MEMS take place in a single plasma system during a single etch run. A fast processing and a relative low-cost of the substrate accompanied with large freedom of design and high process flexibility makes this technology an attractive platform for fabrication and rapid prototyping of MEMS.

3.2 TECHNOLOGY

Main fabrication steps of the proposed technology are shown in Fig. 3.1.

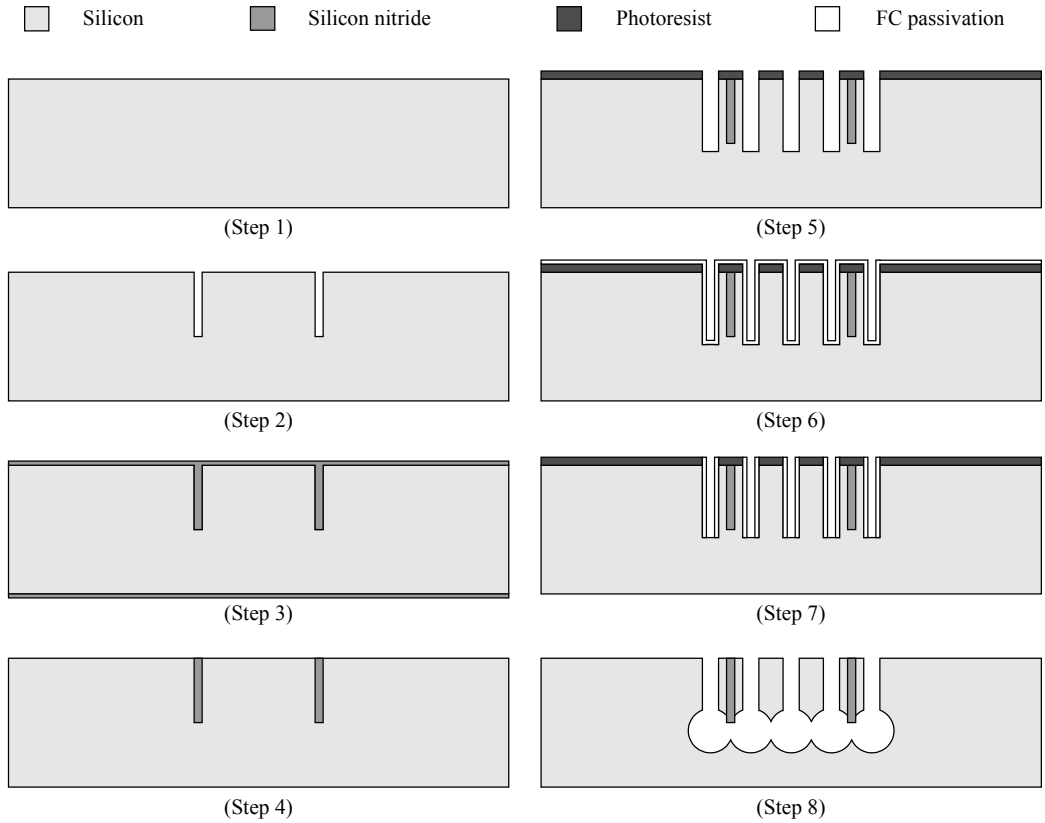

Figure 3.1: A bulk micromachining process for MEMS fabrication in standard silicon wafer by combining trench isolation and advanced plasma release.

The starting material for the two-mask fabrication process is a standard silicon wafer with an arbitrarily crystallographic orientation (*Step 1*). To assure electrical conductivity of the substrate a highly conductive wafer can be selected or an impurity doping can be performed.

In the selected wafer, trenches are etched using deep silicon etching (*Step 2*). A perfect vertical or slightly negative trench profile is required in order to insure reliable electrical isolation (see Section 2.3.2). The maximum trench depth is determined by the width of trenches and the maximum achievable aspect ratio of the etching process. A small width of trenches is preferred to reduce both the deposition and the removal time of the isolation layer in the subsequent fabrication steps.

On the patterned surface, an LPCVD low-stress silicon nitride is deposited to completely refill the trenches (*Step 3*). Silicon nitride is employed for its good electrical insulating properties and highly conformal step coverage. Other dielectric or poor conducting materials, e.g. thermal silicon oxide [6], can be used as well.

The deposited isolation layer is removed from the top and the bottom of the wafer using a blanket etch (*Step 4*), leaving the silicon nitride only in the refilled trenches. The surface of the wafer remains flat and smooth after the blanket etch allowing further processing including a potential integration of electronic circuits. Optionally, polysilicon or aluminium interconnects, discussed in Section 2.3.3, can be incorporated as part of the same electronic integration process or at the cost of two additional masks (not shown in Fig. 3.1).

After removal of the isolation layer, micromechanical structures are created in the bulk material by employing an advanced plasma processing technique, the so-called Black Silicon Method (BSM) multi-step one-run process [8]. This technique has the ability to etch, passivate and release structures in a single plasma run. The advantages of the BSM method, compared to the more traditional methods [3,4,7] that employ a silicon oxide layer to protect the structures during the isotropic release, include simplified and fast fabrication, low temperature processing and an easily removable low-stress fluorocarbon (FC) passivation layer.

The BSM starts with the directional transfer of the photoresist pattern in the bulk silicon using DRIE (*Step 5*). Subsequently, a thin FC passivation layer is

uniformly deposited (*Step 6*) to protect the structures during the following isotropic release step. The passivation layer from planar surfaces is removed using directional plasma etching (*Step 7*). In the last release step a selective isotropic plasma etch of silicon is performed in order to undercut the structures (*Step 8*). The photoresist mask and the passivation layer can be removed in an oxygen plasma followed by a thermal ashing.

Released micromechanical structures with integrated trench isolation, fabricated by the presented technology, are shown in Fig. 3.2.

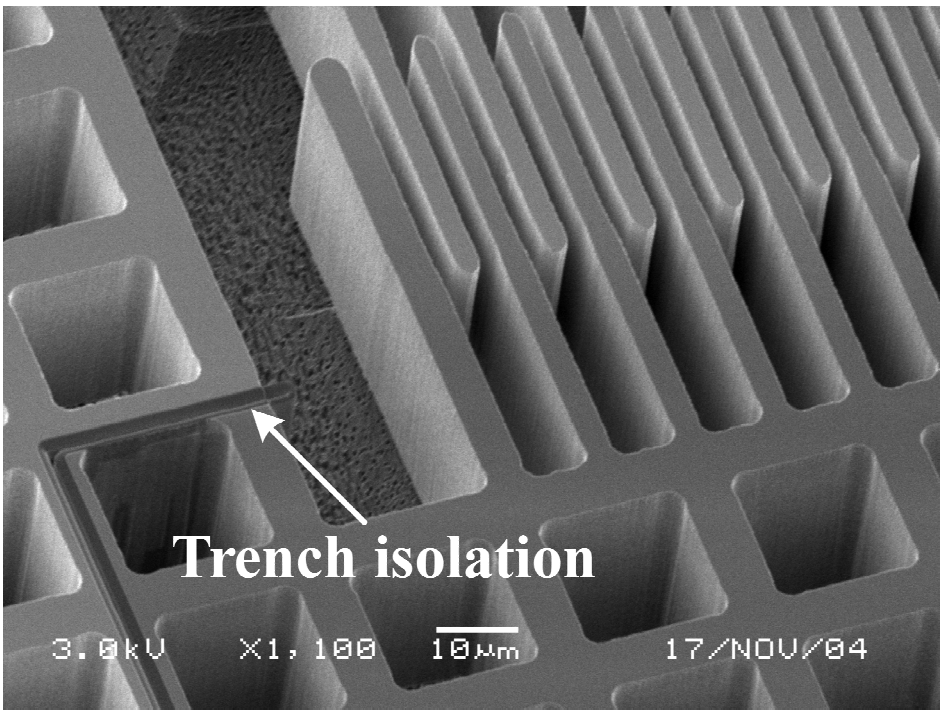

Figure 3.2: SEM micrographs of released microstructures with properly integrated trench isolation.

The suspended silicon nitride trenches assure mechanical integrity and electrical insulation between the released, high-aspect-ratio, monocrystalline microstructures. A visible contrast difference between electrically insulated parts arises from the charging during SEM session. The contrast difference provides evidence for good electrical insulation.

3.3 DESIGN AND PROCESSING ISSUES

Several design and process parameters, shown in Fig. 3.3, must be chosen and controlled in order to successfully fabricate released microstructures with a reliable electrical insulation.

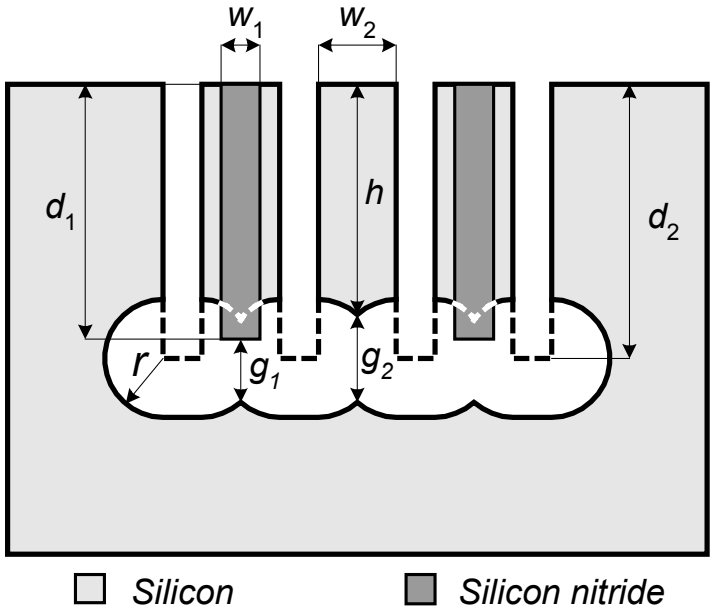

Figure 3.3: A schematic view of a released insulated structure with important design and process parameters.

A careful mask design and an accurate process control are necessary to assure successful release and uniform height of MEMS components. A small structure width w_2 is favourable in order to decrease the etch time and to reduce the loss of the structure height during the plasma release step. A grid or a honeycomb design can be used for large area structures.

The structure height h is a process parameter and hence can be easily varied. The final structure height is determined by the structural etch depth d_2 reduced by the isotropic etch distance r. The etch distance must be larger than the half structure width (r>0.5w_2) in order to completely release the structure.

A uniform mask design with small variations in the trench width (or opening) suppresses the Aspect Ratio Dependent Etching (ARDE) effect, also called RIE lag. Due to the ARDE effect smaller trenches (openings) are etched (*Step 5*)

slower than wider trenches (openings), as schematically shown in Fig. 3.4 (left). Differences in the trench depth induce variations in the final structure height after the isotropic release (*Step 8*). Furthermore, the different etch depths can cause variation and increase in the release time.

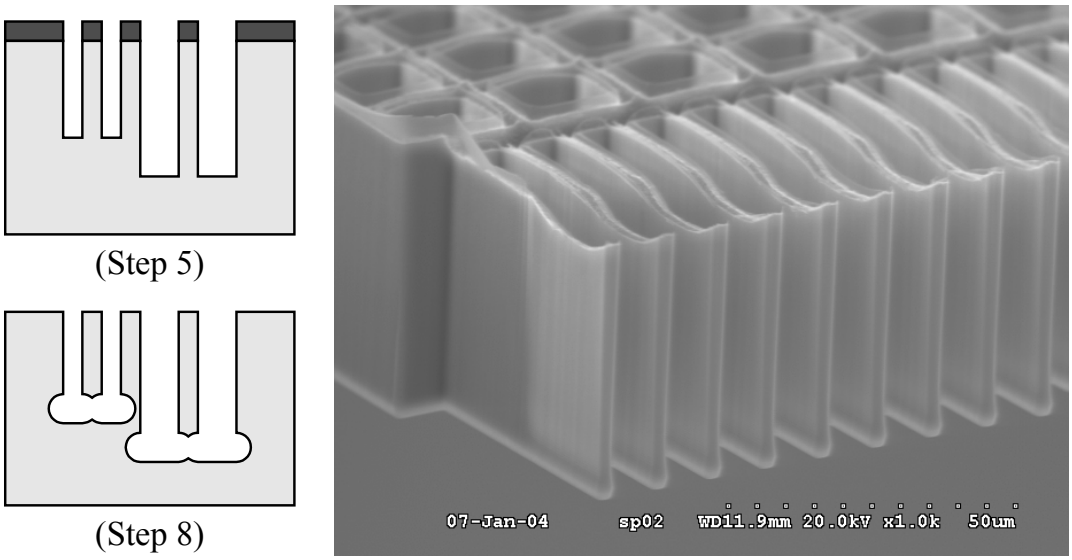

Figure 3.4: Influence of ARDE effect on etch uniformity, release time and final structure height (left). The backside of a released comb drive with non-uniform height caused by the ARDE effect (right).

Comb drive fingers with non-uniform height, caused by the ARDE effect, are shown in Fig. 3.4 (right). The height variation is the most pronounced on the finger part, which belongs to the overlapping area between fingers on stationary and movable combs.

The height variations caused by the ARDE effect can be further amplified by the non-uniform etch rate of silicon (lower etch rate in smaller trenches) during the isotropic release step. A special etching method for eliminating the ARDE effect [9] can be employed in addition to a restrictive mask design to achieve uniform structure height. An extra directional etch [6] employed prior to the isotropic release (*Step 8*) increases the gap g_2 between the micromechanical structures and the substrate, reduces the release time and also suppresses variation in the release time induced by the ARDE effect.

In the proposed fabrication process refilled trenches are employed. A large mechanical strength and a high electrical resistance between components connected by a refilled trench assure for both mechanical integrity and electrical isolation. An isolation trench can be placed within the structure ($w_2>w_1$) and protected by the photoresist during the structural etching step (*Step 5*) or can be fully exposed to the etch plasma. The etch rate of silicon nitride is significantly lower than the etch rate of silicon resulting in a complete removal of silicon around the refilled trench and formation of freestanding isolating structures made of silicon nitride after the release (see Section 2.4.1).

To achieve a reliable electrical isolation, the structural depth d_2, the isolation trench depth d_1 and the isotropic etch distance r must be selected in accordance to each other. Assuming that the release process is completely isotropic, the etch distance r has to be larger then half the width of the structure ($r>0.5w_2$) to completely undercut it. However, when the structural etch is deeper then the isolation trench ($d_2>d_1$) a minimum etch distance r, required for a reliable electrical isolation, is equal to:

$$r = \sqrt{(d_2 - d_1)^2 + \left(\frac{w_2}{2}\right)^2} \qquad (3.1)$$

Accordingly, a released structure does not always implicate a good electrical isolation and vice versa a good electrical isolation is not a warrant for a movable structure. Three different situations that can arise depending on selected design and fabrication parameters are illustrated in Fig. 3.5.

A relative deep isolation trench and a relative short release step, illustrated in Fig. 3.5(a), leave the molded dielectric parts embedded in the bulk material resulting in a good electrical isolation and a very stiff suspension, only desirable in some applications. Obviously, in this case an electrical isolation on movable parts is not possible. In order to achieve this well-timed etching and release processes, shown in Fig 3.5(b), are necessary. A relative deep structural etch and an insufficient long release step may leave a silicon bridge at the bottom of the refilled trench resulting in unintentionally short-circuited movable structures as shown in Fig 3.5(c).

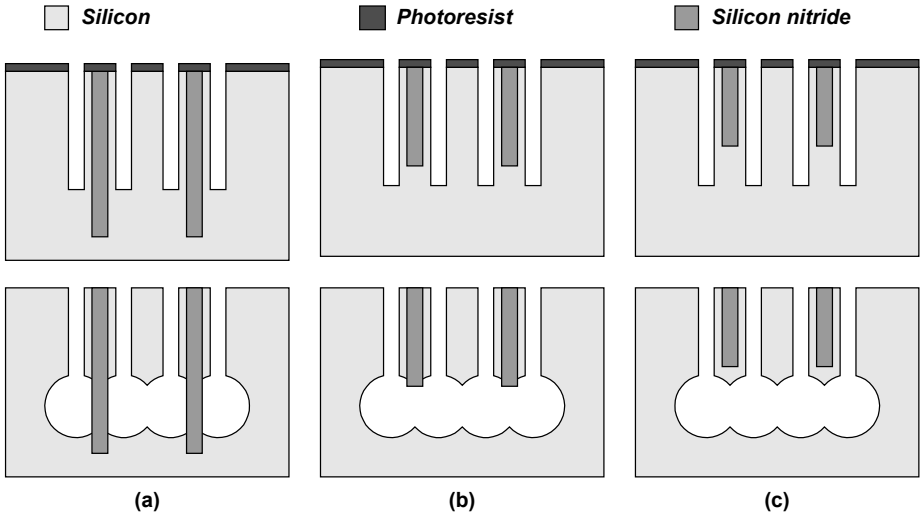

Figure 3.5: Reliable electrical isolation requires a careful selection of design and process parameters: (a) high stiffness support, (b) movable structure with integrated isolation and (c) short-circuited structure.

The backside of a micromechanical structure with integrated trench isolation, fabricated in a well-timed etch and release process, is given in Fig. 3.6. A protruding isolating trench, which is an essential condition for a reliable electrical insulation, is clearly visible.

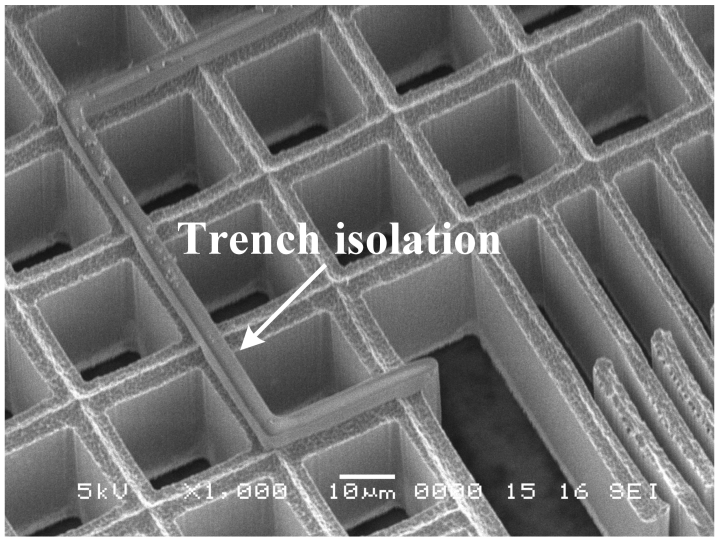

Figure 3.6:A SEM micrograph of the backside of released microstructures with properly integrated trench isolation.

Vertical trench isolation requires only a small wafer area and can be configured in many different ways depending on application. Three typical configurations are depicted in Fig. 3.7.

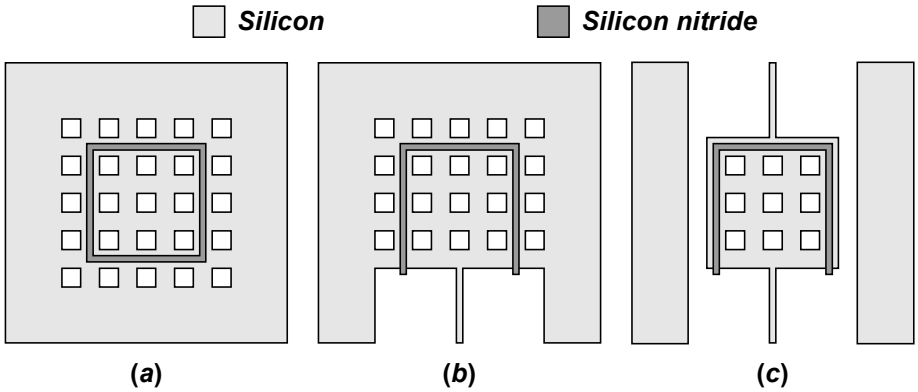

Figure 3.7: Trench isolation assures both electrical isolation and mechanical integrity. Different trench arrangement results in: (a) an isolated material island, (b) an anchor and (c) a movable part with integrated isolation.

A suspended material island, schematically given in Fig 3.7(a), is entirely surrounded by the refilled trench, thereby completely electrically isolated from the surrounding. An anchor configuration, shown in Fig 3.7(b), is only partially embedded into the bulk material by the refilled trench. A free side of the anchor can be used to connect some functional part. The anchor configuration can also serve as an electrical pad to connect the MEMS devices to a standard probe station enabling the device testing on wafer level. Suspended trench isolation allows creation of distinct electrical domains even on a movable part, as shown in Fig 3.7(c).

3.4 FABRICATION AND APPLICATIONS

Diverse example microstructures e.g. comb drive microactuators and XY-scanners, are successfully fabricated using the proposed technology.

3.4.1 Fabrication process

The fabrication process is started on a highly conductive (100) silicon wafer. Isolating trenches with slightly negative profile, 2 μm wide and 30 μm deep, are etched by cryogenic DRIE using SF_6/O_2 based plasma chemistry [10]. The etched

trenches are completely refilled with a 1.2 µm thick LPCVD low-stress silicon nitride. The deposited silicon nitride layer from the top of the wafer is removed by a standard RIE using CHF_3 plasma.
After lithography of the device layout with standard Olin 917 photoresist, the BSM release process is employed to fabricate released microstructures in a single plasma system. The BSM process is performed in a state of the art etching machine type AMS 100SE of the company ADIXEN [11]. Several test runs have been carried out in order to optimise the release process. A test microstructure, manufactured with the optimised BSM release process, is shown in Fig. 3.8.

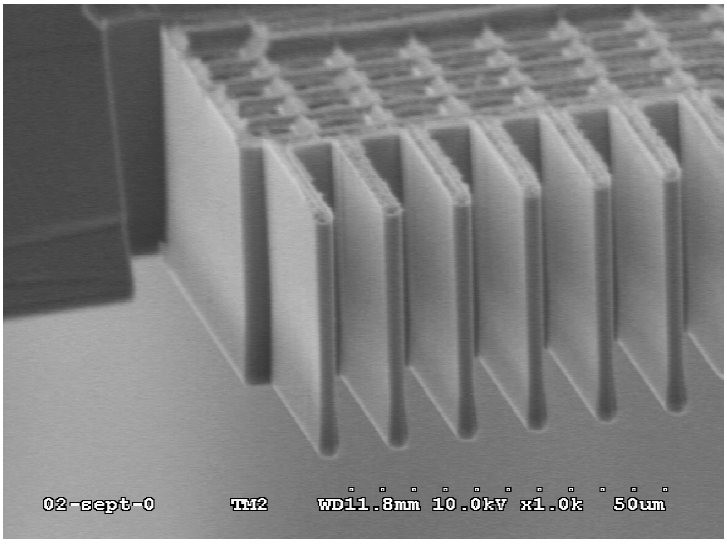

Figure 3.8: SEM micrograph of the back side of a 45 µm high test microstructure fabricated using BSM release process

In the first BSM step all trenches with different exposed areas are uniformly etched at the same depth as the isolation trenches (~30 µm) with the so-called Bosch process. The ARDE-effect [9] is suppressed by employing a gas mixture with a relative high C_4F_8 flow. In this way, an extra fluorocarbon is deposited in larger trenches reducing its silicon etch rate compared to smaller trenches and creating thereby a more uniform etch rate for the trenches with different exposed areas. During the second step the FC coating is uniformly deposited on the walls of the etched structures using pure C_4F_8 plasma. The FC-layer acts as a protection layer during the isotropic release step. Before the release can take place the FC

coating on the bottom of the trenches is removed by directional SF_6 plasma using a relative high ion energy. A selective isotropic SF_6 etch of silicon is performed with a pure chemical SF_6 plasma with a low ion energy. The parameter settings for the optimised release process are summarized in Table 3.1.

Table 3.1: Optimised process parameters for BSM release process on AMS 100SE etching machine.

Process step (Figure 3.1)	Description	Gasses (SF_6/C_4F_8)	Source Power (Watt)	Pressure (Pa)
Step 5	DRIE of Silicon	400/400	1500	4
Step 6	FC Coating	0/300	1800	10
Step 7	Bottom removal	300/0	1800	10
Step 8	Isotropic etch	300/0	1800	10

The etch, passivation and release process is completed in the same plasma chamber within 11 minutes. The final height of the released structures was 28 μm. A gap between the freestanding structure and the bulk of the substrate was 7 μm.

3.4.2 Comb drive actuator

A comb drive [12] is an electrostatic microactuator, which consists of one movable and one stationary interdigitated comb-like structure. Applying a voltage difference between the combs results in an electrostatic force, which displaces the movable comb.

An electrostatic comb drive actuator fabricated in a standard silicon wafer using the proposed technology is shown in Fig. 3.9. Contact pads and stationary combs are fixed to the bulk material by the refilled silicon nitride trenches enabling application of a potential difference between comb fingers on the stators and comb fingers on the movable shuttle. The comb fingers were 50 μm long and 3 μm wide. The gap spacing between the fingers and the initial finger overlap were 3 μm and 25 μm, respectively. The movable shuttle is suspended by folded flexures (347 μm long and 2 μm wide) to the bulk material, which was electrically grounded. Electrical contact with the stationary combs is achieved through contact pads. A standard probe station could be used owing to the high stiffness and large mechanical strength of the suspended contact pads.

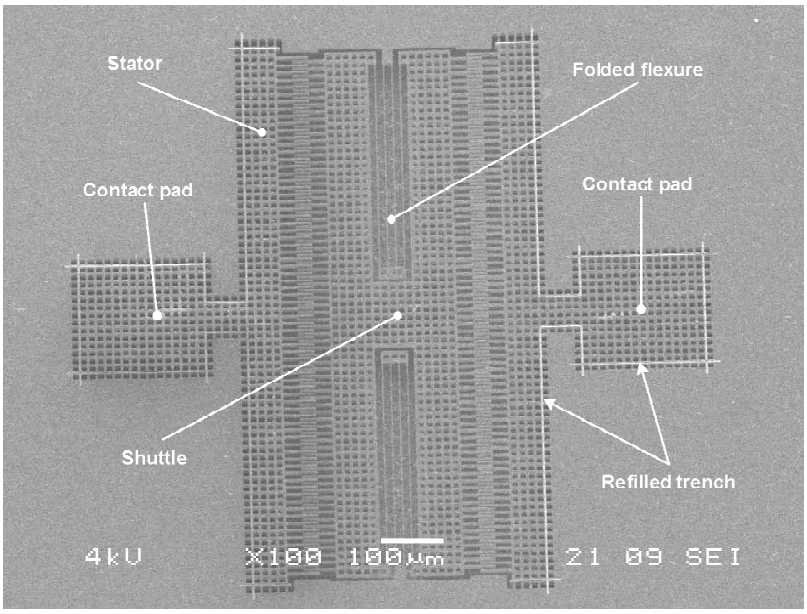

Figure 3.9: SEM micrograph of an electrostatic comb-drive microactuator. The driving voltage is applied on the suspended contact pads using a standard probe station.

The comb-drive actuator was successfully operated. The maximum displacement of ± 9 µm was limited by design.

3.4.3 XY-Scanner

In order to demonstrate electrical isolation on movable parts an XY-scanner, driven by comb drive actuators, is designed and fabricated.

An overview of the realized XY-scanner is shown in Fig. 3.10. The XY-scanner consists of a 1430 µm x 1012 µm large movable shuttle. The shuttle is suspended by four, 336 µm long and 4 µm wide, folded flexures to the stationary part. A pair of electrostatic comb drive actuators are employed to move the shuttle bidirectionally along one axis (pull-pull). A small (996 µm x 206 µm) central stage is suspended to the large movable shuttle by two folded flexures and driven by another pair of comb drives in the direction perpendicular to the movement of the shuttle. This serial stacked assembly assures independent motion of the central stage in two axial directions.

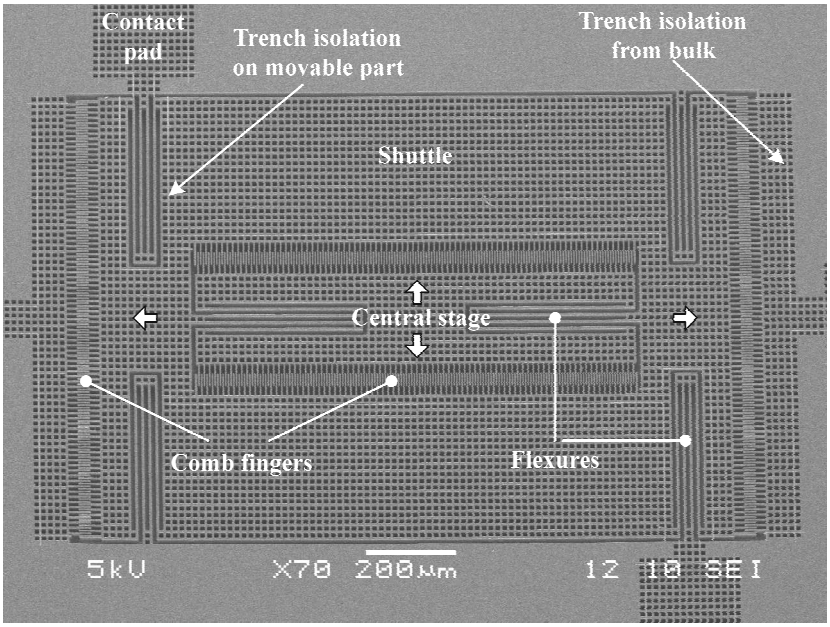

Figure 3.10: SEM micrograph of an XY-scanner.

Trench isolation is employed to achieve electrical insulation from the bulk material and to create distinct electrical domains on the movable parts (Fig. 3.11).

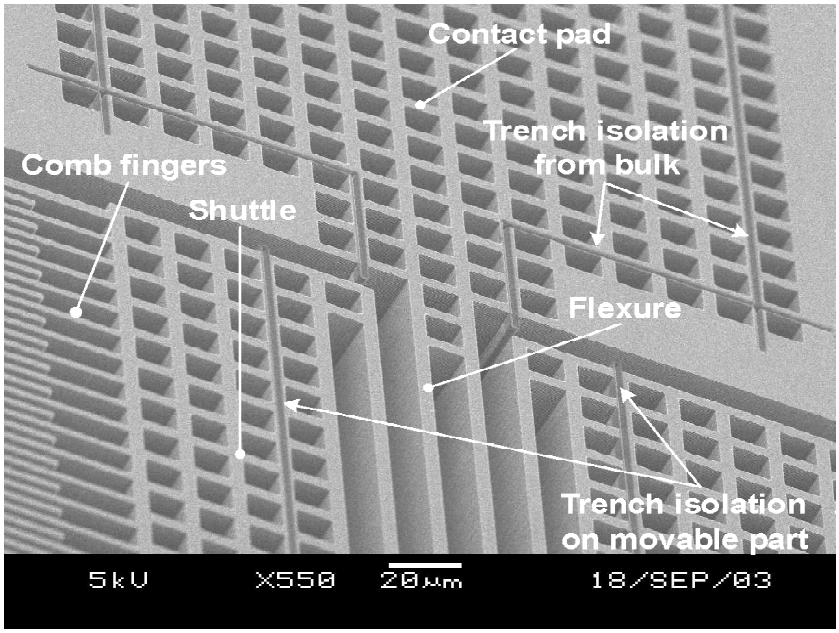

Figure 3.11: SEM micrograph of a portion of an XY-scanner. Trench isolation was employed to insulate structure from the bulk and to define various electrical domains on a movable shuttle.

The trench isolation on the movable shuttle allows independent excitation of the central stage. The XY-scanner was successfully driven independently in both axial directions. The maximum achieved displacement of ± 9 μm for both directions was limited by design.

3.5 CONCLUSIONS

A bulk micromachining technology is presented. A two-mask process allows for fabrication of single-crystal, high-aspect-ratio microstructures in a standard silicon wafer. Distinct electrical domains can be defined on movable parts in addition to electrical insulation from the bulk of the wafer. The electrical isolation achieved using trenches refilled with dielectric material requires low wafer area and can be employed in various ways depending on the application. The sophisticated electrical isolation accompanied with a relative low-cost of the starting material, a relative fast and reliable dry release and a large design freedom makes the technology an attractive platform for MEMS fabrication and rapid prototyping. An electrostatic comb-drive actuator and an electrostatic XY-scanner have been successfully fabricated using this technology.

3.6 REFERENCES

1 Petersen K E 1982 Silicon as a mechanical material *Proceedings of the IEEE* **70**(5) 420-457

2 Arnold J C and Sawin H H 1991 Charging of pattern features during plasma etching *J. Appl. Phys.* **70**(10) 5314-5317

3 Lisa Z Z and MacDonald N C 1992 A RIE process for submicron silicon electromechanical structures *J. Micromech. Microeng*. **2** 31-38

4 MacDonald N C 1996 SCREAM MicroElectroMechanical Systems *Microelect. Eng.* **32** 49-73

5 Sridhar U, Lau C H, Miao Y B, Tan K S, Foo P D and Liu L J 1999 Single crystal silicon microstructures using trench isolation *Int. Conf. on Solid State Sensors and Actuators* (TRANSDUCERS 99) (Sendai, Japan) 258-261

6 Bertz A, Küchler M, Knöfler R and Gessner T 2002 A novel high aspect ratio technology for MEMS fabrication using standard silicon wafers *Sensors Actuators* A **97-98** 691-701

7 Webb R Y, Adams S G and MacDonald N C 1998 Suspended thermal oxide trench isolation for SCS MEMS *SPIE Conf. Microrobotics and Micromanipulation* (Boston, USA) vol **3519** (SPIE) 196-199

8 de Boer M J, Jansen H and Elwenspoek M 1995 A study of the fabricating of movable structures for MEMS *Int. Conf. on Solid State Sensors and Actuators* (TRANSDUCERS 95) (Stockholm, Sweden) 565-568

9 Dijkstra P, Puech M, Launay N, Arnal N, Rolland L and Gruffat J M 2003 New development in silicon and oxide ICP etching for MEMS *14th Micromechanics Europe Workshop* (MME03) (Delft, The Netherlands) 107-110

10 de Boer M J, Gardeniers G E, Jansen H V, Smulders E, Gilde M, Roelofs G, Sasserath J N and Elwenspoek M 2002 Guidelines for etching silicon MEMS structures using fluorine high-density plasmas at cryogenic temperatures *J. Microelectromech. Syst.* **11** 385-401

11 Adixen Micro Machining Systems (www.adixen.com), Alcatel Vacuum Technology, Annecy Cedex, France

12 Tang W C, Lim M G and Howe R T 1989 Laterally driven polysilicon resonant microstructures *IEEE Micro Electro Mechanical Systems Workshop* (Salt Lake City, USA) 53-59

Chapter 4

Vertical trench isolation and backside release

Abstract

In this chapter, we introduce a bulk micromachining technology, based on standard single crystal silicon wafer, which combines a backside etching with vertical trench isolation. The backside etching permits a dry release of high-aspect-ratio microstructures with a large non-perforated area and a uniform height. The vertical trench isolation assures an electrical insulation of microstructures from the bulk material and also between distinct movable microstructures mechanically linked with a flexible or rigid connection. Electrostatic XY-scanners driven by comb drive actuators with a large non-perforated central shuttle and a contraction beams actuator with a relative large height of beams are successfully fabricated using this technology.

4.1 INTRODUCTION

The bulk micromachining technology, presented in the previous chapter, allows fabrication of MEMS in a standard silicon wafer. High-aspect-ratio monocrystalline MEMS with embedded electrical insulation on fixed and movable parts can be fabricated and integrated with on-chip electronics. The technology employs advanced plasma processing to etch, passivate and release micromechanical structures in a single plasma system, and vertical trench isolation to obtain electrical insulation between released microstructures. The technology is an attractive platform for fabrication and rapid prototyping of MEMS due to the relatively low cost of the starting substrate, sophisticated electrical insulation, CMOS compatibility, low temperature processing, dry release, high process flexibility and short processing time.

Despite of many advantages of the aforementioned technology, there are also some drawbacks, which are directly associated with the use of the isotropic plasma etch to release the microstructure. Careful mask design with small variations in pattern size and special etching methods that suppress the Aspect Ratio Dependent Etching (ARDE) effect are necessary to assure successful release and uniform height of microstructures (see Section 3.3). In addition, the dimensions of the microstructures, which can be laterally undercut by the plasma release, are limited. A mesh-like design is required to release large area microstructures, which makes the technology less suitable for applications that require micromechanical structures with a large non-perforated area e.g. in data storage to maximize the effective recording area or in optical systems [1,2].

To overcome these drawbacks without loosing all the advantages, we proposed a fabrication method, in which a backside etch releases microstructures with integrated trench isolation. A similar approach [3], developed independently from our work, was already successful in fabrication of a single-chip integrated gyroscope.

The following sections explore the use of vertical trench isolation in combination with backside release for MEMS fabrication, focusing on the manufacturing of electrostatic microactuators. The fabrication process is outlined and some critical fabrication steps related to the backside release are discussed in

more detail. Different types of electrostatic actuators that were successfully fabricated and operated are described, demonstrating the large flexibility of this fabrication method.

4.2 BACKSIDE RELEASE

Basic fabrication steps of the bulk micromachining technology based on vertical trench isolation and a backside release are illustrated in Fig. 4.1.

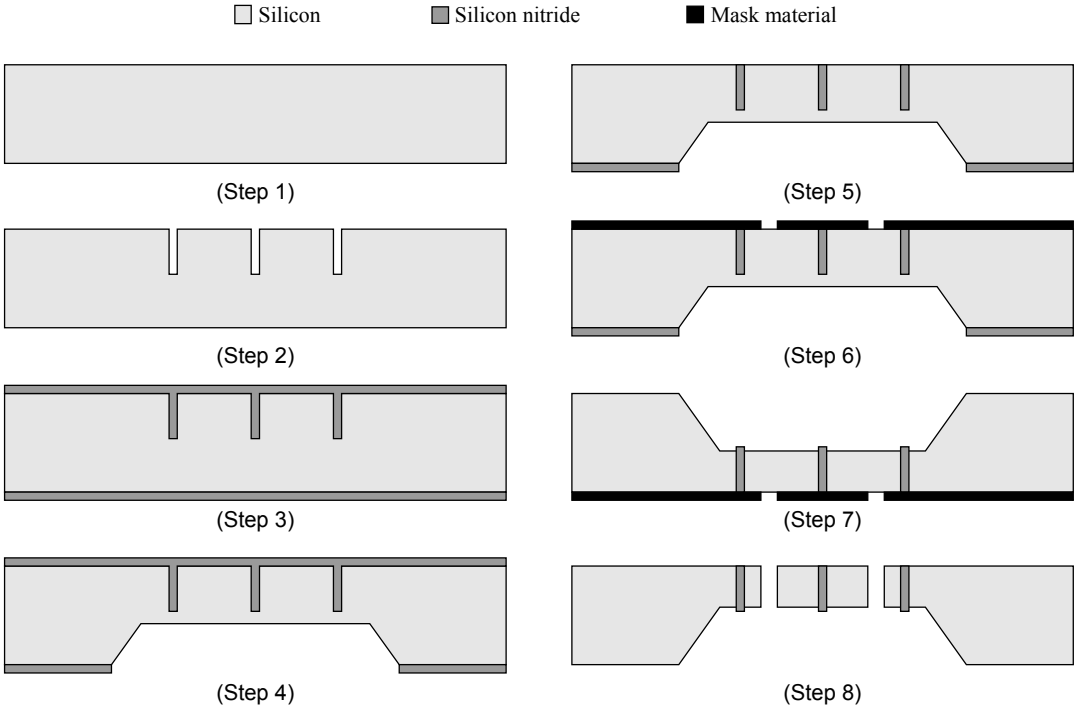

Figure 4.1: A bulk micromachining process for MEMS fabrication in standard silicon wafers by combining vertical trench isolation and backside etching.

The three–mask fabrication process starts on a <100> oriented, single crystal silicon wafer (*Step 1*). Vertical trench isolation is defined in the wafer by a deep plasma etch (*Step 2*) and subsequent refill with low-stress LPCVD silicon nitride (*Step 3*). After the definition of vertical trench isolation, a silicon membrane is formed by wet anisotropic etching from the backside of the wafer (*Step 4*). The silicon nitride, which was deposited as the backfill material for trench isolation, is used as the backside etching mask and top-side protection layer. After removal of the silicon nitride from the top surface (*Step 5*), a structural layout is patterned on

the silicon membrane (*Step 6*). Next, a plasma etch is performed on the flipped wafer to thin the silicon membrane down to the desired final thickness (*Step 7*). In the last fabrication step, micromechanical structures are etched in the silicon membrane by deep plasma etching (*Step 8*).

The described process allows fabrication of high-aspect-ratio monocrystalline MEMS with embedded vertical trench isolation. The fabrication sequence is fully compatible with standard CMOS process permitting full integration of MEMS with on-chip electronics as demonstrated by Yan [3]. A portion of a fabricated comb drive actuator, which is electrically insulated from the bulk material by vertical trench isolation, is shown in Fig. 4.2.

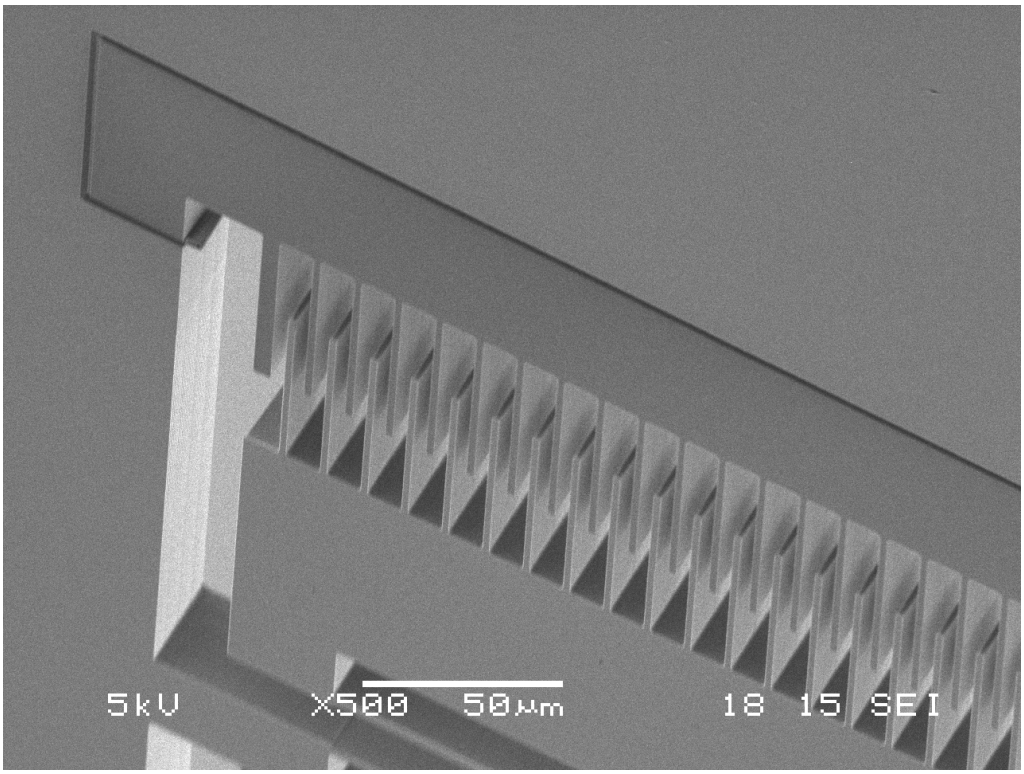

Figure 4.2: SEM micrograph of a comb drive with trench isolation fabricated in a standard monocrystalline silicon wafer by the backside release method.

The use of a backside etch to release microstructures with integrated trench isolation has several advantages over the release methods based on the removal of sacrificial silicon oxide layer (Chapter 2) and the lateral undercutting by isotropic plasma etch (Chapter 3). The microstructures etched in a silicon membrane formed

by a backside etch are automatically released. A separate release step, e.g. to remove sacrificial oxide layer or to undercut microstructure by an isotropic plasma etch, is not required. Furthermore, etching holes are not needed for a successful release. This simplifies the mask design and allows the fabrication of microstructures with large non-perforated areas. Finally, the backside release is less susceptible to the ARDE and the notching effects, resulting in microstructures with a uniform height and a smooth underside.

The abovementioned advantages come at the cost of increased complexity in the fabrication process and an additional lithography step that requires a proper front-to-back side alignment.

4.3 DESIGN AND PROCESSING ISSUES

The important design and processing issues concerning the trench isolation in general are discussed in Section 2.3. This section examines the issues related to two critical fabrication steps inherent to the backside release: the formation of a silicon membrane and the etching of micromechanical structures in this membrane. It also addresses the method for connecting a fabricated MEMS device with measurement equipment for testing purposes.

4.3.1 Membrane formation

Once isolating trenches are etched (*Step 2*) and completely refilled (*Step 3*), the backside etching of the wafer results in a silicon membrane with a desired final thickness. This final thickness, which is directly related to the depth of isolating trenches, determines the height of micromechanical structures. The height of microstructures is thus a process variable, which can be adjusted to a certain extent on demand, thereby increasing design flexibility.

Wet anisotropic etching, deep plasma etching or a combination of these two etch techniques can be employed to successfully create a membrane with integrated vertical trench isolation in a silicon wafer.

The wet anisotropic etch of a <100> silicon wafer in potassium hydroxide (KOH) or tetramethyl ammonium hydroxide (TMAH) solution [4] is an inexpensive and well-established etching technique, which is highly suitable for the formation of silicon membranes with uniform thickness. In spite of a low etching rate (~ 1μm/min), a high throughput can be achieved by parallel

processing of a large number of wafers. Furthermore, the silicon nitride, used as a refill material for the trench isolation, is an ideal masking layer for the wet anisotropic etching in KOH solution.

A single wet anisotropic etch can be used to reduce the membrane to the desired thickness [3]. In this case, a separate plasma etch (*Step 7*) is not required. The wet etching proceeds until the bottom of isolating trenches is visible. The trench bottom serves as a visual mark for the end-point detection. The visual control and the possibility to lower the removal rate of the etch solution in the final etching stage (e.g. by lowering the temperature) allow a good control of the final thickness of the membrane.

Compliant membranes with a relatively large area and relatively small thickness can be damaged during the patterning of the structural layout (*Step 6*). In addition, a deflection of the compliant membrane during the mask exposure can result in inaccurate patterning. For vulnerable membranes, the wet anisotropic etching is performed only above a certain membrane thickness (*Step 4*) that allows safe handling afterwards. This intermediate thickness depends on the size and the geometry of the membrane, which are fully determined by the size and the geometry of the intended MEMS device. After the patterning of the structural layout (*Step 6*), a plasma etch is performed on the flipped wafer to thin the membrane down to the final thickness. The underside of isolating trenches serves as an end-point detection mark. A released micromechanical structure, which is machined in a silicon membrane formed by a combination of a wet and plasma etch, is shown in Fig. 4.3.

Optionally, a silicon membrane can be formed entirely with a plasma etch (*Step 8*) as demonstrated in [4]. In this case, a wet anisotropic etch (*Step 4*) is not needed. This technique is particularly useful when the available space on the wafer is a concern. In comparison to wet anisotropic etching, plasma etching uses less die area and is not affected by crystal orientation. Although plasma backside etching can be performed on the same plasma system that is used for the isolation and structural trenches, it may remain a time-consuming process, depending on equipment and recipes.

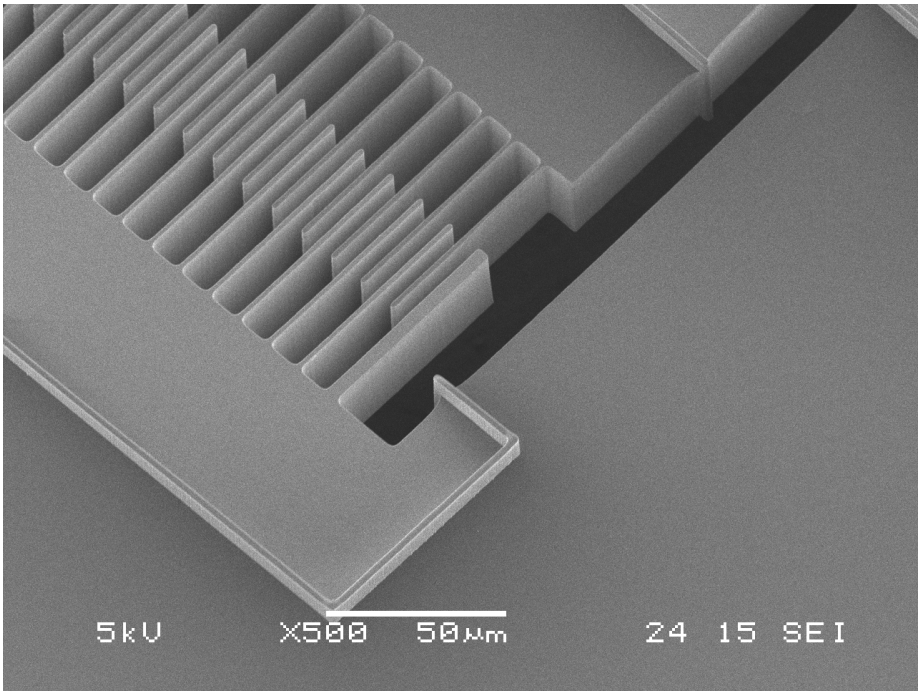

Figure 4.3: SEM micrographs of the backside of a comb drive actuator machined in a silicon membrane. The membrane was formed by a combination of wet anisotropic (KOH) and plasma etching.

4.3.2 Structural etching

In the fabricated silicon membrane, released micromechanical structures are machined by plasma etching (*Step 8*). Deep reactive ion etching (DRIE) is used to allow directional etching all the way through a relatively thick silicon membrane [4-9], thus enabling fabrication of high-aspect-ratio microstructures. Diverse masking materials can be employed depending on the membrane thickness and the selectivity of the etch process. In our process, we used chromium as etching mask to assure high selectivity. A chromium mask and metallic masks in general short-circuit all microstructures previously insulated with vertical trench isolation, so it needs to be completely removed after the etching.

In plasma etching, different etching rates for different opening areas are induced by the ARDE effect. As a consequence, the large opening areas are etched through the silicon membrane much faster than the small areas. Due to the difference in etch rates some amount of overetch time must be introduced into the etching process. The overetching can cause structural damage through several

different effects, such as (micro)loading [10], charging [7,8] or limited thermal stability [11].

The loading, which is the silicon area exposed to the plasma glow, is drastically reduced once the etching is performed through the membrane. Reduced loading increases the global reactant concentration on the wafer surface, which can give rise to an enhanced lateral underetching and ultimately a severe damage of micromechanical structures [10]. This unwanted underetching could also occur locally (microloading) due to the difference in etch rates of silicon for different opening areas induced by the ARDE effect. When the large opening areas are completely etched through the silicon membrane, the local reactant concentration increases, giving rise to lateral underetching.

To suppress the (micro)loading effect, the device wafer is temporarily mounted on a dummy silicon wafer during the plasma etch, as schematically shown in Fig. 4.4.

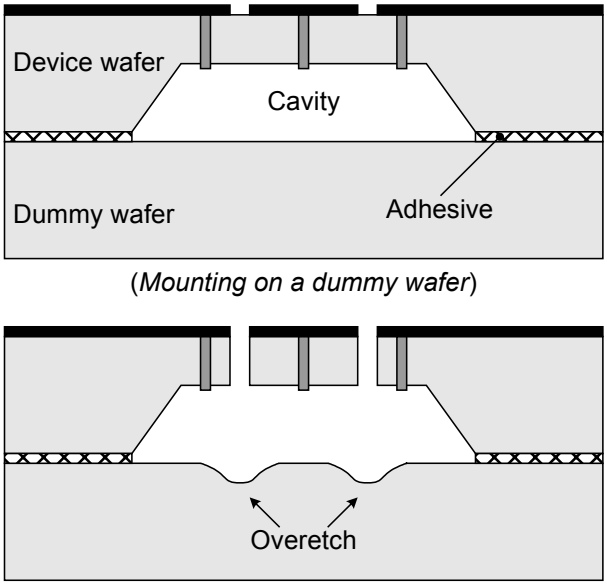

Figure 4.4: The device wafer is mounted on a dummy silicon wafer during the structural etching.

We used diffusion pump oil as an adhesive material to temporarily bond two wafer surfaces together. Alternatively, photoresist [3,5] and black wax [9] can be employed as adhesive materials. The cavity formed by the backside etch allows an

easy mounting without interference with the microstructures formed in the silicon membrane. The diffusion pump oil is afterwards removed using an acetone cleaning.

By employing a silicon dummy wafer, the loading and the reactant concentration remain practically unaltered even if the membrane is completely etched through. The etching process, once completed in the membrane, simply continues in the dummy wafer causing some etch in the dummy wafer surface (see Fig. 4.5). Using this procedure, significant damage of the microstructures from the (micro)loading effect is efficiently avoided.

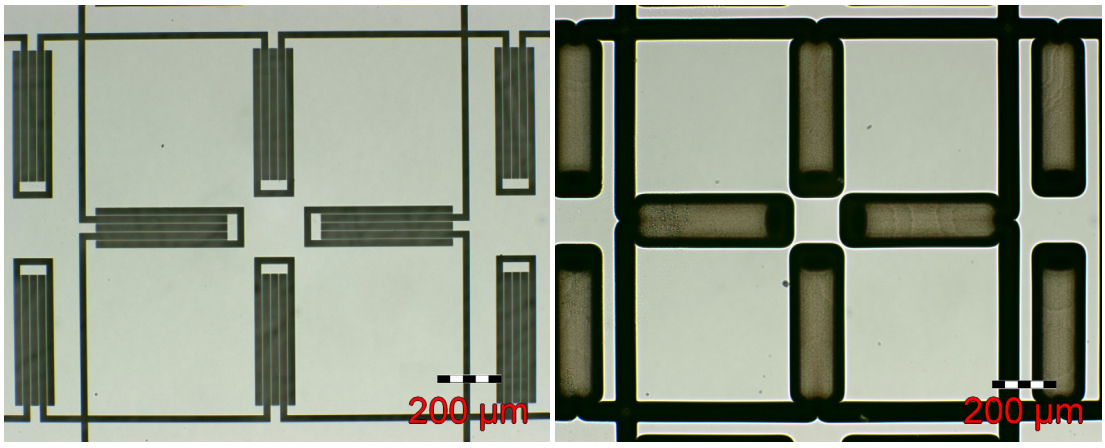

Figure 4.5: (left) Microstructures machined in a silicon membrane, (right) The overetching of the dummy silicon wafer.

The silicon dummy wafer, used to protect the microstructures from the (micro)loading effect, also prevents charge accumulation during ion bombardment. For example charge accumulation on glass dummy wafers causes undesired etching from the backside and severe structural damage [7,8]. Additionally, the silicon dummy wafer allows the use of helium backside cooling to provide an accurate temperature control on the wafer during the etching. The temperature control is needed to assure a proper etch profile, which generally has a strong temperature dependency.

The (micro)loading and the charging are not the only effects that can cause structural damage during overetching. A limited thermal stability of the fluorocarbon (FC) passivation layer can also induce accelerated lateral etching of

large area structures suspended by slender flexures [11]. During the etching of microstructures in a silicon membrane, heat is generated due to bombardment of the wafer surface by ions from the plasma glow. As long as the etching through the silicon membrane is not completed, as illustrated in Fig. 4.6 (a), heat can easily diffuse through the remaining silicon, preventing (local) excess temperature increase.

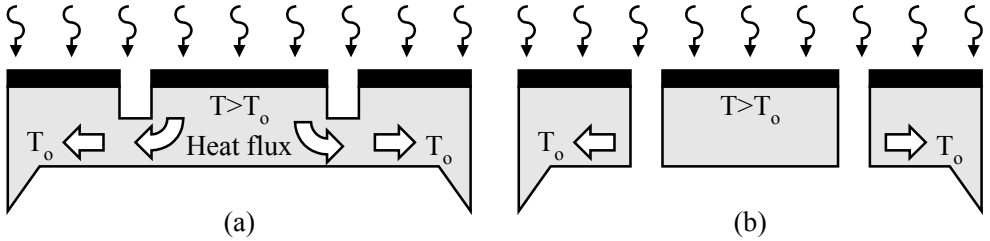

Figure 4.6: A bulk micromachining process for MEMS fabrication in standard silicon wafer by combining vertical trench isolation and backside etching.

However, when the microstructures are completely released, as shown in Fig. 4.6 (b), any generated heat must be conducted through flexure suspensions. Limited heat conduction will dramatically increase the temperature of slender suspension causing the FC passivation to fail. A slender flexure, which is damaged by this thermal effect, is shown in Fig. 4.7.

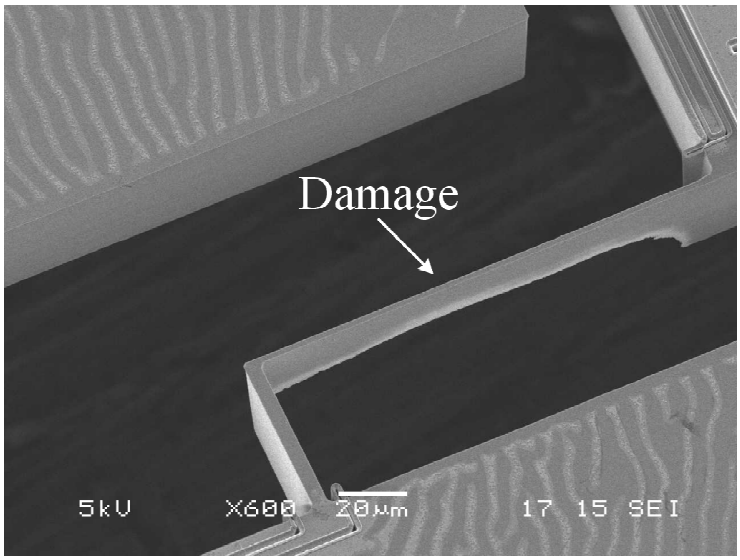

Figure 4.7: SEM micrograph of a silicon flexure damaged by thermal effects.

The thermal effect mentioned above can be suppressed by several means. First, the overetch time can be reduced by eliminating or suppressing the ARDE effect. This can be achieved by a proper mask design with uniform opening areas. Second, the etching process can be optimised by reducing the discharge power and/or by lowering the etch temperature [11]. Finally, temporarily connecting suspended structures to each other and/or to surrounding bulk material allows heat conduction and reduces temperature of the passivation layer [13]. These conductive paths must be later interrupted to prevent undesired short-circuiting. Suitable techniques utilize the die separation or singulation operation and silicon fuses.

4.3.3 Interconnects

After the fabrication, diverse tests must be performed on manufactured MEMS devices to characterize their performance. In the development stage it is important to have the possibility to perform these tests on a wafer level. Sharp probe needles are commonly used to provide electrical connection between contact pads of a MEMS device and measurement equipment. Vertical trench isolation can be employed to define suspended contact pads in the silicon membrane, as illustrated in Fig. 4.8 (a). Large mechanical strength of a suspended contact pad allows the use of a probe needle to establish electrical connection. The free side of a contact pad is used to connect functional parts of the microdevice.

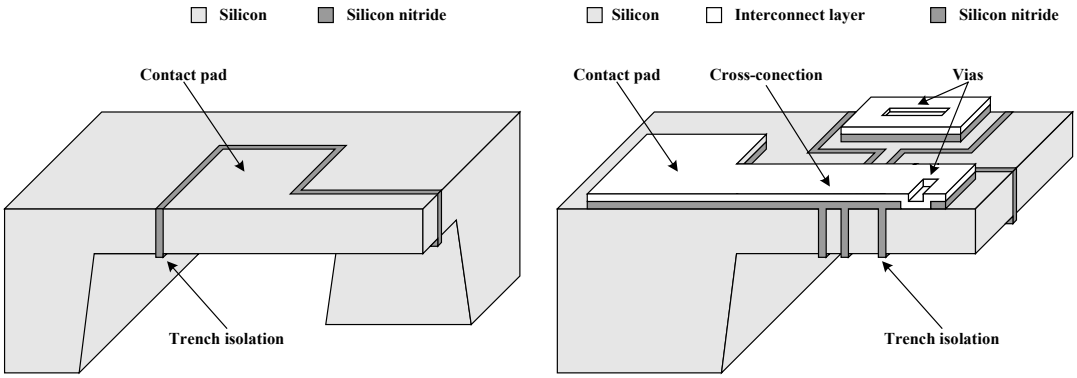

Figure 4.8: Cross-sections of (a) a contact pad formed by refilled trenches, (b) embedded interconnects to address microstructures.

A more advanced approach to interfacing a MEMS device with a measurement set-up is the use of metal or polysilicon interconnects, as shown in Fig. 4.8 (b). The interconnects can be realized as a part of the electronic integration process or at the cost of two additional photolithography masks (see Section 2.3). By employing embedded interconnects, contact pads are moved from the silicon membrane to the bulk material, allowing wire bonding. Furthermore, interconnects provide electrical connection between distinct isolated microstructures, allow full integration with on-chip electronics by connecting the integrated circuits and the microstructures and enable multiple level electrical interconnects (cross-connections) to be realized.

4.4 FABRICATION AND APPLICATIONS

To demonstrate the feasibility of the presented technology, various electrostatic microactuators are fabricated.

4.4.1 Fabrication

The three–mask fabrication process starts on a four inch, <100> oriented, single crystal silicon wafer (*Step 1*). A single side polished wafer with a thickness of 500 μm is used. A highly conductive wafer is selected to ensure good electrical conductivity of the bulk material. In the selected wafer, 35 μm deep and 2 μm narrow trenches are (*Step 2*) etched using Deep Reactive Ion Etching (DRIE). A 40 nm thick chromium layer is used as a masking material. After removal of the chromium mask, a 1.5 μm low-stress LPCVD silicon nitride layer is deposited on the patterned wafer to completely refill the trenches and form a mask layer at the same time (*Step 3*). In the next fabrication step, a window in the silicon nitride layer is defined on the backside of the wafer by photolithography, followed by directional RIE using CHF_3 plasma chemistry. After removal of the photoresist in an HNO_3 solution, a wet anisotropic etch was carried out in a 25% potassium hydroxide (KOH) solution at a temperature of 75 °C (*Step 4*). The time-controlled etch was performed for 6.5 hours leaving a 110 μm thick single crystal silicon membrane. Subsequently, the silicon nitride layer was removed from the top surface by a blanket RIE etch, leaving the silicon nitride only in the refilled trenches (*Step 5*). A structural pattern was transferred in a second 40 nm thick chromium layer serving as a hard etching mask (*Step 6*). Plasma etching of the

backside of the wafer was performed on the flipped wafer to thin the silicon membrane until the trench isolation was visible (*Step 7*). The final thickness of the membrane was 30 μm. Another plasma etch, performed from the front side in the same plasma system, was used to define and release micromechanical structures in the silicon membrane (*Step 8*). The wafer was temporarily mounted on a dummy silicon wafer by diffusion pump oil. The fabrication process is terminated by removal of the chromium mask by a sputter-etching in an oxygen plasma.

4.4.2 XY-scanner

Electrostatic XY-scanners driven by comb drive microactuators [1,2] are well suited for the positioning of a recording medium in probe-based data storage. Microscanners with a relatively large movable stage are favoured, because they maximize the effective recording area. An XY-scanner with a large non-perforated stage, manufactured in the presented fabrication process, is shown in Fig. 4.9.

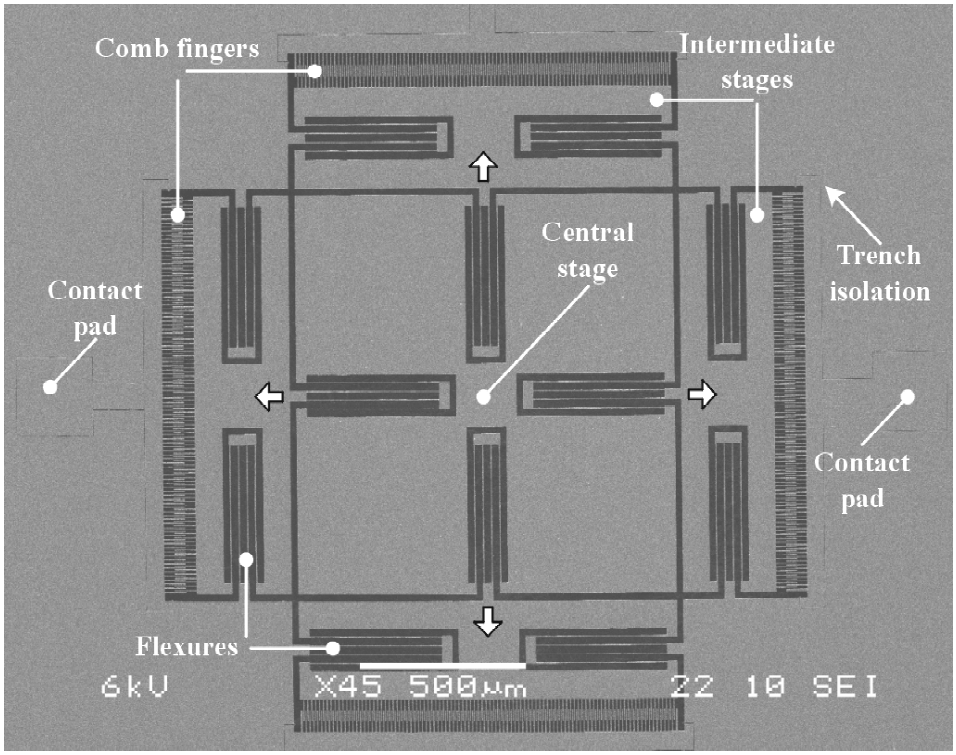

Figure 4.9: SEM micrograph an electrostatic X-Y scanner with a non-perforated central stage.

The whole XY-scanner, machined in a 30 µm thick silicon membrane, fits in an area of 2 mm x 2 mm. The scanner consists of a movable central stage, which is driven by electrostatic comb drive actuators. The non-perforated central stage occupies 29 % of the total scanner area, which is roughly three times more than the previously reported area efficiency of less then 10 % [1]. Each comb-drive actuator consists of 194 fingers, which are 66 µm long and 2.6 µm wide. The gap and the overlap between comb fingers are 3.6 µm and 34 µm, respectively. Comb drive actuators are suspended by folded flexures, which are 410 µm long and 2.6 µm wide. Four intermediate stages and a flexure mechanism are employed to provide a decoupled, orthogonal motion of the central stage. A bi-axial motion of the central stage is shown in Fig. 4.10. The XY-stage was designed for a maximum displacement of ±20 µm in both X and Y directions.

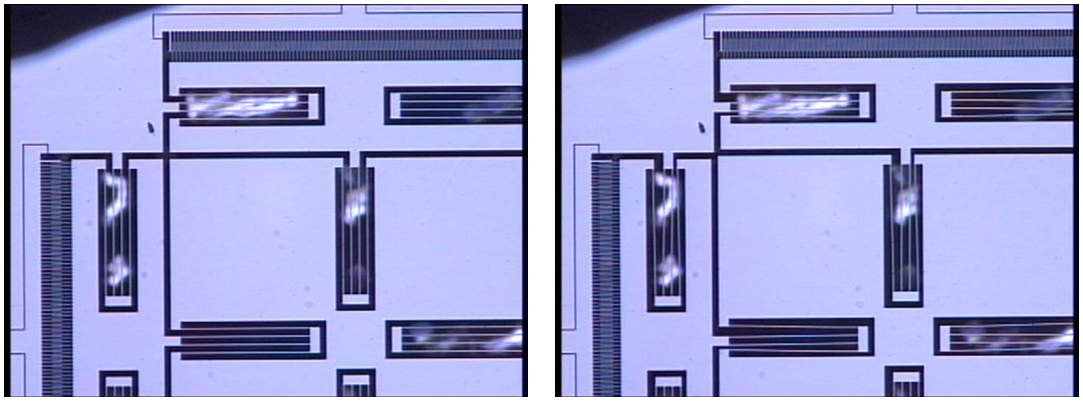

Figure 4.10: Motion of the central stage: (left) initial position, (right) stage moved up and left.

Fig. 4.11 shows the displacement of the stage as a function of the driving voltage applied on a single comb-drive actuator. The displacement measurement is performed using an image processing technique based on the Fourier transform [14]. An actuator voltage of 102 V was required to achieve the maximum displacement. Young's modulus of single crystal silicon of 178 GPa is extracted from the measurements, which is in good agreement with the value founded in the literature [4].

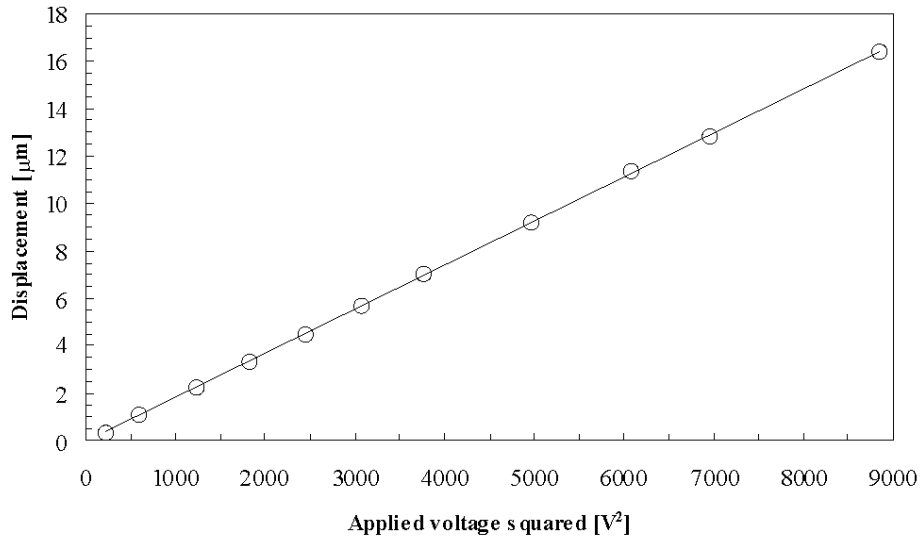

Figure 4.11: Measured displacement of the central stage as a function of the driving voltage.

As expected from the theory [14], the displacement of the stage was proportional to the square of the voltage applied on the comb-drive.

4.4.3 Stacked XY-scanner

The XY-scanner, presented in the previous section, employs four intermediate stages and a flexure mechanism to decouple x and y motion. An alternative design, shown in Fig. 4.12, employs a stacked assembly to achieve decoupled motion along two perpendicular in-plane axes. In the stacked assembly, a movable central stage is mounted perpendicularly inside a movable shuttle, resulting in an entirely decoupled motion in X and Y directions. The non-perforated central stage occupies 28 % of the total scanner area. The scanner is machined in the 30 μm thick silicon membrane and measures 2000 μm x 1200 μm. The shuttle and central stage, which are suspended by folded flexures, are each driven by a pair of electrostatic comb-drive actuators. The same dimensions as in the previous section are used for the comb drive actuators and folded flexures. Number of folded flexures in each direction is reduced from six in the previous design to four, resulting in lower stiffness.

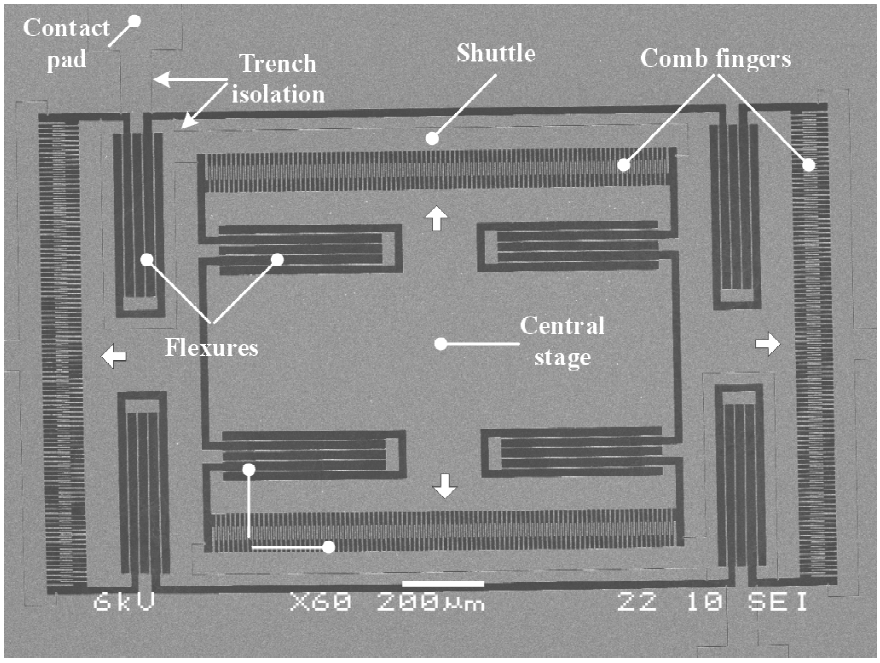

Figure 4.12: SEM micrograph of a XY-stage with the stacked assembly.

Vertical trench isolation integrated on the movable shuttle, as shown in Fig. 4.13, allows independent excitation of the central stage.

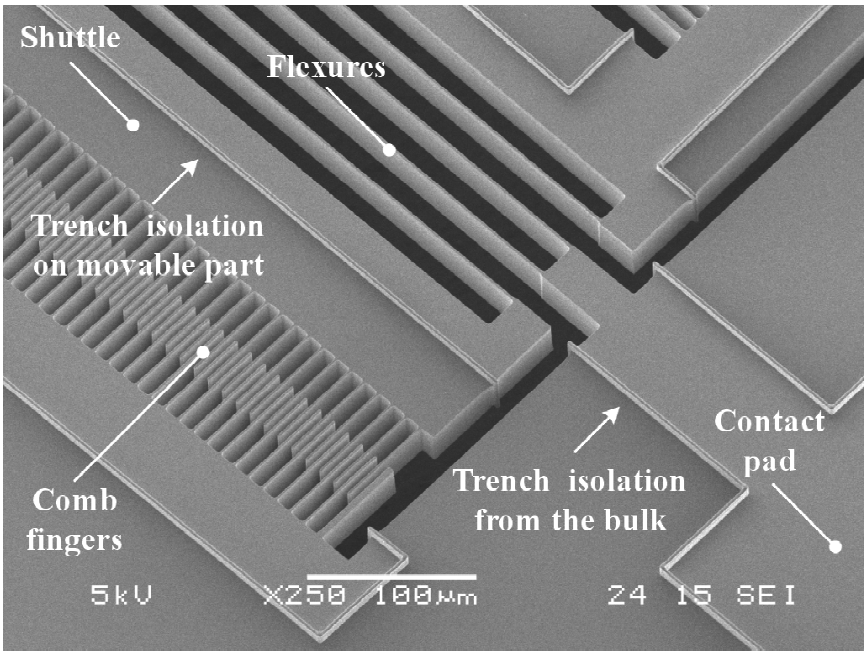

Figure 4.13: SEM micrograph of the backside a XY-stage with the stacked assembly.

The scanner is successfully operated, as shown in Fig. 4.14. A maximum displacement of ±20 µm is achieved with an actuation voltage of 88 V.

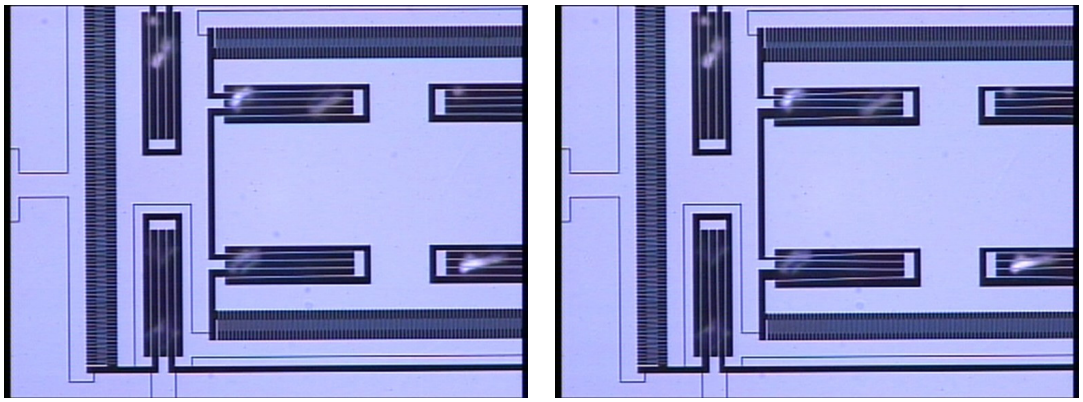

Figure 4.14: Motion of the central stage of a XY-scanner with stacked assembly: (left) initial position, (right) central stage moved down and left.

The displacement curve as function of the voltage squared is shown in Fig. 4.15.

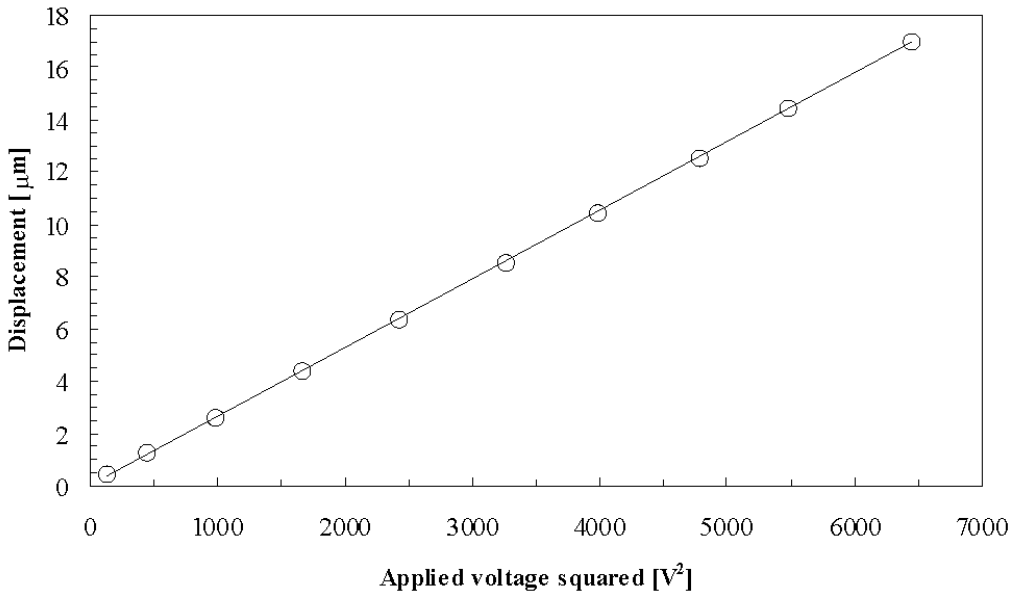

Figure 4.15: Measured displacement of the central stage of the XY-scanner with stacked assembly as a function of the driving voltage.

4.4.4 Contraction beams actuator

A contraction beams actuator, already introduced in Section 2.5.1, converts a lateral deflection of a large number of elastic beams into a powerful longitudinal step. This electrostatic microactuator is highly suitable for step generation in a stepper micromotor because of its finely resolved steps, fast response, large output force and small size. An improvement in the output force and response time/speed of this microactuator for a given drive voltage can be achieved by increasing the height of beams.

We have employed the backside release to fabricate a contraction beams actuator with a large beam height in a single crystal silicon. The microactuator, shown in Fig. 4.16, consists of 20 beams. The beams in the array, 2500 μm long, 10 μm thick and 30 μm tall are electrically insulated, allowing the application of a voltage difference between neighbouring beams. The initial gap between beams was 10 μm.

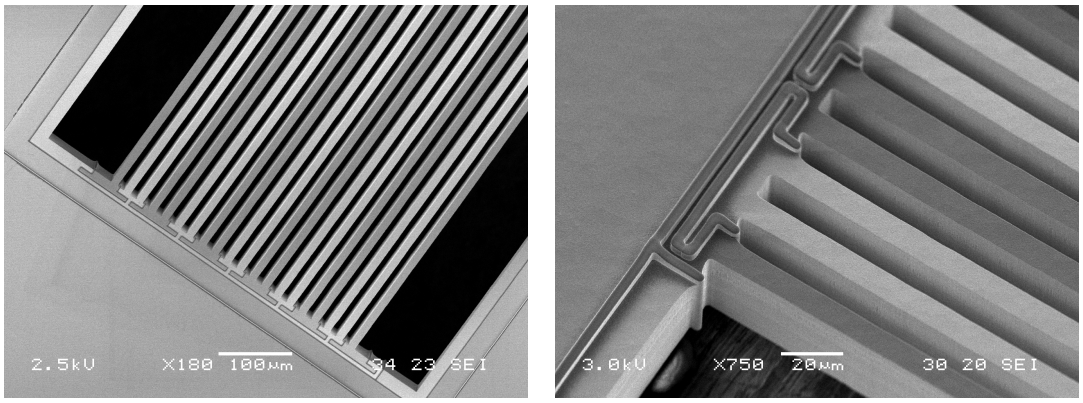

Figure 4.16: SEM micrographs of a contraction beams actuator made in monocrystalline silicon. The beams are successfully insulated using vertical trench isolation (left) front side (right) backside of microactuator.

The actuator is successfully operated above the pull-in voltage of 48 V. A single step of 50 nm at 50 V is measured. The measurement is performed using an image processing technique with a resolution of a few nanometers [14]. A theoretical estimate for the force produced by these actuators is 10 mN [16]. This type of actuator can be integrated in an stepper micropositioning system, similar to the one proposed by Konishi S. et al. [17]. In contrast to [17], which utilizes a

piezoactuator, the contraction beam actuator is compatible with the fabrication process used for the electrostatic clamps, enabling batch fabrication of the entire micropositioning system.

4.5 CONCLUSIONS

A bulk micromachining technology for fabrication of high-aspect-ratio monocrystalline microstructures with embedded vertical trench isolation in a standard silicon wafer is presented. The technology is suitable for full integration with on-chip electronics. The backside etching, employed for the release, produces microstructures with large non-perforated areas and uniform height. The height of microstructures is a process variable, which can be easily adjusted with the proposed technology. Low cost of the starting substrate and large design flexibility make this technology highly suitable for MEMS design and fast prototyping. Working electrostatic microactuators, fabricated using the proposed process, have been successfully demonstrated.

4.6 REFERENCES

1 Kim C H, Jeong H M, Jeon J U and Kim Y K 2003 Silicon micro XY-stage with a large area shuttle and no etching holes for SPM-based data storage *J. Microelectormech. Syst.* **12**(4) 470-478

2 Alfaro J F and G K Fedder 2002 Actuation for probe-based mass data storage *Int. Conf. on Modeling and Simulation of Microsystems* **1** 202-205

3 Yan G, Zhu Y, Wang Z, Zhang R, Chen Z, Liu X and Wang Y Y 2004 Integrated bulk-micromachined gyroscope using deep trench isolation technology *Int. Conf. on Micro Electro Mechanical Systems* (MEMS 2004) (Maastricht, The Netherlands) pp. 605-608

4 Kovacs G T A, Maluf N I and Petersen K E 1998 Bulk micromachining of silicon *Proceedings of the IEEE* **86**(8) 1536-1551

5 Xie H, Erdmann L, Zhu X, Gabriel K J and Fedder G K 2002 Post-CMOS processing for high-aspect-ratio integrated silicon microstructures *J. Microelectromech. Syst*. **11**(2) 93-101

6 Klaassen E H, Petersen K, Noworolski J M, Logan J, Maluf N I, Brown J, Storment C, McCulley W and Kovacs G T A 1996 Silicon fusion bonding and deep reactive ion etching: a new technology for microstructures *Sensors Actuators* A **52** 132-139

7 Chabloz M, Jiao J, Yoshida Y, Matsuura T and Tsutsumi K 2000 A method to evade microloading effect in deep reactive ion etching for anodically bonded glass-silicon structures *Int. Conf. on Micro Electro Mechanical Systems* (MEMS 2000), (Miyazaki, Japan) 283-287

8 Chae J, Kulah H and Najafi K 2005 A CMOS-compatible high aspect ratio silicon-on-glass in-plane micro-accelerometer *J. Micromech. Microeng*. **15** 336-345

9 Amini B V, Pourkamali S and Ayazi F 2004 A high-resolution, stictionless, CMOS compatible SOI accelerometer with a low noise, low power, 0.25 μm CMOS interface *Int. Conf. on Micro Electro Mechanical Systems* (MEMS 2004) (Maastricht, The Netherlands) pp. 572-575

10 Jansen H 1996 Plasma etching in microtechnology *PhD Thesis* University of Twente, The Netherlands, ISBN 903650810x

11 Bertz A, Küchler M, Knöfler R, Gessner T 2002 A novel high aspect ratio technology for MEMS fabrication using standard silicon wafers *Sensors Actuators* A **97-98** 691-701

12 Chase TA and Christenson JC 2002 Deep reactive ion etching process and microelectromechanical devices formed thereby *United States Patent* US 6,500,348 B2

13 Dijkstra P, Puech M, Launay N, Arnal N, Rolland L and Gruffat J M 2003 New development in silicon and oxide ICP etching for MEMS *14th Micromechanics Europe Workshop* (MME03) (Delft, The Netherlands) 107-110

14 Vanapalli S 2004 Techniques for characterization of in-plane displacement for microactuators *M.Sc Thesis* Department of Electrical Engineering, University of Twente, The Netherlands

15 Legtenberg R, Groeneveld A W and Elwenspoek M 1996 Comb-drive actuators for large displacement *J. Micromech. Microeng*. **6** 320-329

16 Sarajlic E, Berenschot E, Krijnen G and Elwenspoek M 2003 Low volume, large force (>1mN) and nanometer resolution, electrostatic microactuator for low displacement applications *Nanotechnology Conference and Trade Show* (NANOTECH 2003) (San Francisco, USA) **1** 637-640

17 Konishi S, Ohno K and Munechika M 2002 Parallel linear actuator system with high accuracy and large stroke *Sensors Actuators* A **97-98** 610-619

Chapter 5

Double side release and vertical trench isolation

Abstract

In this chapter we present another bulk micromachining technology for MEMS fabrication based on standard single crystal silicon wafers and vertical trench isolation. This technology, which is fully suitable for integration with on-chip electronics, employs double-side processing to completely release micromechanical structures machined in the bulk silicon. Etching and release of microstructures are performed in a single plasma chamber allowing dry, low temperature processing. Utilizing double-side release, high-aspect-ratio monocrystalline MEMS with integrated vertical electrical insulation are fabricated on one side of the wafer and, at the same time, mechanically and electrically coupled with released micromechanical structures on the opposite side. This opens new design opportunities to improve performance and functionality of MEMS devices. The presented technology is employed for fabrication of an electrostatic XY-scanner for probe-based data storage with a significantly larger effective recording area proving the feasibility and large potential of this technology.

5.1 INTRODUCTION

Two distinct bulk micromachining technologies for MEMS fabrication in a standard silicon wafer have already been introduced in the previous chapters. Both employ vertical trench isolation to assure electrical insulation between movable microstructures, which are mechanically linked via fixed or flexible connection. Two different methods are used to release microstructures with integrated vertical trench isolation. The first release method, presented in Chapter 3, employs an isotropic plasma etch to laterally undercut microstructures defined in the bulk material. The second, introduced in Chapter 4, uses backside etching to form a silicon membrane in which microstructures are etched and automatically released.

In this chapter we present another bulk micromachining technology for MEMS fabrication based on standard single crystal silicon wafers and vertical trench isolation. This technology, which is also fully suitable for integration with on-chip electronics, employs double-side processing to completely release a micromechanical device machined in the bulk silicon. Utilizing the double-side release, high-aspect-ratio monocrystalline microstructures with embedded vertical trench isolation are fabricated on one side of the substrate and at the same time mechanically and electrically linked with released micromechanical structures on the other side. The ability to mechanically and electrically couple microstructures on both sides of the wafer opens new design opportunities to realize MEMS with increased performance and functionality.

In the following sections, we explain the basic fabrication steps of this bulk micromachining technology. Subsequently, we demonstrate the feasibility and potential of this technology by describing a successful realization of an electrostatic XY-scanner for probe-based data storage with a significant large effective recording area of 76%.

5.2 DOUBLE SIDE RELEASE

The basic fabrication steps of the bulk micromachining technology utilizing a double side release are illustrated in Fig. 5.1. An isotropic plasma etch from the front side of the wafer, followed by a backside etch, are employed to completely release microstructures with integrated vertical trench isolation machined in the bulk silicon.

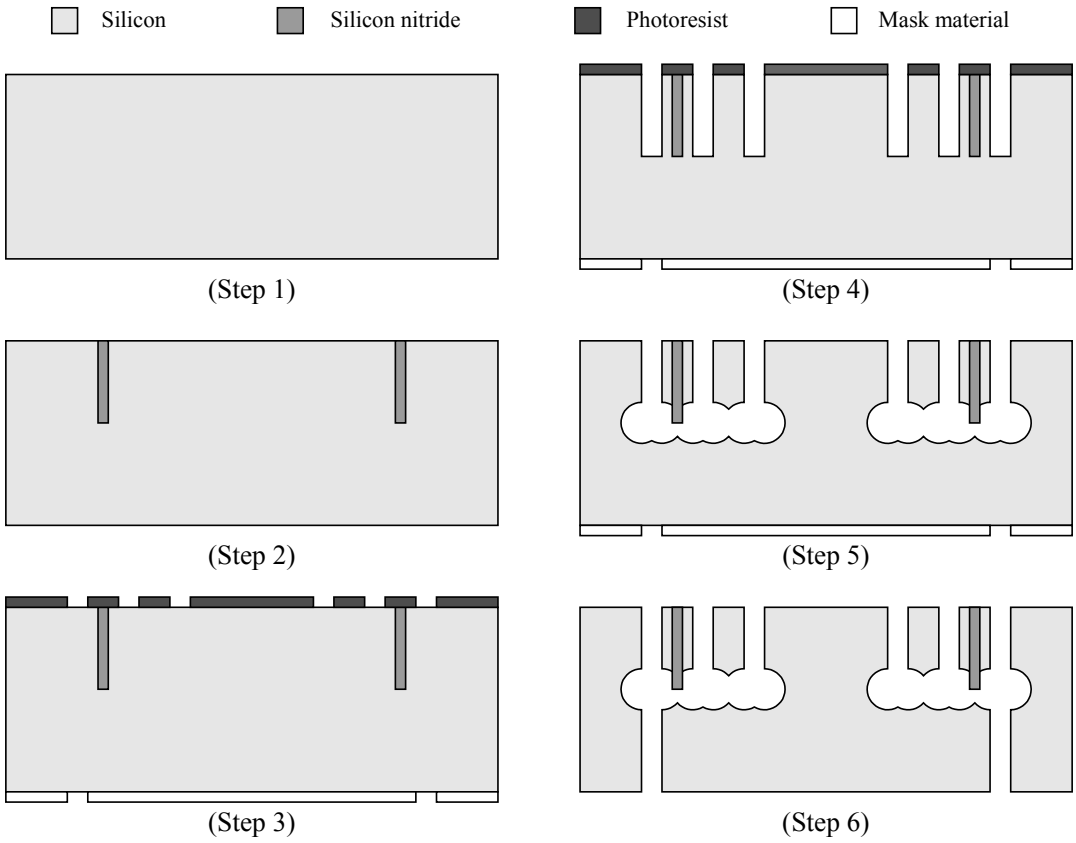

Figure 5.1: A bulk micromachining technology for MEMS fabrication based on standard silicon wafer and vertical trench isolation. A double-side processing is employed to fully release microstructures machined in the bulk material.

A three–mask fabrication process starts on a standard single crystal silicon substrate with an arbitrary crystallographic orientation (*Step 1*). In the selected substrate, isolating trenches are etched by deep reactive ion etching (DRIE) and subsequently refilled with a dielectric material. We deposit a low-stress LPCVD silicon nitride layer to refill isolating trenches because of its favourable electrical insulating properties and highly conformal deposition. A silicon oxide layer, which is compatible with the rest of the fabrication process, can be used alternatively as the backfill material.

The backfill material from the top surface of the substrate is removed by a maskless directional etching step (*Step 2*). The surface of the substrate remains flat and smooth after the etching, allowing further processing. This may include

integration of on-chip electronics and/or embedded interconnects (see Section 2.3).

After removal of the backfill material from the top surface, photolithographic patterning is performed on both sides of the substrate requiring a double-side alignment (*Step 3*). The photoresist pattern on the backside of the substrate is transferred into a previously applied layer, serving as an etching mask in a subsequent DRIE step. Various masking materials can be employed, depending on the required etching depth and the selectivity of the etch process. We use a silicon oxide layer, deposited by Plasma Enhanced Chemical Vapor Deposition (PECVD), as a masking material. Silicon oxide is a common choice of masking material, as it allows deep trench etching due to its high selectivity in the silicon DRIE process.

After patterning, the structural layout on the top side of the substrate is etched into the bulk silicon (*Step 4*) and subsequently released using an isotropic plasma etch to laterally undercut microstructures (*Step 5*). We employ the advanced plasma processing, already discussed in Chapter 3, to etch, passivate and release microstructures in one and the same plasma system during a single etch run. This method allows the fabrication of released, high-aspect-ratio microstructures using dry, low temperature processing. The final height of the microstructures is determined by the structural etch depth and the duration of the isotropic etch step. These two process parameters must be adjusted for the depth of the isolating trenches in order to assure proper electrical insulation on movable components (see Section 3.3). Microstructures with a width below a certain maximum, which is directly related to the duration of the isotropic etch step, are completely laterally undercut during plasma release; wider microstructures are only partially undercut in this release process, remaining anchored to the underlying bulk silicon. A large gap (tens of micrometers) between the underlying silicon and the released structures, which are often at different electrical potential during operation, can be achieved strongly reducing the vertical interaction due to electrostatic forces.

After the plasma release, the structural pattern on the backside of the substrate is etched using a DRIE process (*Step 6*). Backside etching is performed all the way through the remaining silicon layer located beneath the microstructures previously machined on the front side of the substrate. Prior to backside etching, the

microstructures on the front side are uniformly coated with a fluorocarbon (FC) film, which acts as a protection layer when the silicon layer is completely etched through. The FC layer is deposited in the same plasma system used for the DRIE processing.

In the last fabrication step, the silicon oxide mask as well as the photoresist mask and the FC passivation layer are removed using respectively a silicon oxide plasma etching and an oxygen plasma cleaning followed by a thermal ashing step.

5.3 APPLICATIONS

The bulk micromachining technology presented in the previous section allows fabrication of high-aspect-ratio, monocrystalline silicon microstructures with embedded vertical trench isolation. These microstructures, machined on one side of the substrate, can be mechanically and electrically coupled with released micromechanical structures on the other side. This enables realization of functional microstructures on both sides of the substrate, opening new design opportunities.

There are many types of MEMS devices that can benefit from the unique possibilities offered by this technology, such as highly sensitive capacitive inertial sensors with a large proof mass (substrate thickness) or electrostatic XY-scanners with a large area efficiency for probe based data storage. In this section, we will only discuss the later application. The former one is currently under investigation and will be reported elsewhere.

5.3.1 Two-level electrostatic XY-scanner

The basic principle behind probe-based data storage (see Chapter 1) is to access a recording medium placed on a movable stage with a large array of stationary micromechanical probes. A high-performance medium positioner is required to successfully implement the probe-based data storage concept and achieve significant performance improvements over conventional data storage devices

Electrostatic XY-scanners are considered suitable candidates to perform this demanding positioning task [1-4]. In general, these scanners consist of a suspended movable stage driven by two pairs of comb-drive microactuators in two orthogonal directions. Several working prototypes have already been demonstrated

[2,3, Chapter 4] with a relatively large displacement range and good vertical stability provided by their substantial microstructure height.

All previously reported electrostatic XY-scanners have been built in a single device layer, with all components at the same level, resulting in a relatively simple design. A serious drawback of the single-level electrostatic XY-scanners is low area efficiency. The comb-drive actuators and the spring suspension consume a large part of the total scanner area, leaving only a small part for the movable stage where the recording medium can be deposited. Therefore, only a relatively small portion of the total scanner area can actually be used for data storage. The area efficiency for the single-level electrostatic XY–scanners is typically less than 30 % , as the one shown in Section 4.5.2.

We present an electrostatic XY-scanner for probe-based data storage with an area efficiency close to 100 %. The XY-scanner, schematically drawn in Fig. 5.2, is built in two levels using the bulk micromachining technology based on double side release.

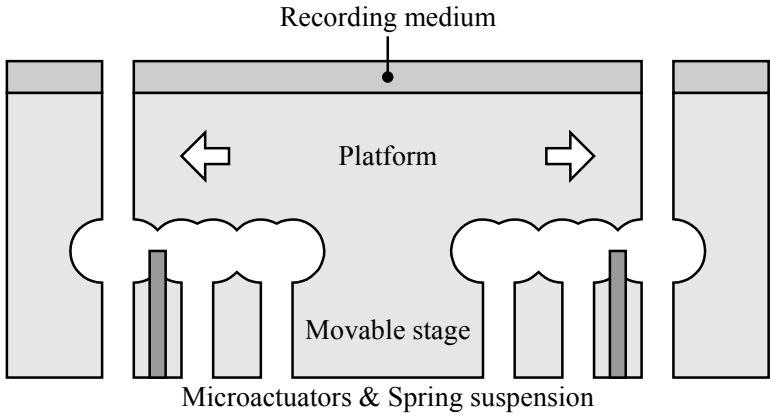

Figure 5.2: A schematic view of a two-level, electrostatic XY-scanner with driving actuators and a spring suspension completely placed beneath a movable platform to increase area efficiency.

The two-level XY-scanner utilizes both sides of the substrate to increase the effective recording area. A movable stage driven by microactuators is defined on one side of the substrate. This stage is mechanically connected to a platform machined on the opposite side. The platform, on which a recording medium is to

be applied, completely covers the area used for the microactuators and the spring suspension.

By hiding the driving components beneath a movable platform covered by the recording medium, a large area required for these components can be efficiently used for the data storage. This also allows further miniaturization, and thereby an increase in speed, of the medium scanners without compromise of the recording area efficiency. In this way, a large number of fast medium scanners with a large recording area, required in microSPAM (see Chapter 1), can be fabricated. Furthermore, the microactuators in a two-level XY-scanner are placed on the opposite side of the recording medium, preventing a potentially harmful influence of the microactuators on the operation of micromechanical probes used for the recording and vice versa.

A potential problem with the two-level XY-scanner is that the force generated by microactuators is not applied through the center of mass. This introduces an undesired torque that has to be taken into consideration in a design. The large height of microstructures achievable by the double-side release bulk micromachining technology, however allows for a large stiffness in the vertical direction, making this problem less pronounced.

5.4 FABRICATION AND RESULTS

In order to demonstrate the feasibility of the proposed technology, we have fabricated different prototypes of the two-level XY-scanner. Our primary intention was to prove the technological concept and we have not optimised our design in any respect. We have simply reused the design described in Chapter 4.

The fabrication process begins on a single side polished, silicon substrate with a thickness of 475 μm. In the selected substrate, isolating trenches, 2 μm wide and 32 μm deep, are etched and subsequently refilled with a 1.2 μm thick low stress silicon nitride layer deposited by LPCVD. The silicon nitride layer from the top surface is removed by a standard RIE using CHF_3 plasma chemistry. After removal of the silicon nitride, a silicon oxide layer with a thickness of 1 μm is deposited by PECVD on the backside. The photolithographic patterning is then performed on both sides of the substrate using standard Olin 917 photoresist. The photoresist pattern on the backside is transferred into the silicon oxide by BHF

etching. Next, the BSM multi-step one-run process [5] is employed to machine released microstructures on the front side of the substrate. The BSM process is performed using the optimised parameter settings summarized in Table 3.1. The final height of the released structures is 28 μm and the gap between freestanding structures and the bulk of the substrate is 8 μm. A SEM micrograph taken from the backside of released microstructures with properly integrated vertical trench isolation is shown in Fig. 5.3.

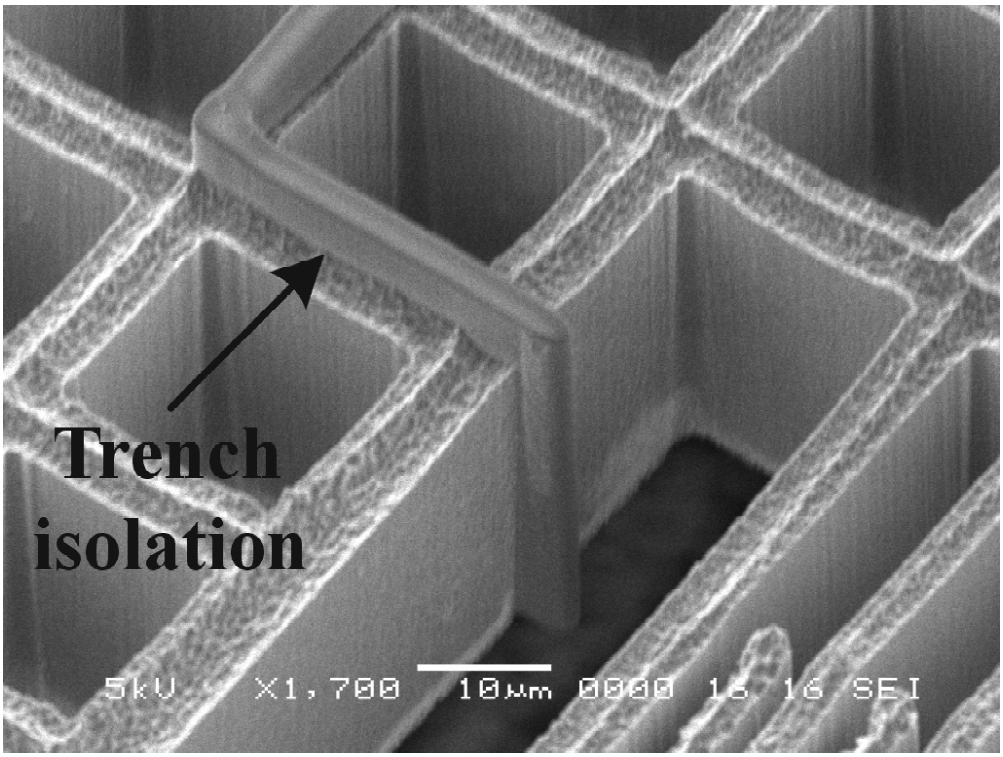

Figure 5.3: SEM micrograph of the backside of a microstructure with a properly integrated isolating trench assuring electrical insulation even on movable parts.

After the plasma release, a silicon layer, approximately 440 μm thick and located beneath the released microstructures, is completely etched through using DRIE processing. The microstructures, previously machined on the front side, were protected with a FC layer deposited prior the backside etching. The same processing parameters (see Table 3.1) as one used for the sidewall passivation in the plasma release process are employed. An SEM picture of the part of a two-

level XY-scanner, successfully manufactured in this fabrication process, is shown in Fig. 5.4.

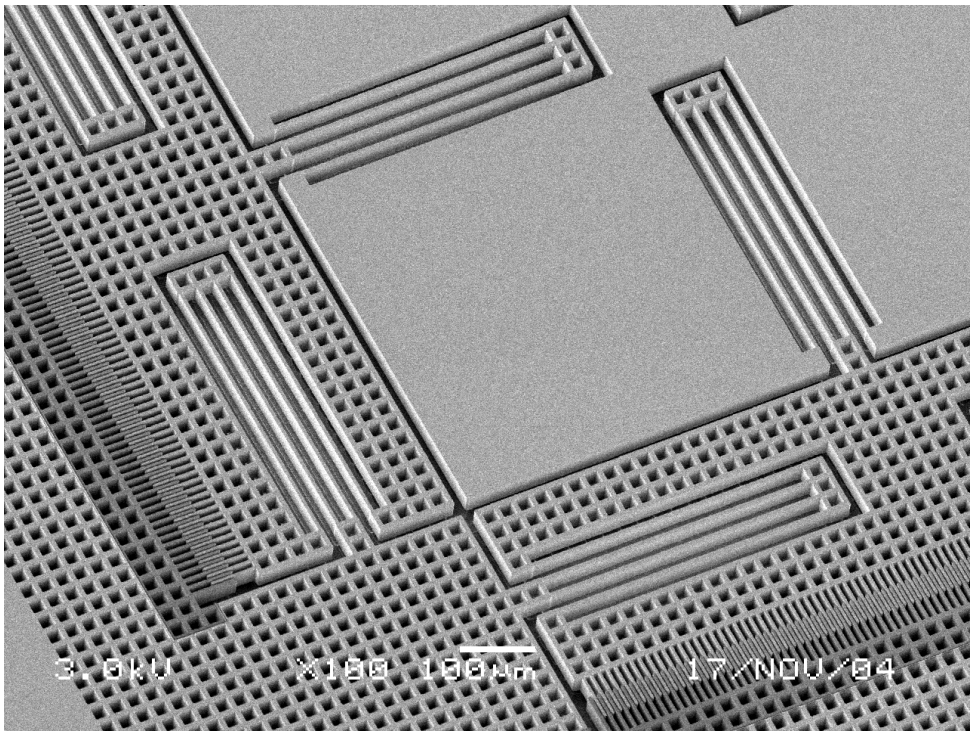

Figure 5.4: SEM micrograph of the part of a two-level XY-scanner fabricated using the bulk micromachining technology based on double side release.

Slender and mesh-like structures are fully undercut by the isotropic plasma etch. A visible contrast difference, originating from charging during the SEM session, signifies different electrical regions enclosed by the isolating trenches. A large non-perforated structure, suspended by folded flexures, is mechanically linked with a released platform on the opposite side of the substrate.

A two level XY scanner with all components is shown in Fig. 5.5. The whole scanner fits in an area of 2412 μm x 2412 μm. The scanner consists of a movable stage driven by two pairs of electrostatic comb-drive microactuators. Four intermediate stages and a folded flexure suspension are employed to provide decoupled motion of the central stage along two orthogonal axes. The movable stage and the intermediate stages are suspended by folded flexures, which are 410 μm long and 4 μm wide.

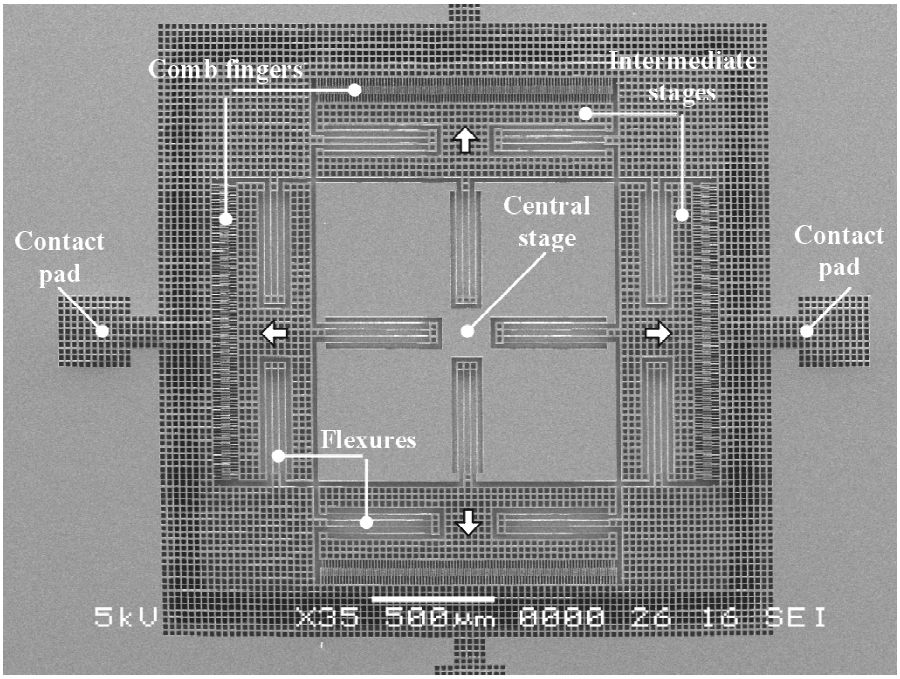

Figure 5.5: SEM micrograph showing an overview of a two-level XY-scanner driven by electrostatic comb-drive microactuators. The central stage is mechanically connected with a platform placed beneath.

The central stage is mechanically coupled to a 2106 µm x 2106 µm platform machined on the opposite side of the substrate. The non-perforated rectangular platform, which occupies 76 % of the total scanner area, is shown in Fig. 5.6.

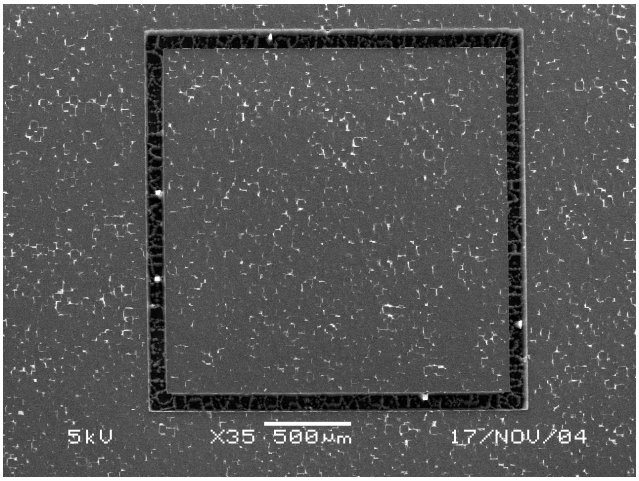

Figure 5.6: SEM micrograph of a released rectangular platform. All driving components of the XY-scanner are hidden beneath.

Each comb-drive actuator, partially shown in Fig. 5.7, consists of 194 fingers, which are 66 μm long and 3 μm wide. The gap and the overlap between comb fingers are 3 μm and 34 μm, respectively. The stationary part of a comb-drive actuator is mechanically anchored and electrically insulated from the bulk material by an isolating trench.

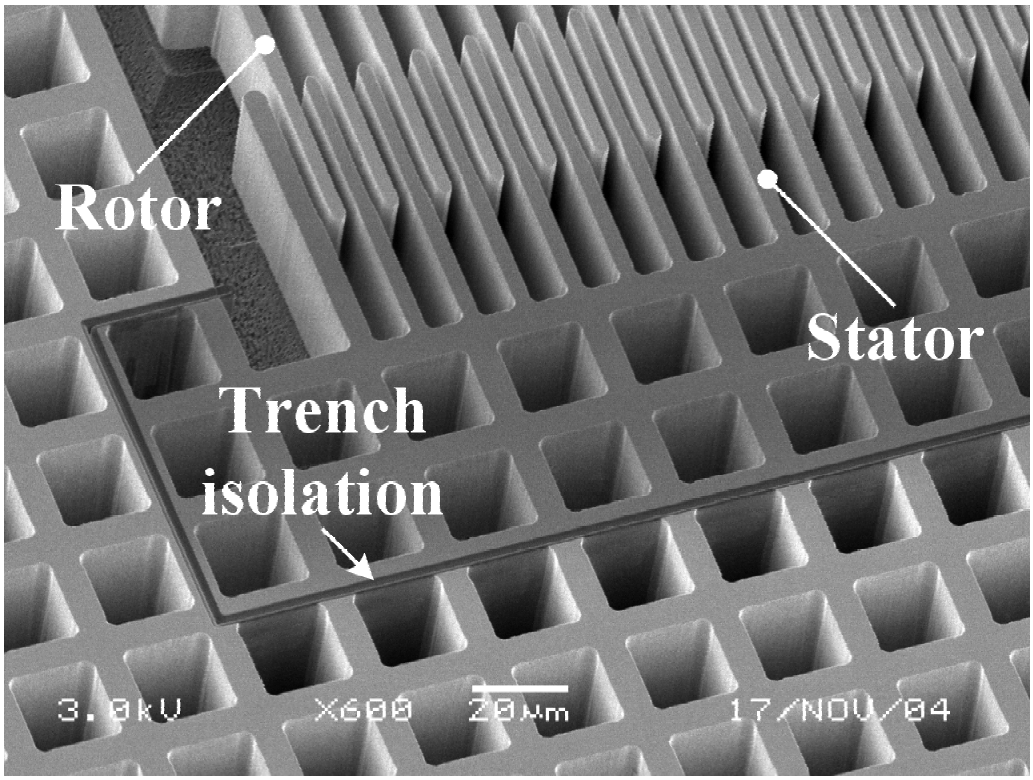

Figure 5.7: A SEM micrograph of an electrostatic comb drive with integrated trench isolation. The contrast is due to charging and indicates proper electrical insulation.

The two-level XY-scanner was successfully operated. The maximum displacement of ± 10 μm in two orthogonal directions was observed.

The fabrication process of this scanner was started on a relatively thick silicon wafer (475 μm), resulting in a large, massive platform (see Fig. 5.8) that limits the maximum speed of the scanner.

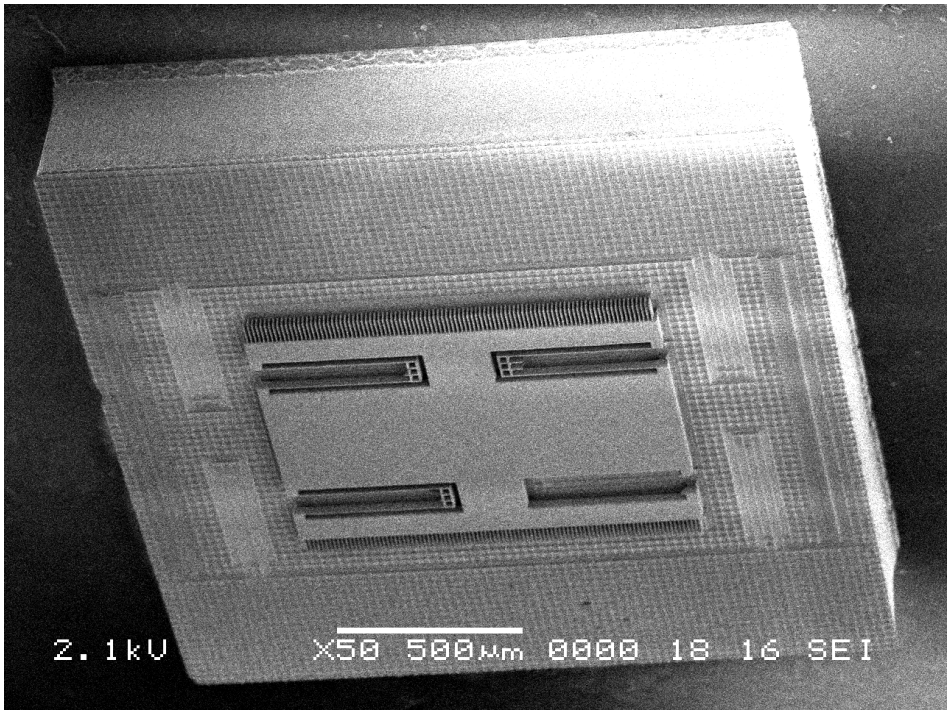

Figure 5.8: SEM micrographs of a movable platform.

To make faster scanners, one should reduce the thickness of the platform by starting the processing on a thinner substrate or by including an extra thinning step in the fabrication process. On the other hand, other MEMS application, such as inertial sensors will benefit from a large suspended mass.

5.5 CONCLUSIONS

A bulk micromachining technology for MEMS fabrication based on standard single crystal silicon substrate and vertical trench isolation is presented. This technology allows fabrication of monocrystalline silicon microstructures on both sides of the substrate. These microstructures, which are built in two levels, can be properly electrically insulated and, at the same time, mechanically connected. A two-level manufacturing process in the silicon bulk opens new design opportunities to realize MEMS with increased performance and functionality. The presented technology is successfully employed for fabrication of electrostatic XY-scanners for probe-based data storage with a significant large effective recording area proving the feasibility and large potential of this technology.

5.6 REFERENCES

1 Carley L R et al 2000 Single-chip computers with microelectromechanical systems-based magnetic memory *J. of Applied Physics* **87** 6680-6685

2 Carley L R, Ganger G R and D F Nagle 2000 MEMS-based integrated-circuit mass-storage systems *Communications of the ACM* **43** (11) 73-80

3 Kim C H, Jeong H M, Jeon J U and Kim Y K 2003 Silicon micro XY-stage with a large area shuttle and no etching holes for SPM-based data storage *J. Microelectormech. Syst.* **12**(4) 470-478

4 Alfaro J F and G K Fedder 2002 Actuation for probe-based mass data storage *Int. Conf. on Modeling and Simulation of Microsystems* **1** 202-205

5 de Boer M J, Jansen H and Elwenspoek M 1995 A study of the fabricating of movable structures for MEMS *Int. Conf. on Solid State Sensors and Actuators* (TRANSDUCERS 95) (Stockholm, Sweden) 565-568

Chapter 6

Selective trench refill method for single-mask MEMS fabrication

Abstract

In this chapter, we introduce a refill method based on conformal deposition and isotropic removal that allows selective refill of isolating trenches with a combination of a dielectric and a poorly conducting material. The selective refill method replaces two previously required patterning steps for trench isolation and structural layout with one, enabling single-mask fabrication of high-aspect-ratio monocrystalline MEMS with integrated vertical trench isolation both on standard silicon and SOI substrates.

6.1 INTRODUCTION

All microfabrication techniques presented in the previous chapters (Chapter 2-5) employ vertical trench isolation to achieve electrical insulation between mechanically connected microstructures in a single layer. Vertical trench isolation is realized by conformal deposition of a dielectric layer to completely fill isolating trenches followed by a directional etch to remove redundant dielectric material from the top wafer surface. The trench refill process is completed prior to the definition of a structural layout. Accordingly, at least two distinct patterning steps, one to define trench isolation and a second to pattern the structural layout, are used to fabricate microstructures with integrated vertical trench isolation. The fabrication process requires a minimum of two photolithography masks, which must be properly aligned. Possible mask misalignments must be taken into account in the design stage. Furthermore, the trench profile has to be carefully controlled to assure proper electrical insulation (see Section 2.3.2).

In this chapter, we present a novel trench refill process, based on conformal deposition and isotropic removal, which allows selective refill of trenches with a combination of a dielectric and a poor conducting material. Narrow trenches, with a width below a certain maximum, are completely refilled in this process, while the refill material from wider trenches is completely removed. This selective trench refill method is not only an alternative for the commonly employed method based on conformal deposition and directional removal, but it offers a unique possibility to replace two separate patterning steps, for trench isolation and structural layout, with one, allowing single-mask fabrication of MEMS with integrated vertical trench isolation.

In the following sections, we present the basic fabrication steps of the selective trench refill method and define some important design and processing rules. Subsequently, we prove the feasibility of the method by fabricating, in a single-mask process, microstructures with integrated vertical trench isolation, using both an SOI-compatible surface micromachining process and a bulk micromachining process on standard silicon substrates.

6.2 SELECTIVE TRENCH REFILL METHOD

We introduce the selective trench refill method by considering the fabrication steps to refill two trenches of different widths formed in a silicon substrate (Fig. 6.1). The wider (structural) trench represents the layout of an arbitrary microdevice, while the narrow (isolating) trench represents a vertical trench isolation that provides both electrical insulation and mechanical coupling between distinct parts of a microdevice.

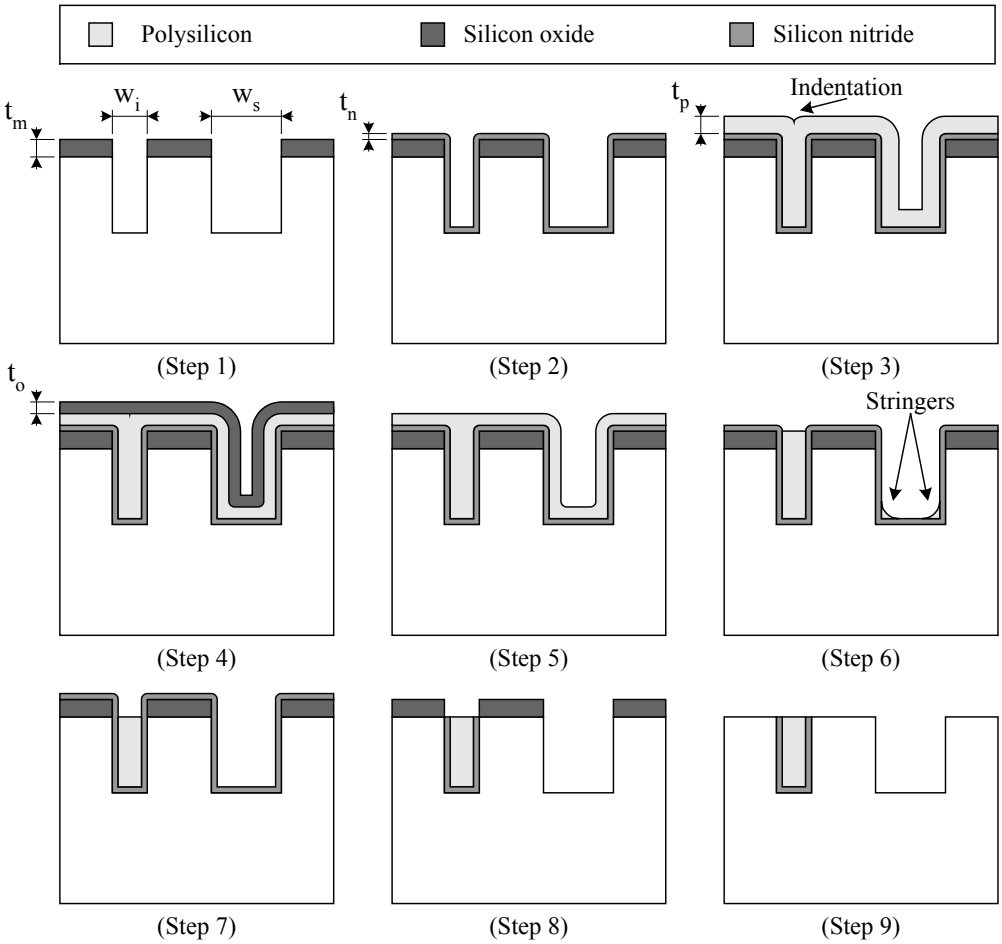

Figure 6.1: Basic fabrication steps of the selective trench refill method based on conformal deposition and isotropic removal.

We start the single-mask fabrication process by patterning the narrow isolating trench w_i and the wide structural trench w_s (*Step 1*). The trenches are etched through a stack, which consist of a silicon oxide layer with thickness t_m deposited

on a silicon substrate. A vertical trench profile is achieved using directional plasma etching of silicon oxide followed by deep reactive ion etching of silicon. The silicon oxide layer serves as an etching mask in the DRIE process, allowing deep trench etching due to the high etch selectivity to silicon. More importantly, the silicon oxide layer temporarily increases the depth of trenches, preventing removal of refill material from the silicon part of trench in subsequent isotropic etching steps (*Step 6* and *Step 7*)

On the patterned surface, we deposit a silicon nitride layer by LPCVD (*Step 2*). An isolating trench does not need to be completely filled by silicon nitride to provide an effective electrical insulation [1]; the silicon nitride layer may simply line the isolating trench. The required thickness of the silicon nitride layer t_n strongly depends on the intended application. In general, a very thin layer is sufficient to assure proper electrical insulation due to the large electrical resistivity and breakdown strength of LPCVD silicon nitride [2].

In the next fabrication step, we deposit an undoped LPCVD polysilicon layer, which completely closes the isolating trench, while leaving the structural trench open (*Step 3*). The thickness of the polysilicon layer t_p, required for appropriate filling, depends on the width of the trenches and the thickness of the previously deposited silicon nitride layer. The total thickness of the silicon nitride and polysilicon layers must be larger than the half-width of the isolating trench, but smaller than the half width of the structural trench:

$$\frac{1}{2}w_s > \left(t_n + t_p\right) > \frac{1}{2}w_i \qquad (6.1)$$

Fig. 6.2 shows isolating and structural trenches, sequentially filled with a silicon nitride and polysilicon layers. A commonly encountered problem during the refill step is that most isolating trenches are incompletely filled, leaving a void (keyhole) in the trench, as in Fig. 6.2 (left).

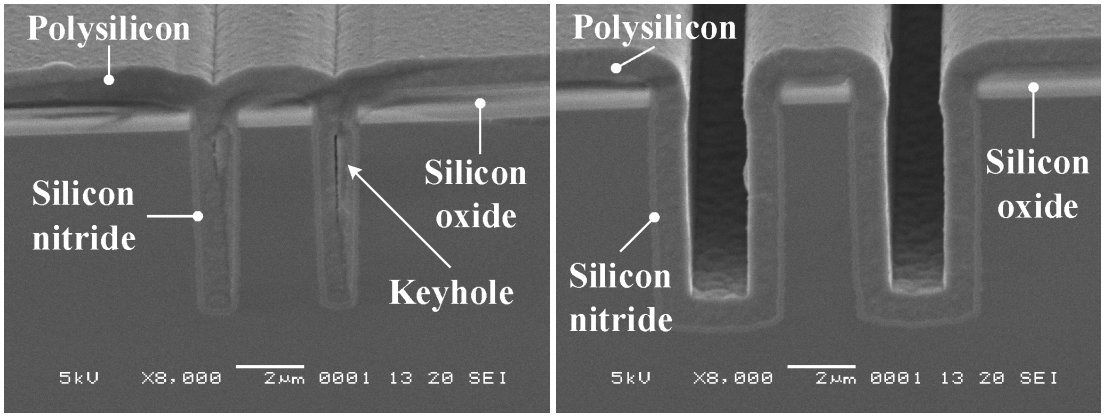

Figure 6.2: SEM micrographs of isolating trenches (left) completely filled with silicon nitride and polysilicon and structural trenches (right) that remain open.

This is highly undesirable because a void reduces the mechanical strength of an isolating trench. Furthermore, the etch solution employed in a subsequent isotropic removal of polysilicon (*Step 6* and *Step 7*) can possibly reach a void, hollowing out the refill material from the trench and causing a failure of the refill process [3]. To assure a voidless trench refill, it is preferable to have isolating trenches with a perfectly vertical or positive (tapered) etch profile and smooth walls.

Another artifact of trench filling is an indentation that is created in the polysilicon surface, as shown in Fig. 6.3 (left). The indentation, nearly unavoidable in the trench filling, is always centered over the isolating trench. It can be as deep as 0.6 μm, depending on the width of the isolating trench and the total thickness of the refill material. During the removal of polysilicon from the top surface by both directional and isotropic etching, the indentation is transferred into the isolating trench, reducing unintentionally its mechanical strength. This problem is particularly pronounced for shallow isolating trenches, where the indentation can comprise a considerable fraction of trench depth.

We employ thermal oxidation to partially remove indentations from the polysilicon surface (*Step 4*). A polysilicon surface before and after this planarization step is shown in Fig. 6.3.

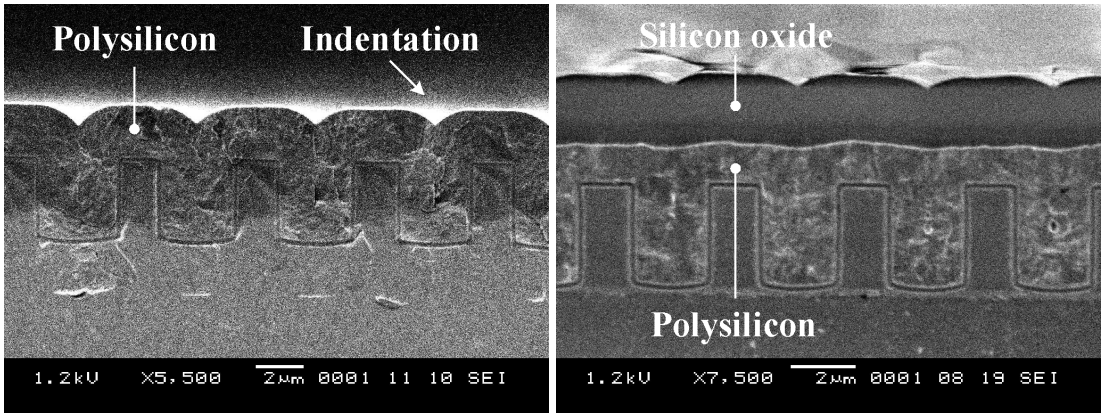

Figure 6.3: SEM micrograph of isolating trenches refilled with polysilicon before (left) and after (right) oxidation planarization.

The thermal oxide growth, shown in Fig. 6.4, changes the relative position of the sidewalls of structural trenches. In order to grow an oxide of thickness t_o a layer of approximately $0.5t_o$ of polysilicon is consumed [4], moving the sidewalls a distance of $0.5t_o$ closer. An excessive growth of silicon oxide can seal a structural trench, as shown in Fig. 6.4 (right), causing a failure of the refill process.

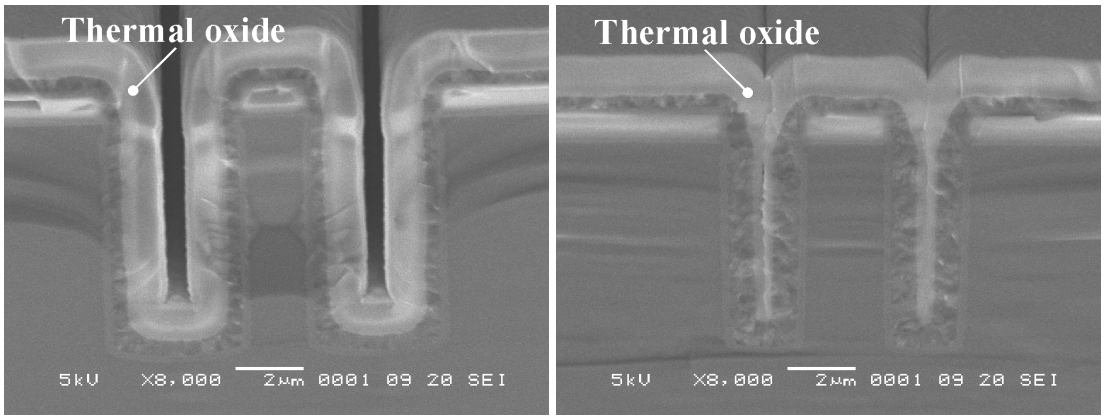

Figure 6.4: SEM micrograph of structural trenches after a thermal oxidation: remain open (left) and sealed (right).

In general, longer thermal oxidation produces a thicker silicon oxide layer, resulting in a smoother surface. The maximum allowable thickness of the thermally grown silicon oxide layer depends on the total thickness of the deposited

silicon nitride and polysilicon layers and the minimum width of a structural trench. In order to prevent sealing, the half width of smallest structural trench must be larger than the aggregate thickness of silicon nitride, polysilicon and thermal oxide layers,

$$\frac{1}{2}w_s > \left(t_n + t_p + 0.5t_o\right) \qquad (6.2)$$

Next, thermally grown silicon oxide is removed in hydrofluoric acid (HF) or a buffered HF (BHF) (*Step 5*). The underlying polysilicon layer is preserved due to the high etch selectivity to silicon oxide etching in (B)HF solution [5].

In the subsequent fabrication step, redundant polysilicon is removed from both the planar surfaces and from the sidewalls of structural trenches by wet isotropic etching (*Step 6*). Polysilicon in the insulating trench is preserved in this fabrication step, due to the limited access of the etching fluid, as shown in Fig. 6.5.

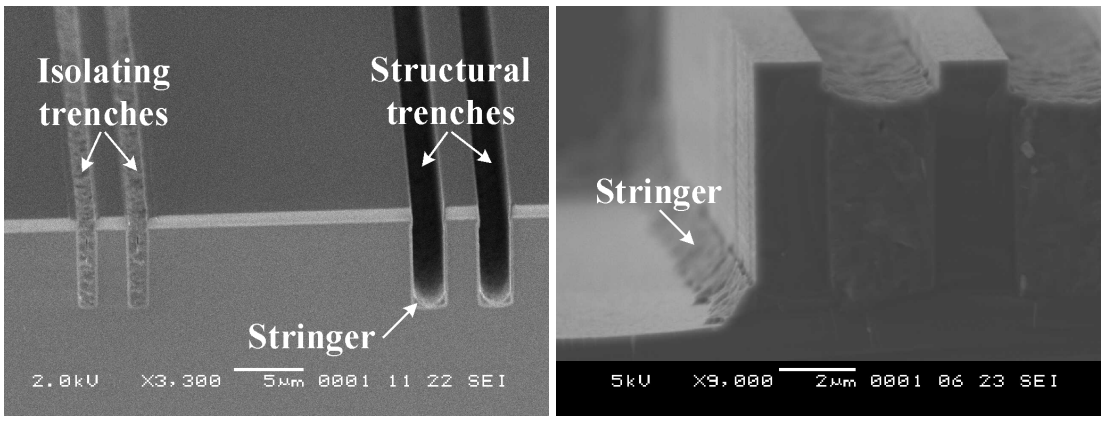

Figure 6.5: (left) SEM micrograph of isolating and structural trenches after isotropic removal of polysilicon. Polysilicon in isolating trenches is preserved, while the refill material from wider trenches is removed. (right) Removal of polysilicon from concave corners of structural trenches requires a considerable overetch, which simultaneously removes material from isolating trenches.

Directional plasma etching, commonly employed for removal of the redundant refill material [1, Chapter 2-5], will leave polysilicon on the sidewalls of structural

trenches, significantly changing the mechanical properties of the microstructures. Another significant advantage of wet isotropic etching, compared to removal by directional plasma etching, is a possibility of parallel processing of large number of wafers at the same time, allowing high throughput [3].

We use TMAH as the etchant for polysilicon. The etching proceeds in an isotropic manner due to random crystal orientation of polysilicon. Additionally, TMAH has a high etching selectivity for polysilicon compared to underlying silicon oxide and silicon nitride. The isotropic etch first clears remaining polysilicon from all planar surfaces, leaving a portion of the film material in the concave corners of structural trenches (stringers), as shown in Fig. 6.5 (right). A complete removal of the material from the concave corners requires a considerably longer etch time compared to that necessary for removal of material from all other surfaces (~100 % overetch). The refill material in the top part of the trench created in the silicon oxide layer is sacrificed during the overetch. In this way, the refill material in the silicon trench, that would otherwise be removed as illustrated in Fig. 6.5 (right), is successfully protected. As a rule of thumb, the thickness of silicon oxide should be equal to the thickness of the deposited polysilicon layer (t_m=t_p) to allow complete removal of stringers without affecting material in the silicon trench.

After polysilicon etching, wet isotropic etching of silicon nitride in hot phosphoric acid (H_3PO_4) is performed (*Step 8*). Phosphoric acid has a large selectivity for silicon nitride compared to silicon oxide and polysilicon [5]. Again, a considerable overetch is required to remove remaining silicon nitride from the concave corners of structural trenches.

In the last processing steps, the silicon oxide mask is stripped by wet etching in B(HF) solution (*Step 8*). The refill material in the isolating trenches is not affected in this etching step.

6.3 APPLICATIONS

The fabrication process presented above completely fills the isolating trench with a combination of dielectric and poorly conducting materials, and removes the refill material from the structural trench and the remaining surfaces. This allows single-

mask fabrication of MEMS with integrated vertical trench isolation by using both surface and bulk micromachining.

The single-mask surface micromachining process, illustrated in Fig. 6.6, starts on a substrate with a (poly)silicon device layer on top of the sacrificial silicon oxide layer. Alternatively, use of an SOI wafer would allow high-aspect-ratio monocrystalline silicon structures.

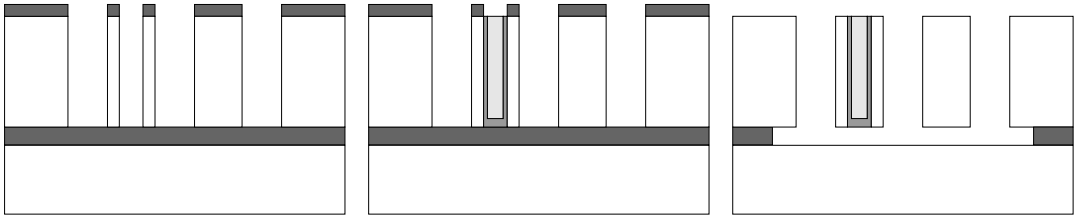

Figure 6.6: Single-mask surface micromachining based on the selective trench refill method: (a) patterning, (b) selective refill of isolating trenches and (c) sacrificial silicon oxide removal.

In the selected substrate, the structural layout and vertical trench isolation are patterned. After patterning, isolating trenches are selectively filled with a dielectric and a poorly conducting material using the selective trench refill method. The refill material from the structural layout is completely removed in this process. The refilled isolating trenches provide electrical insulation and lateral mechanical anchoring between distinct micromechanical structures. The microstructures with integrated vertical trench isolation are released by selective etching of the sacrificial silicon oxide layer with (B)HF.

The single-mask bulk micromachining process, illustrated in Fig. 6.7, employs a standard monocrystalline silicon wafer with an arbitrary crystallographic orientation. After patterning and selective refill, microstructures machined in the bulk silicon are undercut using an isotropic plasma release, introduced in Chapter 3. Polysilicon in the isolating trenches is protected during the plasma release by a thin silicon oxide layer, grown by an extra thermal oxidation step (not shown in Fig. 6.1). The thermal oxidation can be performed prior to removal of the silicon nitride layer in the selective trench refill process (*Step 8* in Fig. 6.1)

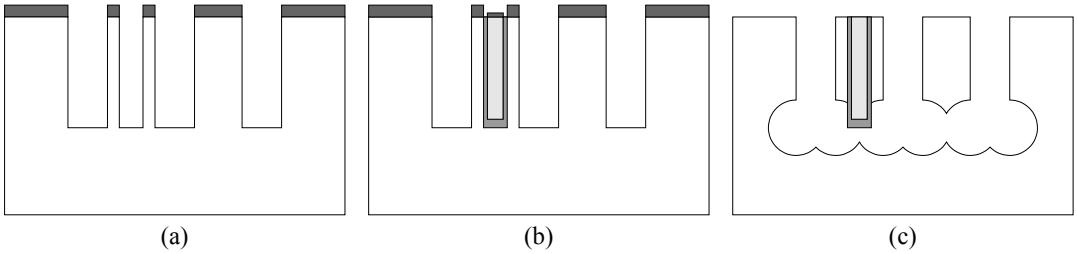

Figure 6.7: Single-mask bulk micromachining based on the selective trench refill method: (a) patterning, (b) selective refill of isolating trenches and (c) isotropic plasma release.

The single-mask surface and bulk micromachining processes have several advantages over a more conventional two-mask process, as presented in Chapters 2 and 3. First, only a single lithographic step is needed, eliminating the need for precise alignment. Furthermore, a positive trench profile, required for a voidless refill to assure large mechanical strength, does not cause accidental conduction as in the case of two-mask processes (see Section 2.3.2)

A serious disadvantage of the single mask process compared to conventional two-mask processes is that the minimum structural distance is directly related to the lateral dimension of isolating trenches. Furthermore, a single-mask process does not support interconnects, discussed in Section 2.3.3, for full integration of MEMS with on-chip electronics

6.4 FABRICATION AND RESULTS

In this section, we demonstrate the feasibility of the single-mask fabrication by discussing the manufacture of several released microstructures with integrated vertical trench isolation. The microstructures are fabricated using both surface and bulk micromachining.

The surface micromachining process is performed on a silicon substrate with a 5 μm polysilicon device layer on top of a 1 μm sacrificial silicon oxide. The bulk micromachining process is completed on a standard (100) silicon substrate.

The single-mask fabrication process starts with deposition of a 1 μm thick silicon oxide layer using LPCVD. Subsequently, we pattern isolating trenches, 1.5 μm wide, and a structural layout with the minimum structural distance of 3 μm.

The patterned trenches are filled sequentially with a 200 μm silicon nitride layer and a 1 μm polysilicon layer both deposited by LPCVD. After deposition, we perform wet oxidation of polysilicon at 1150 ^{o}C for 15 min to smoothen the surface. The thermally grown silicon oxide layer, 400 nm thick, is removed in HF 50%. Next, we etch remaining polysilicon in 25 % TMAH solution at temperature of 40 ^{o}C. Polysilicon from the top surface is removed in 20 minutes. We etch 20 minutes longer (overetching of 100%) in an effort to remove remaining polysilicon from concave corners of structural trenches. Subsequently, silicon nitride is etched in 85% H_3PO_4 solution at 180 ^{o}C. The etch rate of silicon nitride in this solution was around 4 nm/min, requiring 100 minutes etching inclusive the 100% overetching.

Microstructures fabricated in the surface micromachining process are released in BHF solution. The released microstructures with integrated vertical trench isolation are shown in Fig. 6.8.

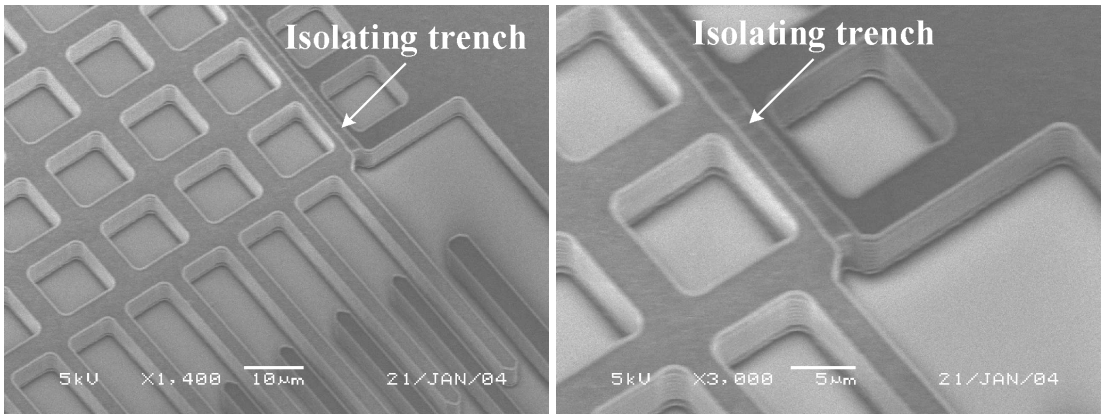

Figure 6.8: SEM micrographs of polysilicon microstructures with integrated vertical trench isolation, realized in a single mask surface micromachining process.

Microstructures machined in the bulk silicon are released by means of the advance plasma processing, using the process parameters presented in Chapter 3. The released high-aspect-ratio, single crystal silicon, microstructures with integrated trench isolation are shown in Fig. 6.9

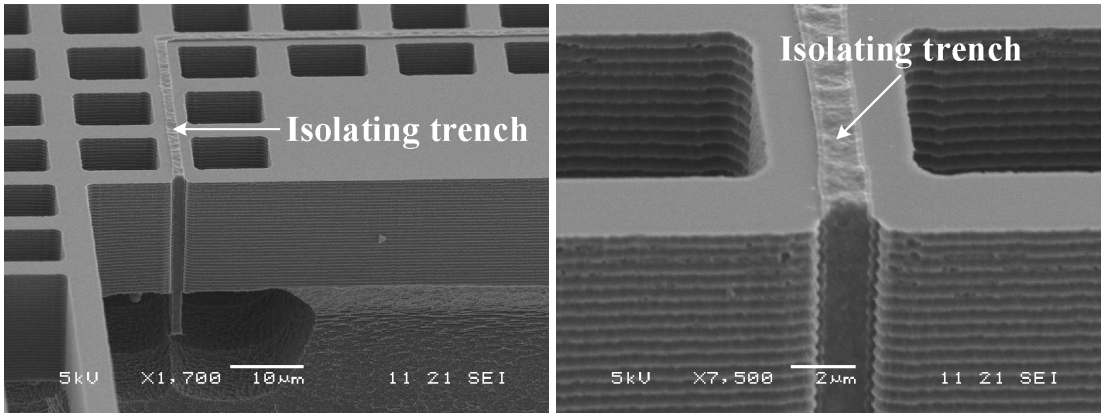

Figure 6.9: SEM micrographs of monocrystalline silicon microstructures with integrated vertical trench isolation, fabricated in a single-mask bulk micromachining process.

Example comb-drive microactuators, fabricated by the single mask refill method, are successfully operated.

6.5 CONCLUSIONS

We presented a refill method based on conformal deposition and isotropic removal that allows selective refill of isolating trenches with a combination of dielectric and poor conducting material. The selective refill method replaces two patterning steps, previously required, with the single one, enabling single-mask fabrication of high-aspect-ratio monocrystalline MEMS with integrated vertical trench isolation both on standard and SOI substrates. An advantage of the single mask process with respect to conventional two-mask processes is that only a single lithographic step is needed for the prototyping of MEMS devices. A disadvantage is that the minimum structural distance is directly related to the lateral dimension of isolating trenches. At the end, it is the specific application, which will decide if the designer will opt for the single or the double mask process.

6.6 REFERENCES

1 Brosnihan T J 1998 An SOI based, fully integrated fabrication process for high-aspect-ratio microelectromechanical systems *PhD Thesis* Department Of Mechanical Engineering, University of California, USA.

2 Stoffel A, Kovács A, Kronast W and Müller B 1996 LPCVD against PECVD for micromechanical applications *J. Micromech. Microeng*. **6** 1-13

3 Sax H, Kruwinus H and Waters E 1999 A Polysilicon overfill etch back using wet chemical spin-process technology *IEEE/SEMI Advanced Semiconductor Manufacturing Conference* (*ASMC*) 223-238

4 Sze S M 1988 VLSI technology McGraw-Hill, New York

5 Williams K R 1996 Etch rates for micromachining processing *J. Microelectromech. Syst*. **5**(4) 256-269

Chapter 7

3D Nanofabrication using Standard Micromachining Technology

Abstract

We report on a simple parallel processing method capable of producing addressable three-dimensional (3D) nanometer-sized structures, such as wires, wire frames and dots. The method employs isotropic removal of conformally deposited material onto a prepared template to form nanostructures in the concave corners of the template. The process results in well-defined nanometer scale structures with exact position and spatial arrangement fully determined by the template. An etching mask with nanometer size features and a nanowire pyramid on a freestanding cantilever, have been successfully fabricated, demonstrating the feasibility and potential of this technology.

7.1 INTRODUCTION

The selective trench refill method, introduced in the previous chapter, employs isotropic etching to remove a layer of material conformally deposited on a patterned surface. When the isotropic etch clears the deposited material from planar surfaces, a portion of the material remains in the concave corners, as shown in Fig.7.1. These etching artifacts, known in IC fabrication as stringers or veils, were previously considered highly undesirable.

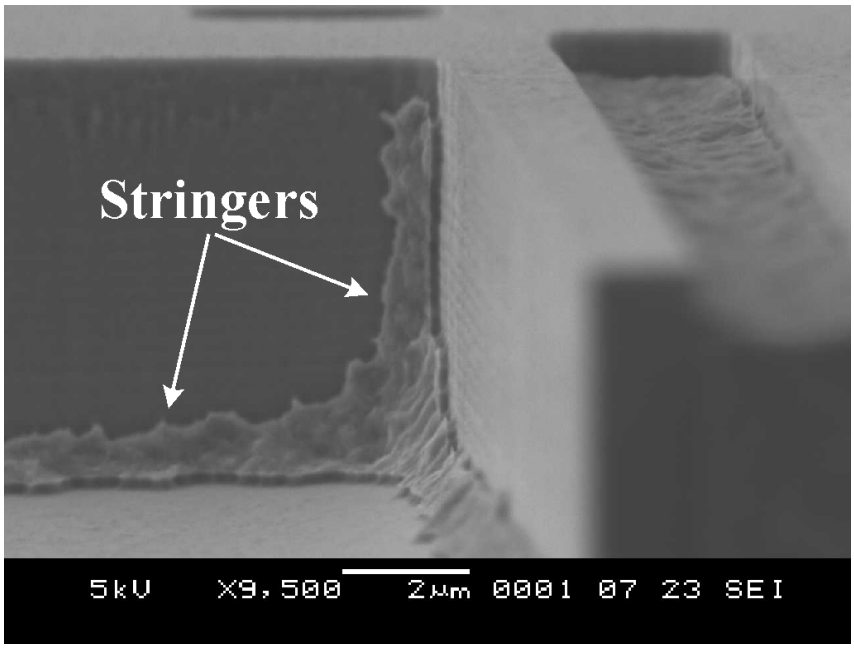

Figure 7.1: Isotropic etching of a conformally deposited layer remove material from all planar surfaces, leaving small portion in concave corners.

In this chapter, we exploit the abovementioned artifact to controllably form nanometer scale structures in three dimensions (3D) with well-defined position and spatial arrangement. In the following sections, we introduce the basic steps of the 3D nanofabrication method and prove its feasibility by fabricating an etching mask with nanometer size features and a 3D structure composed of nanowires.

7.2 3D NANOFABRICATION METHOD

Fig 7.2 illustrates the basic processing steps of the proposed 3D nanofabrication method.

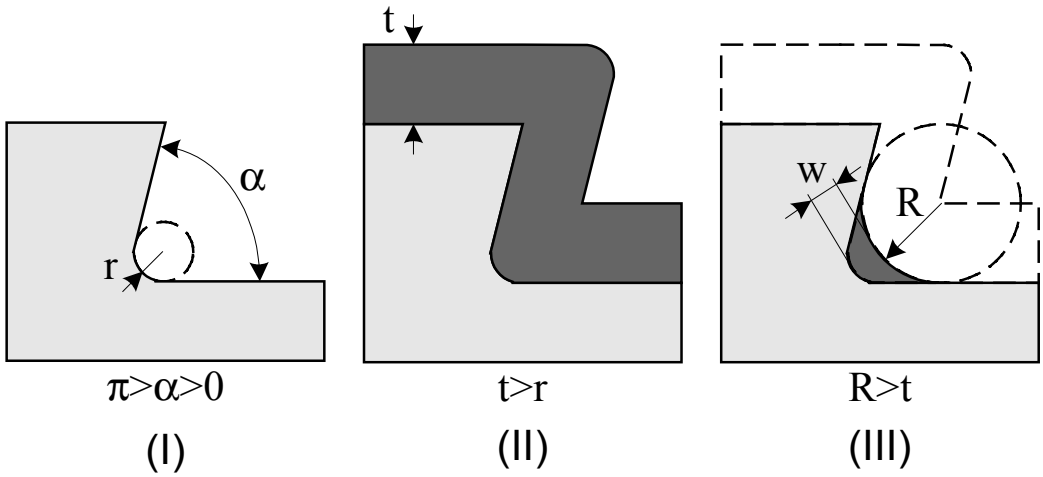

Figure 7.2: 3-D nanofabrication method: (I) template preparation, (II) conformal deposition and (III) time-controlled selective isotropic removal.

The fabrication process starts by creating a template with concave corners (*I*). A material layer is conformally deposited on the prepared template (*II*) and a selective isotropic etch of the deposited layer is performed. The access of the etchant to the material located in the concave corner is restricted by the corner geometry. Well-timed isotropic etching clears the deposited film from all template surfaces, except the material in the concave corner, resulting in well-defined structures with position and spatial arrangement fully determined by the template (*III*). To achieve good control over the resulting structures, the etching must be highly isotropic and selective to the underlying material.

The characteristic width w of the fabricated structures depends on the angle of the concave corner α, its radius of curvature r, the thickness t of the deposited layer and the isotropic etching distance R,

$$w = \frac{t - r}{\sin\left(\frac{\alpha}{2}\right)} + r - R \qquad (7.1)$$

To produce well-defined nanoscale structures, the deposited layer must be uniform, with a good step coverage. Small thickness and good uniformity can be achieved with LPCVD techniques. A thinner deposited layer is favourable,

because it allows the fabrication of smaller structures. Nevertheless, the thickness needs to be larger than the radius of curvature ($t>r$). Otherwise, the material from all surfaces, including the concave corners, would be removed simultaneously, resulting in failure of the fabrication process.

The radius of curvature r limits the minimum size of structures that can be formed in the concave corner. Therefore, a template with non-rounded concave corners ($r=0$) is preferred. Anisotropic etching of silicon in KOH, leads in a straightforward way to concave corners with r smaller than 1 nm. An interesting alternative is to etch silicon by Reactive Ion Etching (RIE) and follow with thermal oxidation, which sharpens the resulting concave features down to a radius r of a few tens of nm [1], with potential for reaching $r<1$ nm. The former method restricts the possible structures to the crystallographic properties of silicon, while the latter gives much more design freedom. Other etching and patterning techniques and template materials can be employed as well.

The etching distance R is determined by the duration and rate of isotropic removal. R needs to be marginally larger than the thickness t ($R>t$) to remove all the deposited material from planar surfaces. A low etching rate is preferred, because it allows a better control of the structure size.

Corner angle α affects the width of fabricated structures, since material remains longer in corners with smaller angles, resulting in wider structures, as shown in Fig. 7.3.

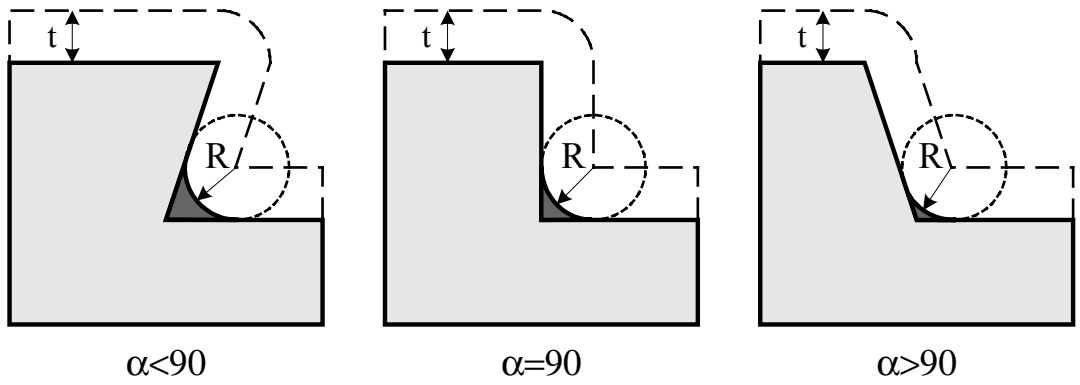

Figure 7.3: Dimensions of structures formed in the concave corners depends on the angle. Small corner angles result in wider structures.

7.3 EXPERIMENTS

In this section, we prove the feasibility and large potential of the 3D nanofabrication method by creating a silicon oxide etching mask with nanometer size features using conventional photolithography and by fabrication of a pyramid composed of silicon nitride nanowires on a freestanding cantilever beam.

7.3.1 Mask with nanometer features

The basic processing steps for fabrication of a silicon oxide mask with nanometer size features are shown in Fig. 7.4.

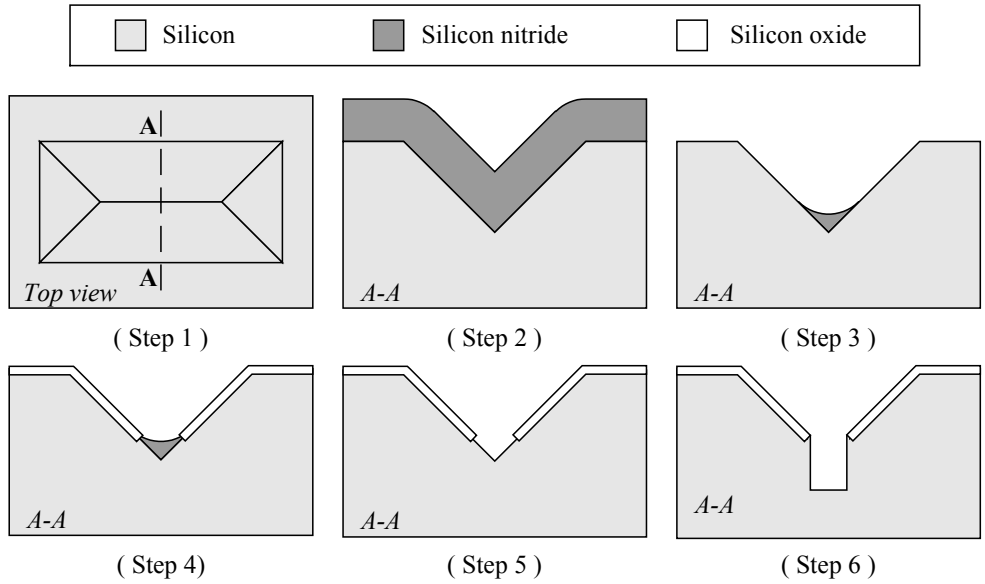

Figure 7.4: Basic processing steps for a silicon oxide etching mask with nanometer-sized features using conventional micormachining and standard lithography.

The fabrication process starts on a single crystal silicon substrate with <100> crystallographic orientation. In the selected substrate, we patterned a rectangular mold using anisotropic etching in 25 wt% KOH:H_2O at 75 ºC (*Step 1*). The mold is bounded by (111) crystallographic planes that exhibit a very low etch rate in KOH. At the intersection of these planes concave corners with very small radii of curvature are formed, typically less than 1 nm. On the patterned substrate, a low stress silicon nitride layer is conformally deposited by LPCVD, resulting in an uniform 80 nm thick layer along the substrate surface (*Step 2*). Next, silicon

nitride is etched isotropically in 50% HF at room temperature (*Step 3*). The etching proceeded until silicon nitride is removed from the top surface of the substrate, indicated by the hydrophilic-hydrophobic transition. Silicon nitride in the concave corners of the mold was preserved in this etching step, as discussed in the previous section. A relatively low etch rate of silicon nitride in HF 50% (3.5 nm/min) makes the end point detection of the etch process less critical, allowing good control of the final nanostructures size. Additionally, the underlying silicon is not affected in the etching process, due to its extremely slow etch rate in HF-based etchants [2]. In the next fabrication step, a 100 nm silicon oxide layer is thermally grown on the silicon (*Step 4*). Silicon in the concave corners of the mold is protected from the thermal oxidation by the silicon nitride nanostructures. Subsequently, remaining silicon nitride is selectively removed from the concave corners (*Step 5*). We used an 85% phosphoric acid (H_3PO_4) solution at 180 ^oC, which has a large etch selectivity for silicon nitride compared to silicon oxide and silicon [2]. Removal of the remaining silicon nitride results in a silicon oxide mask with nanometer size openings, located on the concave corners of the silicon mold.

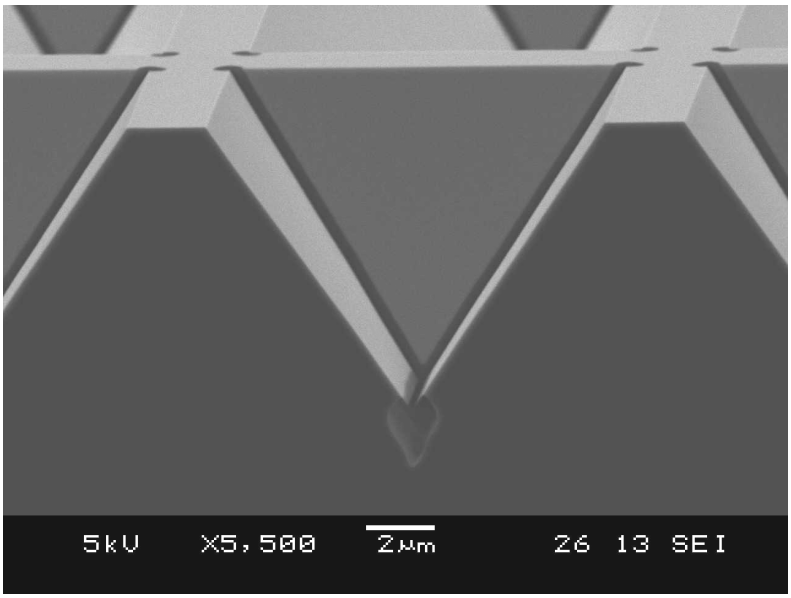

Figure 7.5: SEM micrograph of a plasma etched silicon template. Concave corners of the template were protected by silicon nitride nanostructures during the oxidation step. After the selective removal of the silicon nitride, openings in the silicon oxide are left, which served as an etching mask for the silicon.

Finally, the underlying silicon is etched through the openings in the silicon oxide mask using plasma etching (*Step 6*). Fig. 7.5 shows the cross section of a silicon mold after the plasma etching. As seen in Fig. 7.5, the openings in the silicon oxide mask are created at each concave corner regardless of its spatial position or orientation.

7.3.2 3D Nanopyramid

In the previous experiment we used the 3D nanofabrication method to create an etching mask with nanometer features. Here, we present a fabrication process for 3D structures composed of silicon nitride nanowires, which are attached on a freestanding cantilever, as illustrated in Fig. 7.6

.

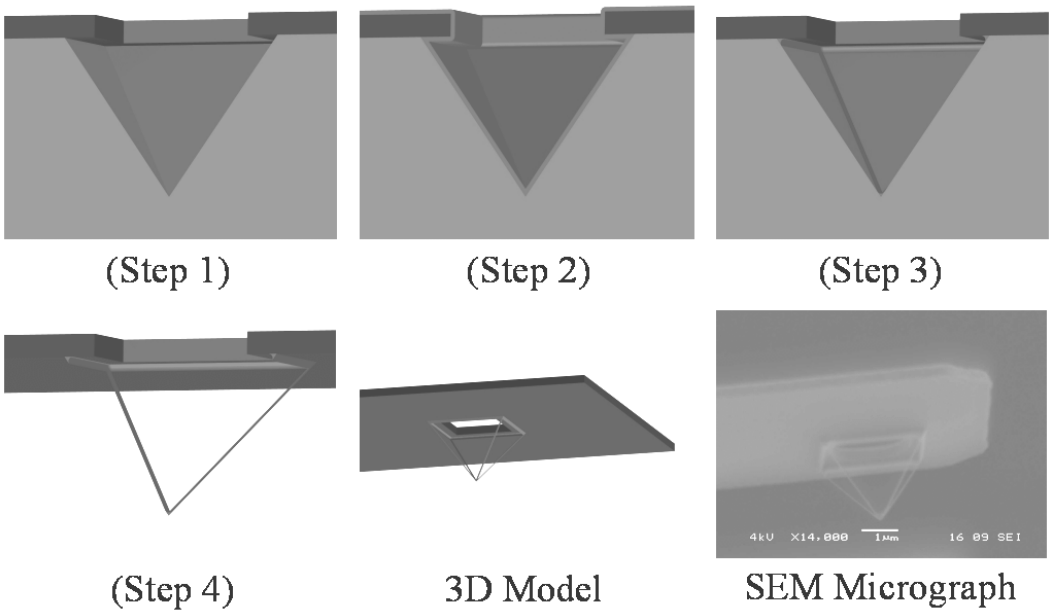

Figure 7.6: Processing steps for a 3D pyramid composed of silicon nitride nanowires, attached on a freestanding cantilever beam.

The fabrication process starts with a deposition of a 500 nm thick silicon nitride layer on the <100> silicon substrate by LPCVD. In the silicon nitride layer, we pattern a circular opening using directional plasma etching. Subsequently, we form a pyramidal cavity by anisotropic etching of single crystal silicon in KOH solution (*Step 1*). The etching proceeds until the (111) crystallographic planes are reached, resulting in the undercutting of the mask. The undercutting forms a

concave corner between the sidewalls of the cavity and the silicon nitride layer. Subsequently, we deposit a second lows stress silicon nitride layer with a thickness of 80 nm using LPCVD (*Step 2*). Using 50% HF, we then isotropically remove this layer from all surfaces with exception of the material in the corners of the pyramidal cavities and between the sidewalls of the cavity and the top silicon nitride layer (c). An unpatterned dummy silicon wafer with a silicon nitride layer of the same thickness is employed to determine the etching time. In the next fabrication step we pattern a cantilever in the first silicon nitride layer by directional plasma etching using a photoresist mask. The silicon nitride nanostructures, formed in the previous step, are protected by the photoresist during the plasma etching. Finally, the cantilever and attached silicon nitride nanowire pyramid are released by a front side etch of silicon in KOH solution (Step 4). A SEM micrograph of the pyramid is shown in Fig. 7.7.

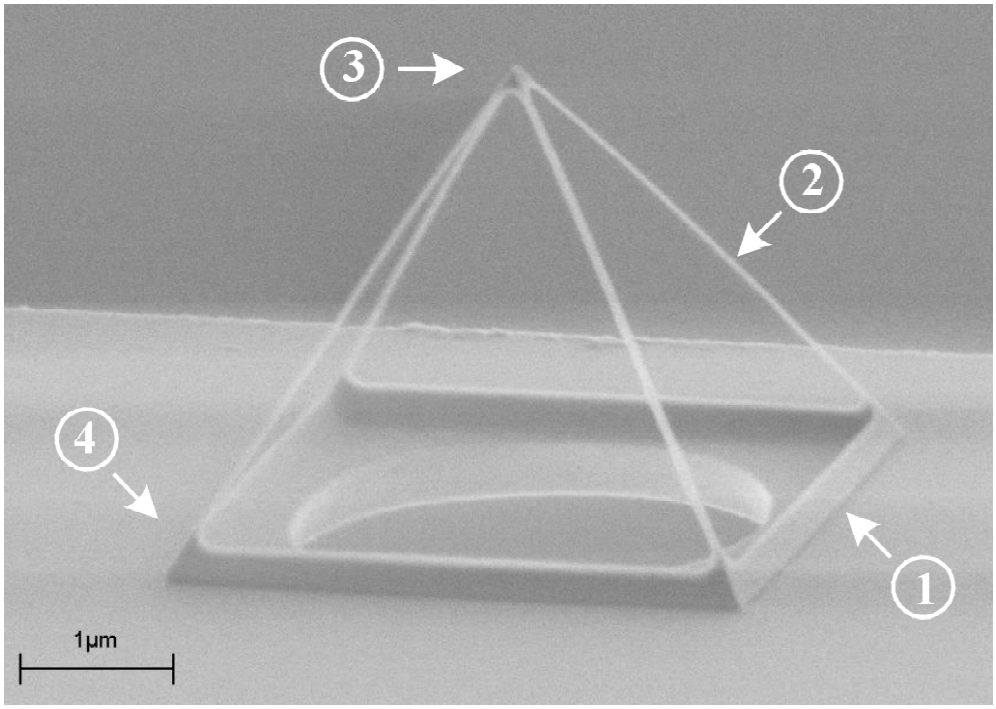

Figure 7.7: SEM micrograph of a freestanding pyramid, composed of 80 nm thick silicon nitride nanowires, integrated on a cantilever beam. Different geometry of concave angles determines the resulting thickness of the wires: 1. Two planes intersect at 57.4° angle; 2. Two planes intersect at 90° angle; 3. Four planes intersect; 4. Three planes intersect.

As expected from the theory the thickness of the nanostructures is determined by the geometry of the concave corners, with smaller angles resulting in thicker structures. Therefore, nanowires formed at the intersection of the sidewalls of pyramidal cavity and the silicon nitride layer (57.4º angle) are thicker than those formed at the intersection of two sidewalls (90º angle). At the intersection more than two planes, the structure is even thicker, as shown in Fig. 7.7 at the apex or base of the pyramid.

7.4 DISCUSSION AND CONCLUSIONS

We have presented a simple parallel processing method based on conventional photolithography that produces well-defined nanometer scale structures in three dimensions. The method is based on thin film deposition and selective isotropic removal of material from a prepared template.

The basic requirements of a successful process are: (1) a template with the concave corners with radii of curvature smaller than the film thickness, (2) conformal coverage of the template by thin film material, (3) isotropic removal of the thin film and (4) a selective etch process. In principle any combination of materials complying with the four basic requirements may be used in the proposed process. We expect that nanostructures can be fabricated from a variety of materials, including metals. Dimensions of the nanostructures in the range of a few nanometers are feasible (see Fig. 7.8) by controlling the geometry of the concave corners, the thickness of the deposited thin film and the duration and the rate of isotropic removal.

The 3D nanofabrication method can be employed in a variety of ways. The nanostructures, defined in this process, can be used as a mask to pattern the underlying substrate or layer, producing nanometer features with standard micrometer lithography (see Section 7.3.1) Additionally, complex 3D structures composed of nanowires can be fabricated and integrated with other functional components such as bond pads, cantilever beams, membranes and bridges, complex spring constructions, microactuators and sensors, etc. A pyramid composed of silicon nitride nanowires, suspended on a freestanding cantilever shown in Fig. 7.7, illustrated this potential.

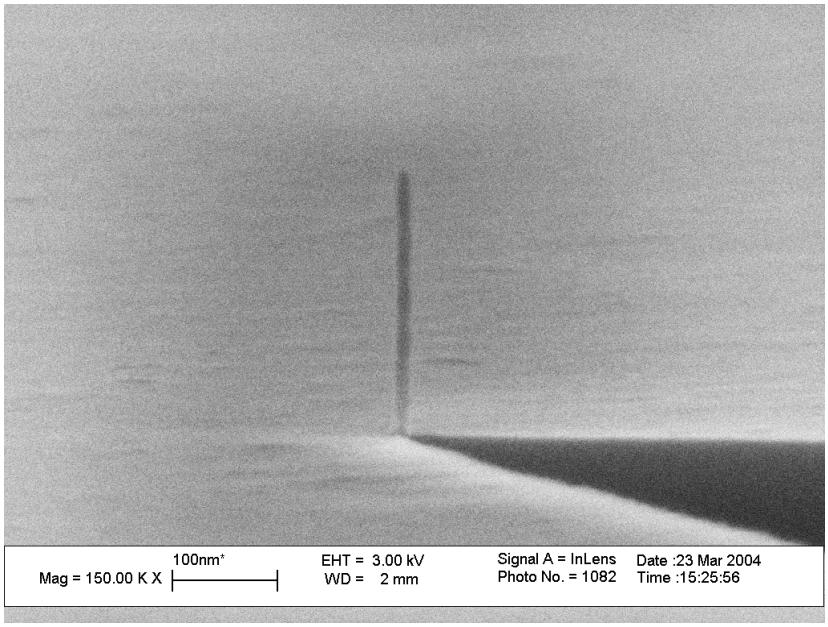

Figure 7.8: SEM micrograph of a protruding 17 nm thick silicon nitride structure.

The fabrication of dots is an extension of this process. Inverted tips, an example is the apex of the pyramid in Fig. 7.7, are formed when three or more planes of the template meet. The material in the inverted pyramid tip is thicker than the edges, and will resist etching longest, resulting in a nanodot. Furthermore, nanowires can be covered by a third material, and then selectively removed. In this way, complex nanotube systems can be fabricated and easily connected to micro-sized functional structures (reservoirs, flow sensors, pressure sensors, electrodes for EOF flow, etc.).

Advantages of this new top-down approach to the fabrication of 3-D structures include the simplicity of the process, compatibility with conventional micromachining, straightforward use of photolithography, the possibility to fabricate three-dimensional structures in a wide range of materials and addressability of these structures by other functional components.

7.5 REFERENCES

1 Marcus R B, Ravi T S and Gmitter T 1990 Formation of silicon tips with <1nm radius *Appl. Phys. Lett.* **56**(3) 236-238

2 Williams K R 1996 Etch rates for micromachining processing *J. Microelectromech. Syst.* **5**(4) 256-269

Chapter 8

High-performance electrostatic linear stepper micromotor

Abstract

In this chapter we report on an electrostatic linear micromotor, which employs built-in mechanical leverage to convert normal deflection of a flexible plate into a small in-plane step and two clamps to enable bidirectional stepping motion. The motor, measuring 412 µm x 286 µm, was fabricated by a combination of trench isolation technology and standard surface micromachining in a relatively simple process. The maximum achieved travel range was ± 70 µm, limited only by the suspension design. Depending on the plate actuation voltage, two operation modes were achieved with adjustable step sizes from 0.6 to 7 nm and 49 to 62 nm. The motor was driven up to a cycling frequency of 80 kHz. Output force of 1.7 mN was measured at 55 V for both the clamps and plate. The motor was operated for 5 days at a stepping frequency of 80 kHz and has travelled a cumulative distance of more than 1500 m in 34 billion steps without observable deterioration in performance.

8.1 INTRODUCTION

The micro Scanning Probe Array Memory (μSPAM), introduced in the first chapter, will combine high storage capacity with low power consumption and small size. The basic principle behind μSPAM is to use a large array of stationary micromechanical probes to scan a magnetic medium that moves in two dimensions. A successful implementation of the μSPAM concept requires a compact micropositioner with demanding performance characteristics, such as speed in mm/s range, displacement of hundreds of μm's, mN force, resolution on the order of tens of nm and low power consumption.

Shuffle motors [1,2] are potential candidates to perform this demanding positioning task. Shuffle motors employ built-in mechanical leverage to convert normal deflection of an elastic plate into a small powerful step and two electrostatic clamps to enable bidirectional stepping motion.

The first shuffle motor was fabricated by a surface micromachining process, using seven lithographic masks and three polysilicon device layers [1]. The motor, measuring 560 μm x 400 μm, was operated successfully with a maximum speed of 0.1 mm/s, corresponding to a cycling frequency of 1.16 kHz and an average step size of 85 nm. An output force of 0.043 mN was achieved at the plate and clamp voltages of 25 V and 40 V, respectively. The performance and reliability of the motor was limited due to charge accumulation in the insulating silicon nitride layer.

The negative effect of charge accumulation was eliminated in an improved shuffle motor design by only allowing mechanical contact between electrically grounded parts [2]. The motor, measuring 200 μm x 1500 μm, delivered a force of 0.45 mN at driving voltages of 65 V and 150 V for the plate and clamps, respectively. Velocities up to 3 mm/s are demonstrated, corresponding to a cycling frequency of 80 kHz and an average step size of 38 nm. A stroke of ± 70 μm is achieved. The motor was fabricated by the five-level SUMMiT V process (14 masks, 240 process steps), which is the most complex polysilicon surface micromachining technology reported to date [3].

In this paper we report on a shuffle motor fabricated using a combination of trench isolation technology and standard surface micromachining. This enables us

to simplify the fabrication process and improve the overall performance characteristics and reliability, as shown in Table 8.1. We believe this shuffle motor has the highest force and power density ever published for an electrostatic microactuator (see Appendix A).

Table 8.1: Performance characteristics of different type of shuffle motors.

Parameter	Tas et. al. [1]	de Boer et. al. [2]	Sarajlic et. al. This Chapter
Fabrication process	7 masks 3 poly layers	14 masks 5 poly layers	4 masks 2 poly layers
Dimensions [μm x μm]	560 x 400	1500 x 200	412 x 286
Force [mN]	0.04	0.45	1.72
Voltage clamp (plate) [V]	40 (25)	150 (65)	55 (55)
Travel range [μm]	43	200	140
Speed [mm/s]	0.1	3	3.6
Step size [nm]	86	38	45
Durability [No. of steps]	-	-	34 billion

In the following sections, we present the design of the shuffle motor and derive models to predict its performance characteristics. We demonstrate stepping motion of the motor and characterize its performance in terms of average step size, speed and output force.

8.2 SHUFFLE MOTOR

8.2.1 Design

Fig. 8.1 shows the design of the shuffle motor, consisting of two U-shaped clamps and an elastic plate. Stretching springs between clamps are employed to guide their relative motion. The plate and clamps are electrically insulated, allowing individual biasing of these components. The motor moves over an unpatterned substrate covered by an insulating layer. The substrate is electrically grounded during operation of the motor. Driving voltage signals to the clamps and plate are provided through the suspension of the motor, which is not shown in Fig. 8.1.

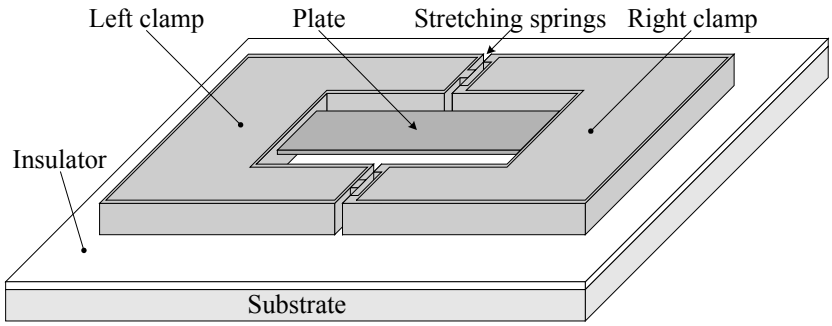

Figure 8.1: A schematic view of a shuffle motor.

The proposed design is substantially different from the previously reported shuffle motors [1, 2], where the whole motor is grounded and driving voltage signals are provided through underlying electrodes. The elimination of underlying electrodes in our design reduces the complexity of the fabrication process. Furthermore, it results in motion of the motor unrestricted to predefined paths, and allows a successful realization of a shuffle motor with two degrees of freedom, as presented in Chapter 9.

8.2.2 Working principle

Fig. 8.2 illustrates a walking motion of the shuffle motor, achieved by applying an appropriate voltage sequence to the plate and clamps.

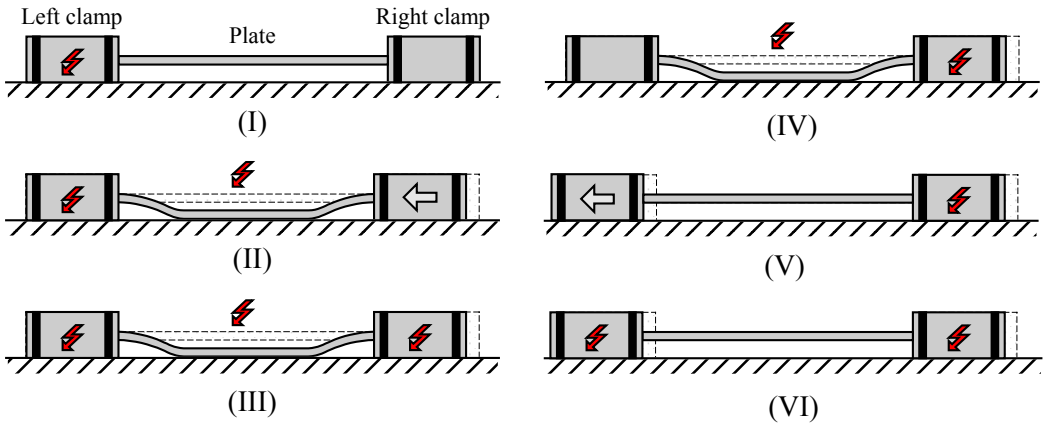

Figure 8.2: Walking sequence of a shuffle motor: (I) left clamp activated, (II) deflection of the plate causes powerful longitudinal contraction, (III) right clamp activated, (IV) left clamp released, (V) stretching of the plate moves left clamp, (VI) left clamp activated again.

First, a voltage is applied on the left clamp, inducing an electrostatic force that prevents sliding of the activated clamp (*I*). Next, a voltage difference is applied between the plate and the substrate, causing deflection of the plate. The normal deflection of the plate induces a contraction of the entire motor, moving the right clamp closer to the left (*II*). Since the normal deflection of the plate is much larger than the induced longitudinal motion there is a built-in mechanical leverage, resulting in a small but powerful contraction. Subsequently, the right clamp is activated in the new position (*III*) and the left clamp is then released (*IV*). The released plate stretches and pushes the left clamp outwards (*V*). The actuation sequence is completed by activation of the left clamp (*VI*). The whole motor is moved a single step to the left. By repeating the actuation sequence a large number of steps can successively be added, resulting in a large displacement range. Reversing the sequence enables bidirectional motion of the motor, without any additional complexity.

8.2.3 Stepping modes

A shuffle motor converts normal deflection of an electrostatically actuated plate into an in-plane step. The step size depends on the degree of the plate deflection, directly related to the voltage U_p applied to the plate. Non-contact and contact modes, resulting in fine and coarse stepping motion, can be attained by an appropriate choice of the actuation voltage, as illustrated in Fig. 8.3.

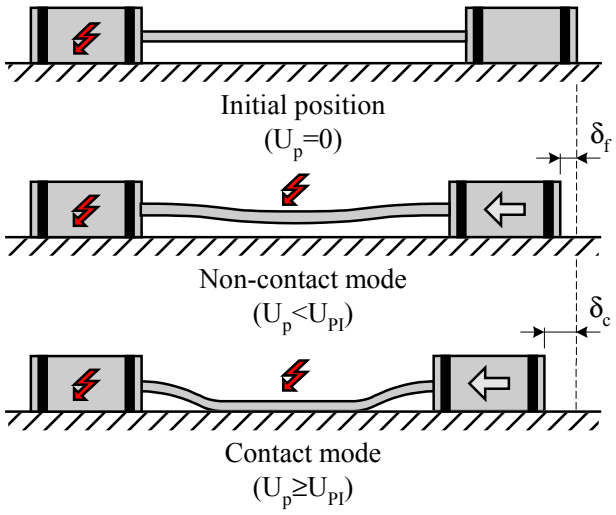

Figure 8.3: Different stepping modes of the shuffle motor.

In the non-contact mode, the plate is operated in the stable regime below the pull-in voltage U_{PI} ($U_p<U_{PI}$). In this operating mode, the mechanical restoring force of the plate counteracts the electrostatic force, resulting in a relatively small normal deflection of the plate and a fine longitudinal displacement δ_f. By increasing the actuation voltage above pull-in ($U_p \geq U_{PI}$), the electrostatic attraction force between the plate and substrate increases faster with decreasing gap than the restoring mechanical force of the plate, causing instability and ultimately, collapse of the plate onto the substrate. The large deformation of the plate, associated with this, results in a relatively large longitudinal displacement δ_c.

8.3 FABRICATION

A successful realization of the proposed shuffle motor requires proper electrical insulation and, at the same time, mechanical connection between the clamps and the plate. We combine vertical trench isolation with surface micromachining, already discussed in Chapter 2, to satisfy these requirements with minimum number of processing steps. A relatively simple fabrication process is developed, which employs only two polycrystalline silicon device layers and four photolithography masks. A detailed description of all processing steps is given in Section 9.3. Fig. 8.4 shows a fabricated shuffle motor with all components.

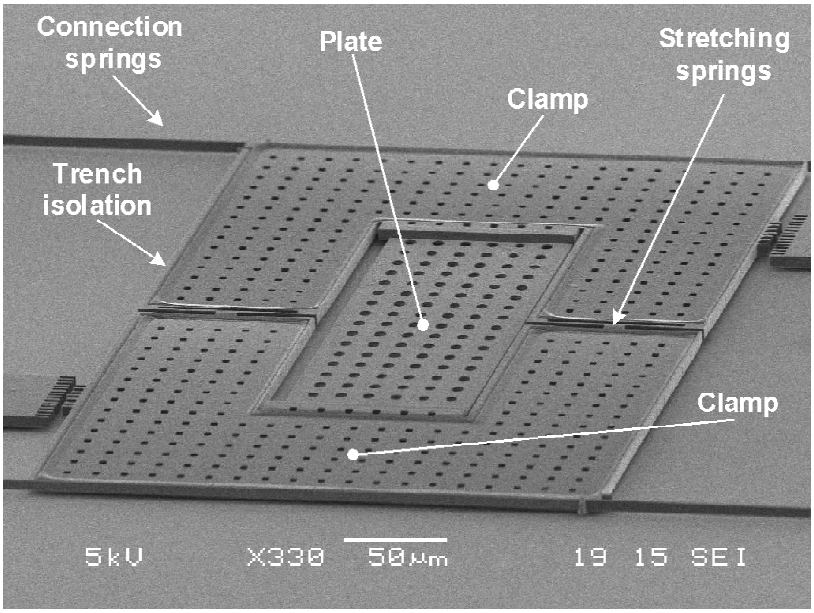

Figure 8.4: SEM micrograph of a shuffle motor.

The motor employs trenches refilled with silicon nitride to provide an electrical insulation between the clamps and plate. Isolating trenches, shown in Figure 8.5 (left), enable independent biasing of these components. At the same time, the stiffness and mechanical strength of isolating trenches ensure mechanical integrity of the motor. Silicon nitride isolating bumps are evenly spaced on the backsides of the clamps and plate, as shown in Fig. 8.5 (right). The isolating bumps significantly reduce the contact area, preventing stiction of the clamps and plate during fabrication and operation. During operation of the shuffle motor only isolating bumps make contact with the silicon nitride coating on the wafer surface, reducing contact charging and charge accumulation. Furthermore, due to the hardness of silicon nitride, its use on both sides of the contact reduces wear, increasing reliability of the motor.

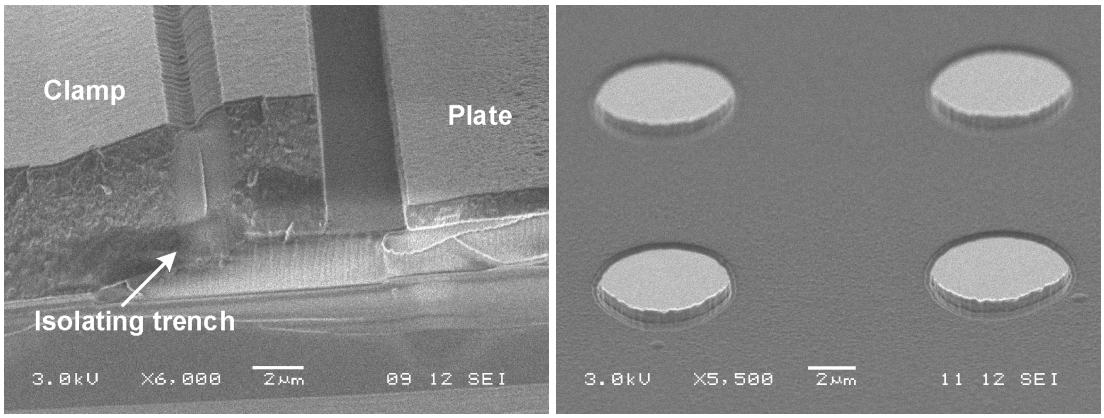

Figure 8.5: SEM micrographs of a cross-section of a shuffle motor showing an isolating trench (left) and the backside of the plate with isolating bumps (right).

The motor is suspended by connection springs, which guide its motion and provide voltage signals to the clamps and plate. The springs are fabricated in a 5.5 µm thick polysilicon layer and suspended 1.95 µm above the coated surface. The springs are not electrically shielded from the grounded substrate, therefore their dimensions must be carefully chosen to prevent pull-down to the substrate during operation. Three types of shuffle motor were built with variations in the plate length and clamp areas.

Dimensions of the fabricated motors are listed in Table 8.1.

Table 8.2: Dimensions of the fabricated shuffle motors.

Parameter	Symbol	Type I	Type II	Type III
Plate length [μm]	$2L$	180	208	236
Size of motor [μm x μm]	-	412 x 286	440 x 286	468 x 286
Clamp area [μm^2]	A_c	38264	40336	42408
Plate width [μm]	w		94	
Plate thickness [μm]	t		1.15	
Gap plate/substrate [μm]	g_a		1.76	
Bump height [nm]	b		210	
Insulating layer thickness [nm]	t_d		210	

8.4 MODELLING

A theoretical model, derived by Tas [1], predicts the performance of a shuffle motor operated in the stable region below the pull-in instability. In this section, we derive a model to calculate the step size of a motor operating above the pull-in voltage of the plate. We also present models for maximum force, operating voltage and power dissipation of a shuffle motor.

We consider an elastic plate with length $2L$, thickness t and width w, shown in Fig. 8.6. The plate is suspended at a distance g_a above the bottom electrode, which is covered with an insulating layer of thickness t_d.

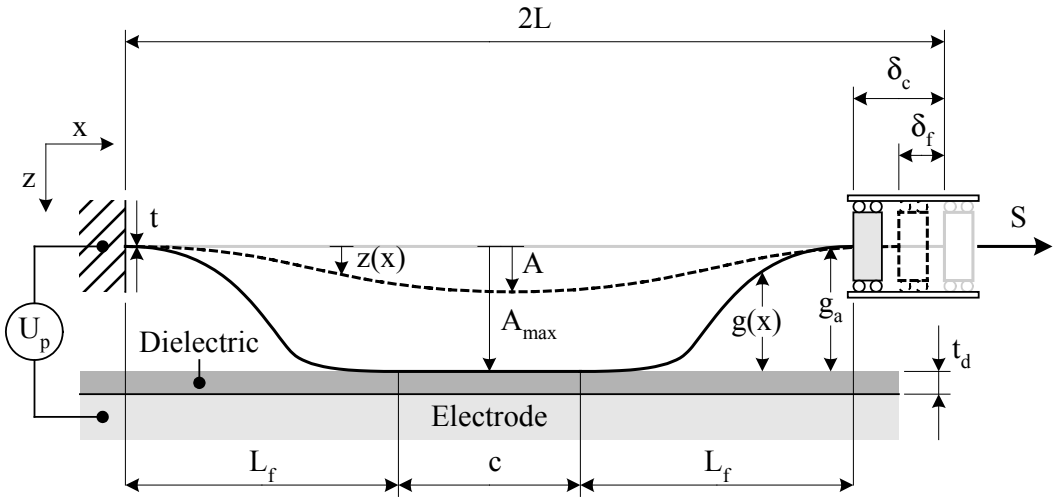

Figure 8.6: Model of the plate of a shuffle motor.

8.4.1 Step size: Non-contact mode

When a voltage U_p is applied on the plate, an electrostatic force deflects the plate towards the grounded substrate. This induces a longitudinal contraction, moving the axially unrestrained end of the plate closer to the fixed end. The longitudinal displacement δ, also called the curvature shortening, can be approximated as the difference between the length of a deflected beam and the original length L [4], given by:

$$\delta = \frac{1}{2}\int_0^L \left(\frac{dz}{dx}\right)^2 dx \qquad (8.1)$$

where z(x) is the deflection curve of the plate.

The deflection curve of half of the plate is approximated with the function

$$z(x) = \frac{1}{2}A\left(1-\cos\left(\frac{\pi x}{L}\right)\right) \qquad 0 \le x \le L \qquad (8.2)$$

where A is the center deflection of the plate. The shape function z(x) satisfies the boundary conditions ($z(0)=z'(0)=z'(L)=0$ and $z(L)=A$), giving a reasonable approximation of the real deflection profile.

The longitudinal displacement δ_f of the movable end of the plate, operated below the pull-in voltage, is obtained by substituting the assumed deflection profile into Expression 8.1:

$$\delta_f = \frac{\pi^2}{8}\frac{A^2}{L} \qquad (8.3)$$

This result is in good agreement with the one derived by Tas [1].

The maximum step size of the fabricated shuffle motors operating below pull-in is given in Table 8.3. The maximum deflection of the plate at the midpoint is assumed to be 40 % of the effective gap g_{eff}, where $g_{eff}=g_a+t_d/\varepsilon_r$.

Table 8.3: Calculated step size of the shuffle motors maximally operated below the pull-in instability.

Parameter	Symbol	Type I	Type II	Type III
Step size: Non-contact mode [nm]	δ_f	7.0	6.0	5.3

8.4.2 Step size: Contact mode

The pull-in voltage is the voltage at which the electrostatic attraction force between the plate and substrate increases faster than the restoring mechanical force causing instability and, ultimately, collapse of the plate. The pull-in voltage is a function of the geometry of the plate and axial load *S*. The pull-in voltage U_{PI} of the plate for zero axial load is given by [1]:

$$U_{PI} = \sqrt{0.75 \frac{E \cdot t^3 \cdot \left(g_a + \frac{t_d}{\varepsilon_r} \right)^3}{\varepsilon_o \cdot L^4}} \qquad (8.4)$$

When the actuation voltage equals or exceeds the pull-in voltage ($U_p \geq U_{PI}$) the plate makes physical contact with the grounded substrate, producing a relatively large longitudinal displacement, $\delta_c >> \delta_f$. The displacement δ_c corresponds to that induced by a plate of length $2L_f$ with a center deflection of A_{max}:

$$\delta_c = \frac{\pi^2}{8} \frac{A_{max}^2}{L_f} \qquad (8.5)$$

A_{max} is determined by the initial gap g_a between the plate and substrate reduced by the height of bumps ($A_{max}=g_a-b$), and $2L_f$ is the part of the plate that is not in contact with the substrate, which depends on the applied voltage U_p. By increasing the plate voltage, the contact region *c* increases, reducing the free length.

To determine the free length of the plate we consider the deflected part of length L_f, as illustrated in Fig. 8.6. The electrostatic force F_e working on this part is given by:

$$F_e = U_p^2 \int_0^{L_f} \frac{1}{2} \frac{\varepsilon_o \cdot w}{\left(g_a - z(x) + \frac{t_d}{\varepsilon_r} \right)^2} dx \qquad (8.6)$$

where ε_o is the permittivity of air and ε_r the relative permittivity of the insulating layer. The mechanical restoring force of the deflected part can be approximated as the force required to deflect a cantilever beam with the guided-end boundary condition a distance A_{max},

$$F_m = \frac{E \cdot t^3 \cdot w}{L_f^3} \cdot A_{max} \qquad (8.7)$$

where E is Young's modulus of the plate.

The free length as function of the applied voltage can be calculated by equating the electrostatic and mechanical restoring force (F_e=F_m). It follows from Equations 8.5 and 8.6 that the free length is independent of the original length L of the plate. This implies that the shuffle motors with different plate lengths will have the same step size when the actuation voltage exceeds the pull-in voltage of the plate.

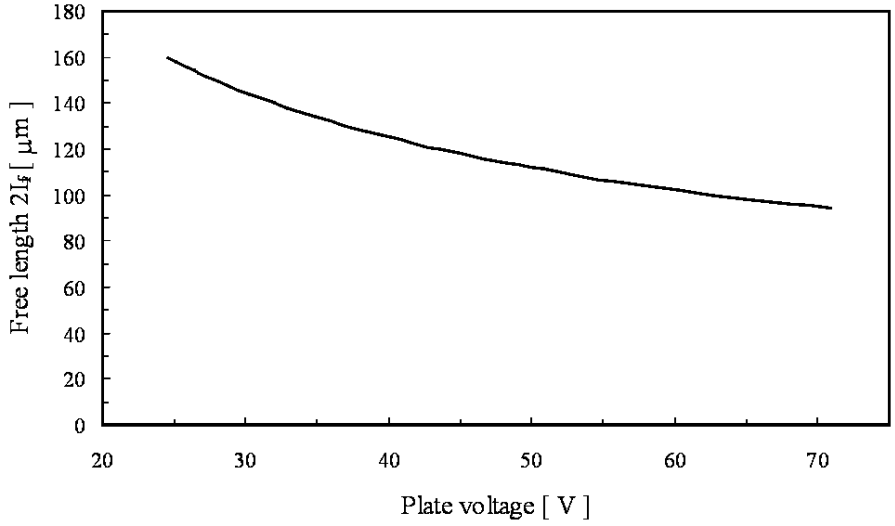

Figure 8.7: Calculated free $2L_f$ length versus applied plate voltage for the fabricated shuffle motors.

Fig. 8.7 shows the calculated free length of the plate as a function of the applied plate voltage for the fabricated shuffle motors. The calculation is performed using the dimensions of the shuffle motor listed in Table 8.1. Also used are Young's modulus of polysilicon E=160 GPa, premittivity of air ε_o=8.85 $\cdot 10^{12}$ and relative permittivity of silicon nitride insulating layer ε_r=7.5.

The longitudinal displacement δ_c of the movable end of the plate, operated above the pull-in voltage, is obtained by substituting the calculated free length into Expression 8.5. Predicted pull-in voltage and step size of the fabricated shuffle motors operated in the contact mode are listed in Table 8.4.

Table 8.4: Calculated pull-in voltage and step size of the shuffle motors operated above the pull-in instability.

Parameter	Symbol	Type I	Type II	Type III
Pull-in voltage [V]	U_{PI}	42.2	31.6	24.5
Step size: Contact mode [nm] (*plate voltages from U_{PI} to 70 V*)	δ_c	48 - 62	42-62	37-62

8.4.3 Output force

A shuffle motor employs deflection and relaxation of an elastic plate for pulling and pushing of a non-activated clamp, as illustrated in Fig. 8.2.

Deflection of the plate reduces its longitudinal extent and displaces the non-activated clamp. When a tensile load S is applied to the clamp, as shown in Fig. 8.6, an axial strain is induced in the plate, reducing the clamp displacement. If the axial strain is equal to the deflection-induced shortening δ, the net displacement of the clamp will be zero. The axial force associated with this strain is the maximum force that can be pulled by the shuffle motor,

$$F_{pull} = \frac{E \cdot t \cdot w}{2L} \delta \qquad (8.8)$$

Relaxation of the plate pushes the non-activated clamp. A compressive load S grater than or equal to the buckling force of the plate will prevent stretching. The

buckling load of the plate is thus the maximum load a shuffle motor can push. The buckling load of a rectangular plate clamped on the both ends is given by

$$F_{push} = \frac{\pi^2}{3}\frac{E \cdot w \cdot t^3}{L^2} \tag{8.9}$$

Depending on the geometry of the plate, the maximum output force of the shuffle motor will be limited by either the pulling or pushing force.

In order to transmit the force produced by the plate, a sufficient clamp force is required. The normal force F_n is generated by applying a voltage difference Uc between the clamp and grounded substrate,

$$F_n = \frac{1}{2}\frac{\varepsilon_o \cdot A_c}{\left(b + \frac{t_d}{\varepsilon_r}\right)^2} U_c^2 \tag{8.10}$$

where A_c is the clamping area. The normal force induces a frictional force F_t in the clamp, which magnitude depends on the coefficient of friction μ ($F_t = \mu \cdot F_n$). In order to prevent slipping of the clamps the frictional force must be larger than the maximum output force of the motor. The coefficient of friction between silicon nitride/silicon nitride contacts is between 0.55 to 0.85 [5].

The predicted maximum output force of the fabricated shuffle motors is in the mN range, and is limited by the pushing force, as shown in Table 8.5. A clamp voltage up to 60 V should be sufficient to generate the required frictional force.

Table 8.5: Predicted output force of the shuffle motors.

Parameter	Symbol	Type I	Type II	Type III
Maximum pull force [mN]	F_{pull}	4.8	4.2	3.7
Maximum push force [mN]	F_{push}	2.3	1.7	1.3
Clamp force [mN] (*15 V- 60 V*)	F_n	0.7 - 10.8	0.7 - 11.3	0.7 - 11.9
Frictional force [mN] (*15 V- 60 V, μ=0.55*)	F_t	0.4 - 5.9	0.4 – 6.2	0.4 – 6.5

8.4.4 Power

The power P dissipated by the shuffle motor can be approximated by considering charging and discharging of the capacitors that make up the motor [6]:

$$P = \left(2C_{clamp} + C_{plate}\right) \cdot U^2 \cdot f_c \tag{8.11}$$

where C_{clamp} is the maximum capacitance of one of the clamp, C_{plate} the maximum capacitance of the plate, U the driving voltage and f_{c} is the cycling frequency. The maximum capacitance of the clamp is cgiven by

$$C_{clamp} = \frac{\varepsilon \cdot A_c}{\left(g_a + \frac{t_d}{\varepsilon_r}\right)} \tag{8.12}$$

To calculate the maximum capacitance of the plate, we assume that 60 % of its length is in contact with the substrate,

$$C_{plate} = \frac{\varepsilon \cdot 0.6(t \cdot w)}{\left(g_a + \frac{t_d}{\varepsilon_r}\right)} \tag{8.13}$$

The capacitance of the free length of the plate may be neglected in the calculation. Using the dimensions of the Type I shuffle motor given in Table 8.2, the driving voltage of 55 V and the cycling frequency of 80 kHz, this predicts a dissipation of 780 µW.

8.5 MEASUREMENTS

In this section, we report on measurements of speed, step size and output force, performed on the fabricated shuffle motors. Unless otherwise mentioned, the measurement results apply to the Type I motor with a plate length of 180 µm.

8.5.1 Stepping motion

We have successfully generated stepping motion with the shuffle motors using a coordinated sequence of clamp and plate voltages. The appropriate voltage sequence is generated using a multichannel analog output card and high voltage amplifier with high slew rate. We used the same voltage sequence as the one shown in Fig. 10.12. After each operation cycle, the polarity of the actuation voltage is reversed in order to reduce charge accumulation in the insulating silicon nitride layer.

Fig. 8.8 shows a typical measurement of the motor position versus time. The motor was actuated at a cycling frequency of 1Hz and a driving voltage of 45 V for both the clamps and plate.

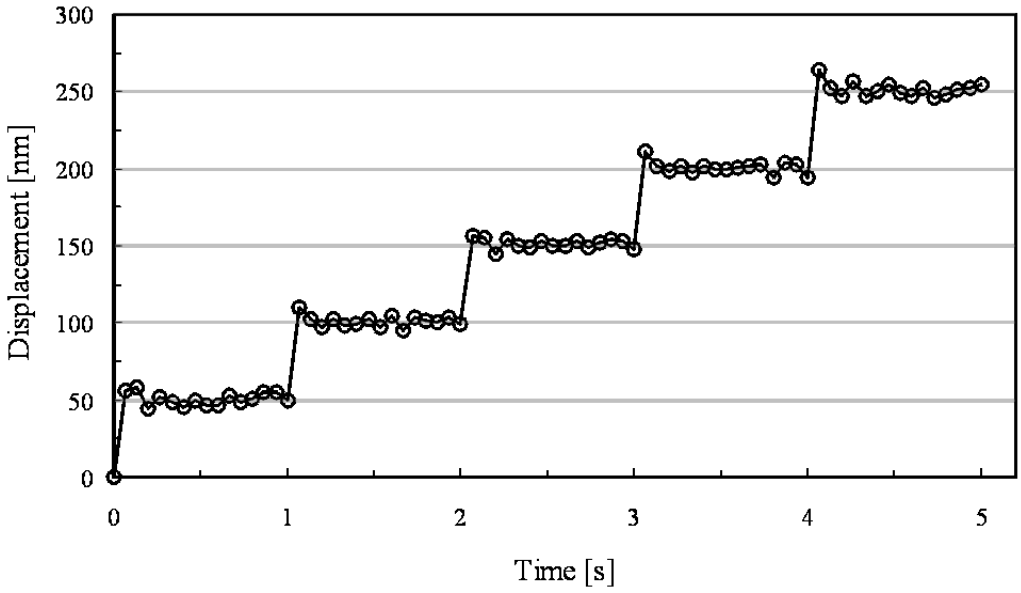

Figure 8.8: Displacement of a shuffle motor versus time. Data were taken at a stepping frequency of 1 Hz and a voltage of 45 V for both the clamps and plate.

The positioning performance of the motors was measured using an image processing technique, based on the Fourier transform [7]. This technique allows in-plane sub-pixel displacement measurements with a resolution of a few nanometers. Due to the high resolution of the measurement, the individual steps

can be clearly resolved. The step size was found to be 50 nm, which is in good agreement with the theoretical prediction (see Table 8.4).

The maximum displacement range of the motor was limited to ± 70 µm by suspension design. To achieve this relative large stroke we used a motor suspended by a rather compliant suspension. Fig 8.9 shows the motor displacement versus time spanning the entire displacement range.

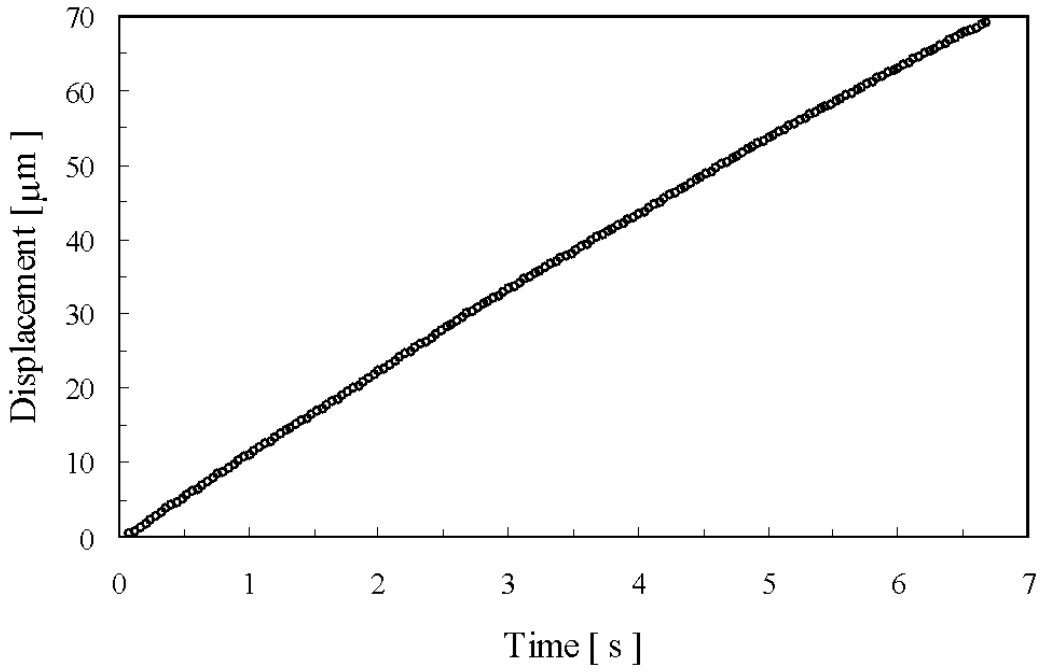

Figure 8.9: Displacement of a shuffle motor versus time. Data were taken at a stepping frequency of 200 Hz and voltages of 30 V and 50 V for the clamps and plate, respectively.

8.5.2 Speed

The speed of the motor is determined by measuring the distance travelled for a given driving frequency and a fixed number of steps (typically 100 steps) [2]. For each frequency, we took an average value of three measurements. The average deviation for each measurement point was smaller than 0.1 %. Fig. 7 shows the speed of the shuffle motor as a function of the stepping frequency. The data were

taken at frequencies up to 80 kHz with both clamps and plate driven at 45 V. The maximum frequency range of 80 kHz was limited by the driving electronics.

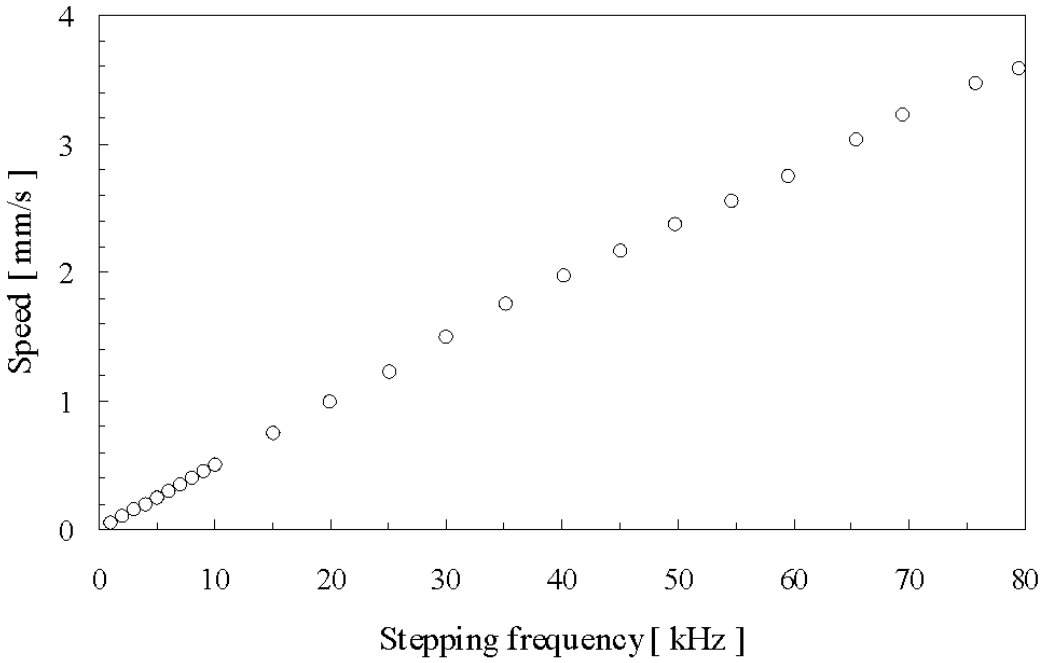

Figure 8.10: Measured speed of the actuator versus stepping frequency with clamps and plate driven at 45 V.

The velocity is nearly linear with cycling frequency over the measured range with a maximum velocity of 3.6 mm/s at 80 kHz. Considering the plate resonance frequency calculated to be 304 kHz, a considerable larger cycling frequency and speed is expected by improving the drive electronics. The slope of the speed curve is a measure for the average step size, which was about 50 nm.

8.5.3 Dependence of step size on plate voltage

The velocity of the shuffle motor depends on the cycling frequency as well as the average step size. The step size of the motor is a function of the degree of plate deformation, which is directly related to the plate actuation voltage, as shown in Fig. 8. 11. These measurements were performed at a cycling frequency of 200 Hz and a clamping voltage of 30 V. The pull-in voltage was measured to be 39 V, which agrees reasonably with the calculated 42.2 V (see Table 8.4).

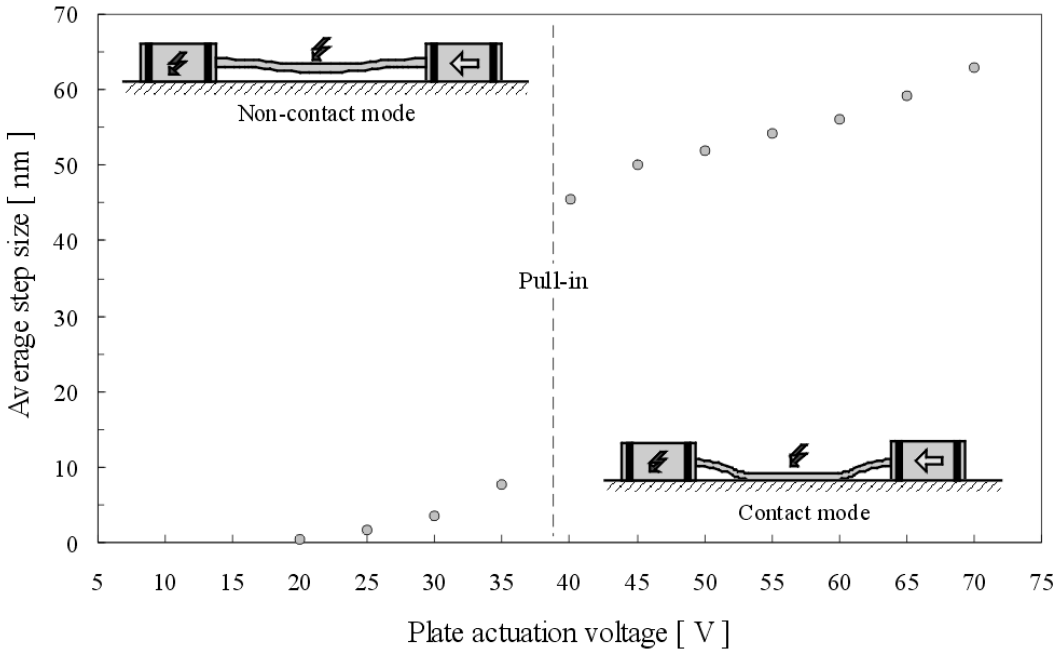

Figure 8.11: Measured average step size versus plate actuation voltage. Clamp voltage of 30 V and cycle frequency of 200 Hz are used.

We have observed an average step size from 0.6 to 7.0 nm for the motor operated below the pull-in voltage. Operation of the plate above the pull-in instability causes the plate to collapse on the substrate, resulting in a large plate deformation and significant increase in step size. We have measured adjustable nanometer-resolution steps ranging between 46 nm and 62 nm corresponding to plate voltages between 40 V and 70 V. The measured step size for both non-contact and contact operating modes are in fair agreement with the theoretical prediction listed in Tables 8.3 and 8.4.

Measurements of the average step size for the three types of shuffle motor operated above pull-in are shown in Fig. 8.12. The measured step size is in good agreement with the theoretical prediction (Section 8.4.2) and does not depend on the length of the plate.

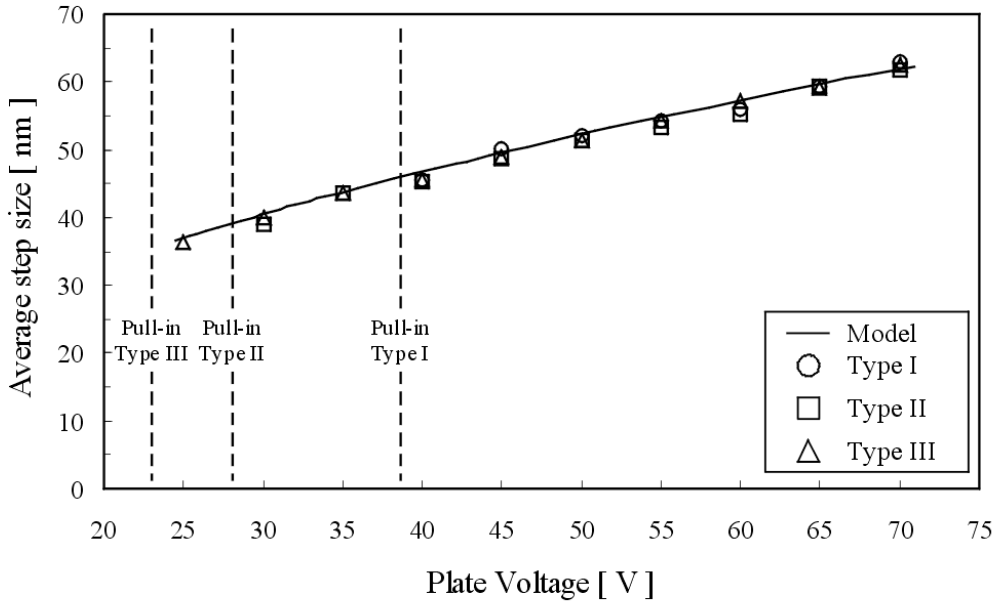

Figure 8.12: Average step size of the fabricated shuffle motors, operated above the pull-in instability.

8.5.4 Output force

To determine the output force of the motors as a function of the driving voltage, we measured the maximum displacement range while varying the voltages on the clamps and plate. The output force was deduced from the displacement measurements and the calculated stiffness of the suspension. A stiff suspension was employed to allow force measurements over a wide range of output forces.

The shuffle motors used in the measurements were suspended by the connection springs on both clamps, as shown in Fig. 8.13. Since the motor works against half of the connection springs at any given time (the activated clamp balances the force of the connection springs attached to it), one half of the total suspension stiffness was used in the calculation. Either in the pull or push mode the spring force can limit the maximum displacement of the motor. In the pull mode, the displacement is maximized when the tensile load on a non-activated clamp is sufficient to raise the pull-in voltage above the driving voltage. The maximum displacement in the push mode is reached when the compressive load exceeds the plate buckling force.

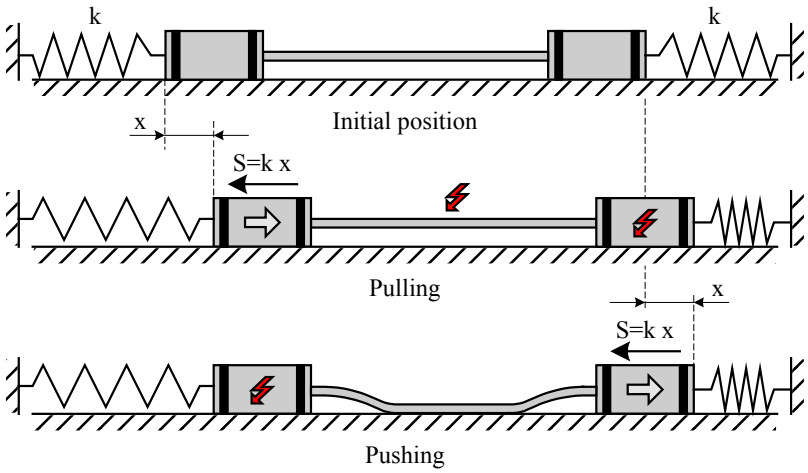

Figure 8.13: Schematic view of the suspension of the shuffle motor used in force measurements.

The measurements were performed on all three types of shuffle motor, using clamp voltages from 15 V to 60 V. The motors were operated above the pull-in instability. Typical data, taken on the Type I motor, are shown in Fig. 8.14.

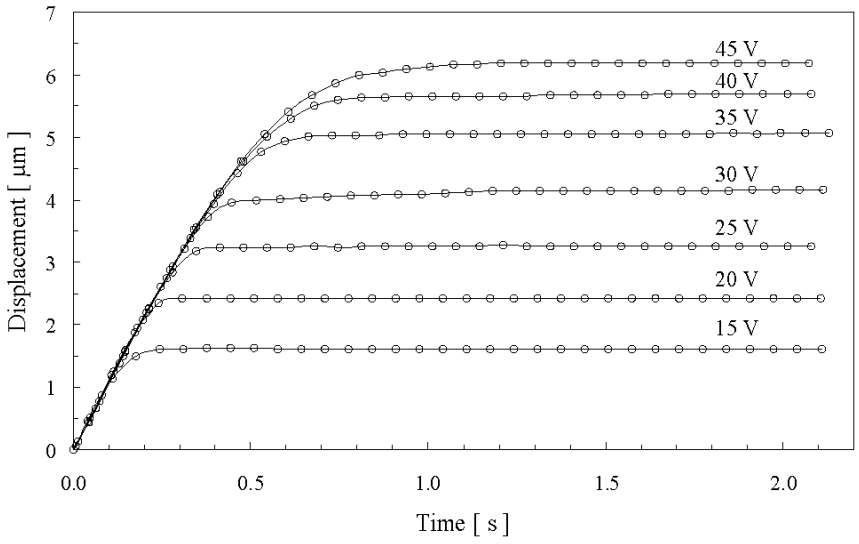

Figure 8.14: Displacement of a shuffle motor (Type I) versus time for different clamp voltages. Data was taken at a stepping frequency of 200 Hz and plate voltage of 55 V.

Figures 8.15, 8.16 and 8.17 show the output force as a function of the square of the clamp voltage for the three types of shuffle motor, operated at different plate voltages.

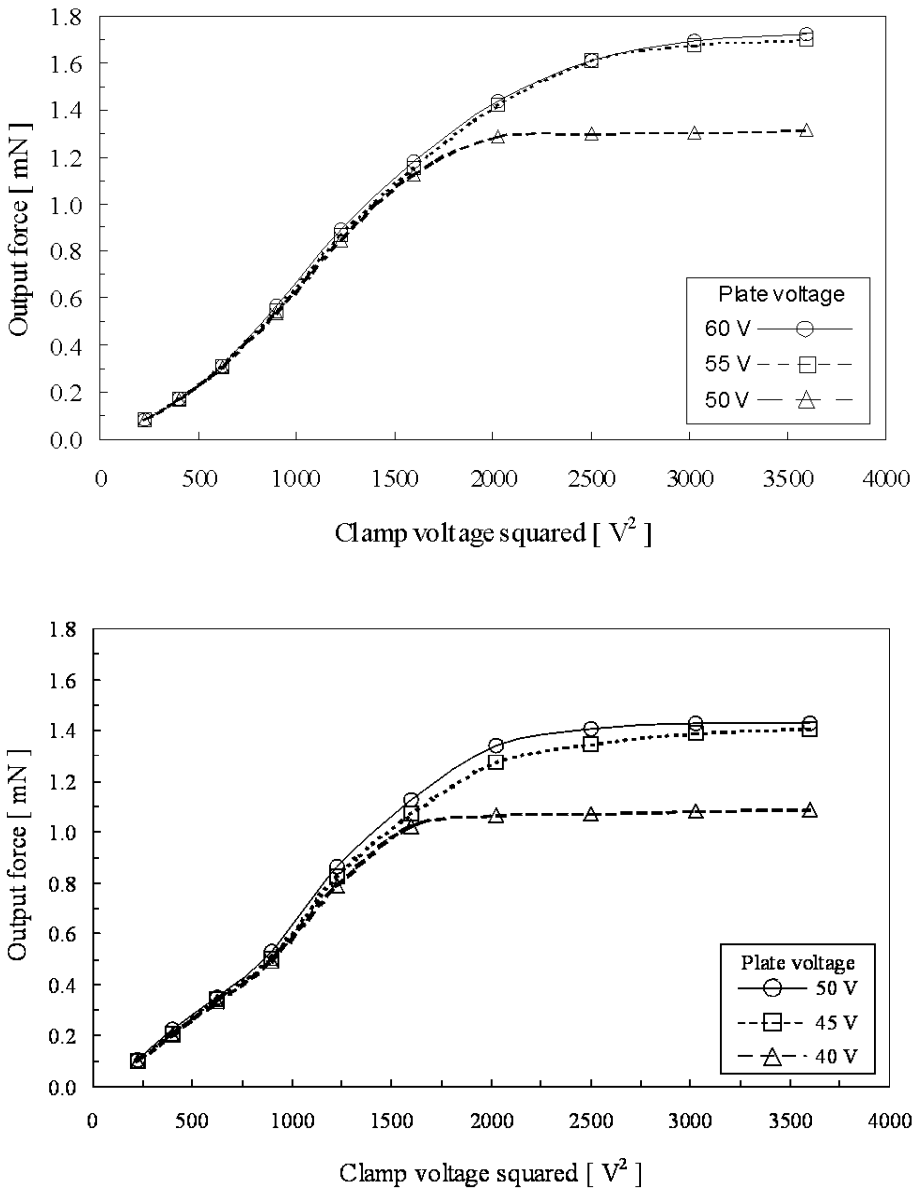

Figure 8.15: Measured output force of the shuffle motors versus clamp voltage for different plate actuation voltages at cycle frequency of 200 Hz: Type I (above) and Type II (below).

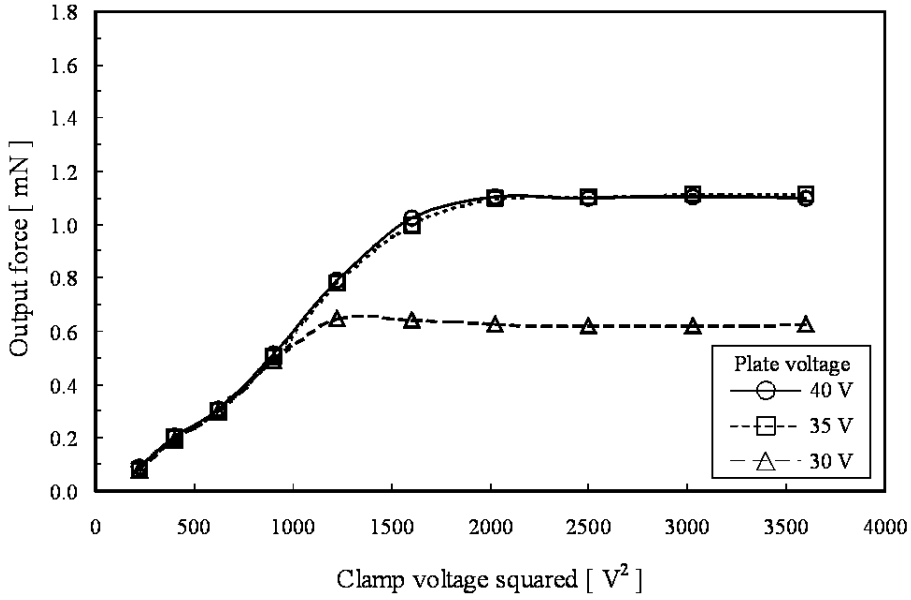

Figure 8.16: Measured output force of the Type III shuffle motor versus clamp voltage for different plate actuation voltages at cycle frequency of 200 Hz.

The output force characteristics are qualitatively similar for all three types of motor. At lower plate voltages, the tensile load, induced by the suspension, limits the output force of the motor. The tensile load on a non-activated clamp, which increases monotonically with displacement of the motor, raises the pull-in voltage of the plate. At a certain displacement, the tensile load is sufficiently high to raise the pull-in voltage above the driving voltage, preventing the motion of the motor. By increasing the plate voltage, the output force increases until it saturates at some maximum value, which is limited by the buckling force of the plate.

The maximum output force of the Type III motor with 236 μm long plate was 1.1 mN (see Fig. 8.17), which is in good agreement with the theoretical value of 1.3 mN (see Section 8.4.3). Using the expression for the buckling force (Expression 8.9) in combination with the measured output force and the length of the plate of the type III motor, the output force of the type II motor can be accurately predicted:

$$F_{II} = \frac{F_{III} \cdot L_{III}^2}{L_{II}^2} = \frac{1.1 \cdot 236^2}{208^2} = 1.4 \text{ mN} \qquad (8.14)$$

This prediction is in excellent agreement with the measured force of 1.4 mN, as shown in Fig. 8.15. The same calculation for the Type I motor with a plate length of 180 μm predicts a maximum output force of 1.9 mN, which is less than the measured force of 1.7 mN, as shown in Fig. 8.15. This suggests that the maximum output force of the Type I motor is actually limited by the clamp force. From the force curve, shown in Fig. 8.15, we can see that the clamp force is not proportional to the clamp voltage squared, as expected from Expression 8.10. The deviation is pronounced at voltages above 40 V. Also, the slope of the force curves is smaller at low clamp voltages. We believe that this is due to the moment induced in the clamp by the deflection of the plate, which reduces the active clamp area and thereby diminishing the clamping force.

A maximum output force of 1.7 mN was demonstrated by the Type I shuffle motor with actuation voltages of 55 V on both clamps and plate. The motor achieved a force density of 9651 N/(m^3V^2) and a power density of $1.05 \cdot 10^5$ W/m^3, which are the highest values reported so far for electrostatic microactuators (see Ref. [8] and Appendix A).

8.5.5 Dependence of step size on load

The step size of a shuffle motor is a function of the load applied to the clamps, as shown in Fig. 8.17.

To investigate this dependence, we suspended the motor with connection springs on both clamps, as schematically illustrated in Fig. 8.14, and measured its displacement as a function of time at a fixed cycling frequency. From this we extracted the step size as a function of the displacement and related it to the mechanical restoring force applied by the connection springs. When the motor walked against the springs in the forward motion, the step size decreased from 53 nm at zero load to 9 nm at 1.5 mN. When the motor travelled backward, the spring force assisted the motion, increasing the step size to 88 nm at a load of 1.5 mN. The step size changes linearly with the applied load.

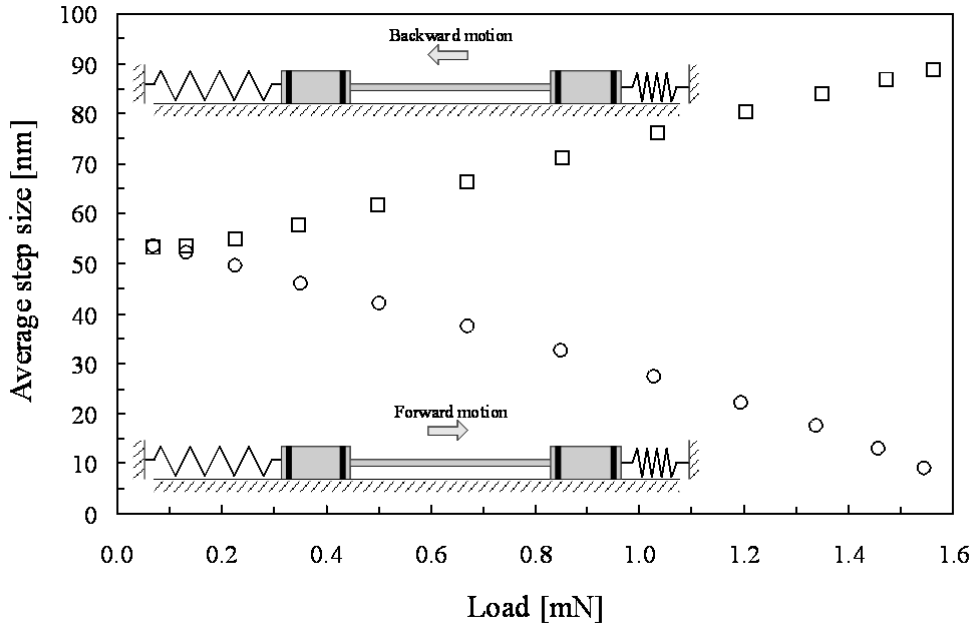

Figure 8.17: Step size of the shuffle motor versus the load on the clamps. The data were taken at cycling frequency of 200 Hz with clamp and plate voltages of 55 V.

8.5.6 Life time

A limited lifetime test was conducted to determine the durability of the shuffle motor. The motor was run for five days at a cycling frequency of 80 kHz, generating nearly 34 billion steps, equivalent to a displacement of 1.5 km. This did not result in a noticeable change in performance.

8.6 CONCLUSIONS

A bidirectional electrostatic linear stepper micromotor is presented. Small size and good performance characteristics in terms of output force, positioning resolution, speed, durability and power consumption make this motor a promising candidate for diverse MEMS applications, such as probe-based data storage systems.

8.7 REFERENCES

1 Tas N, Wissink J, Sander L, Lammerink T, Elwenspoek M 1998 Modeling, design and testing of the electrostatic shuffle motor *Sensors and Actuators* A **70** 171-8

2 de Boer M P, Luck D L, Ashurst W R, Maboudian R, Corwin A D, Walraven J A, Redmond J M 2004 High performance surface-micromachined inchworm actuator *J. Microelectormech. Syst.* **13** 63-74

3 Rodgers M S and Sniegowski J J 1998 5-level polysilicon surface micromachining technology: Application to complex mechanical systems *Solid-State Sensors and Actuators Workshop Hilton Head Island* (South Carolina, USA) 144-149

4 Gere J M and Timoshenko S P 1991 Mechanics of materials, Chapman & Hall, London

5 Deng K and Ko W H 1992 A study of static friction between silicon and silicon compounds *J. Micromech. Microeng.* **2** 14-20

6 Yeh R, Hollar S and Pister K S J 2002 Single mask, large force and large displacement electrostatic linear inchworm motors *J. Microelectormech. Syst.* **11**(4) 330-336

7 Vanapalli S 2004 Techniques for characterization of in-plane displacement for microactuators *M.Sc Thesis* Department of Electrical Engineering, University of Twente, The Netherlands.

8 Yeh R, Hollar S and Pister K S J 2002 Single mask, large force and large displacement electrostatic linear inchworm motors *J. Microelectormech. Syst.* **11**(4) 330-336

9 Fearing R S 1998 Powering 3 dimensional microrobots: Power density limitations *Tutorial on Micro Mechatronics and Micro Robotic*, ICRA

Chapter 9

Two degrees of freedom (2DOF) electrostatic linear stepper motor

Abstract

In this chapter, we present an electrostatic linear stepper micromotor with two translational degrees of freedom. The motor employs built-in mechanical leverage to convert normal deflection of a flexible cross-plate into a small in-plane step and four electrostatic clamps to enable bidirectional stepping motion in two orthogonal directions. The motor is realized in a relative simple fabrication process, which combines conventional surface micromachining with vertical trench isolation. Operation in full, half and diagonal stepping modes was accompanied with high overall performance characteristics such as large force (0.92 mN) at moderate voltage (45V plate and 36V clamp), adjustable nanometer-resolution step size (41 nm to 63 nm), broad cycling frequency range (up to 80 kHz), small dimension (482 μm x 482 μm) and large displacement range (± 30 μm). These features make it an attractive candidate for demanding positioning applications e.g. for (probe based) data storage.

9.1 INTRODUCTION

The electrostatic shuffle motor presented in the previous chapter exploits a built-in mechanical leverage to convert normal deflection of an elastic plate into a powerful, high resolution, step. Two voltage-controlled clamps allow stepping motion over a large displacement range, which is limited only by the dimension of the guidance. This motor is a promising candidate to perform positioning of the recording medium in probe-based data storage systems such as the micro Scanning Probe Array Memory (μSPAM) introduced in the first chapter. This is due to its small size, large displacement range and force, high speed and positioning resolution, reliability and low power consumption. However, the operation of the motor was limited to bidirectional motion along a single axis, whereas implementation of the μSPAM concept requires planar motion.

In this chapter, we report on the design and fabrication of the first electrostatic shuffle micromotor with two translational degrees-of-freedom (2DOF).

9.2 2DOF SHUFLLE MOTOR

Fig 9.1 shows a schematic view of a 2DOF shuffle motor.

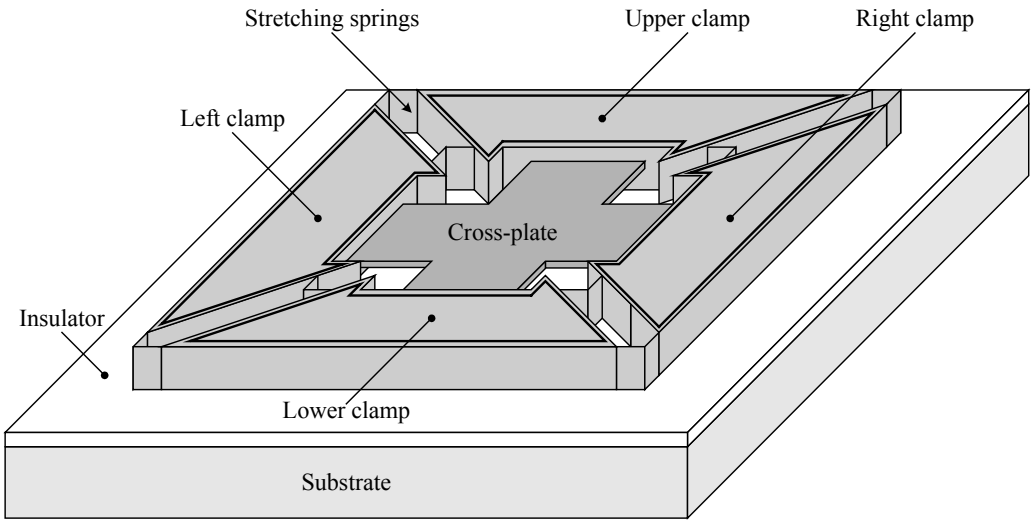

Figure 9.1: A schematic view of a 2DOF shuffle motor.

The motor consists of a flexible cross-plate and four voltage-controlled clamps at the ends of the plate. Stretching springs are employed to additionally connect

neighbouring clamps, guiding their relative motion. The plate and the clamps are mutually electrically insulated, allowing individual biasing of each of these components. The motor moves over an unpatterned substrate, coated with an insulating layer. The substrate is electrically grounded during operation. Driving voltage signals to the clamps and cross-plate are provided through the suspension (not shown in Fig. 9.1). The insulating layer prevents short-circuiting during operation.

By applying an appropriate voltage sequence a walking motion of the 2DOF shuffle motor may be achieved, as illustrated in Fig. 9.2.

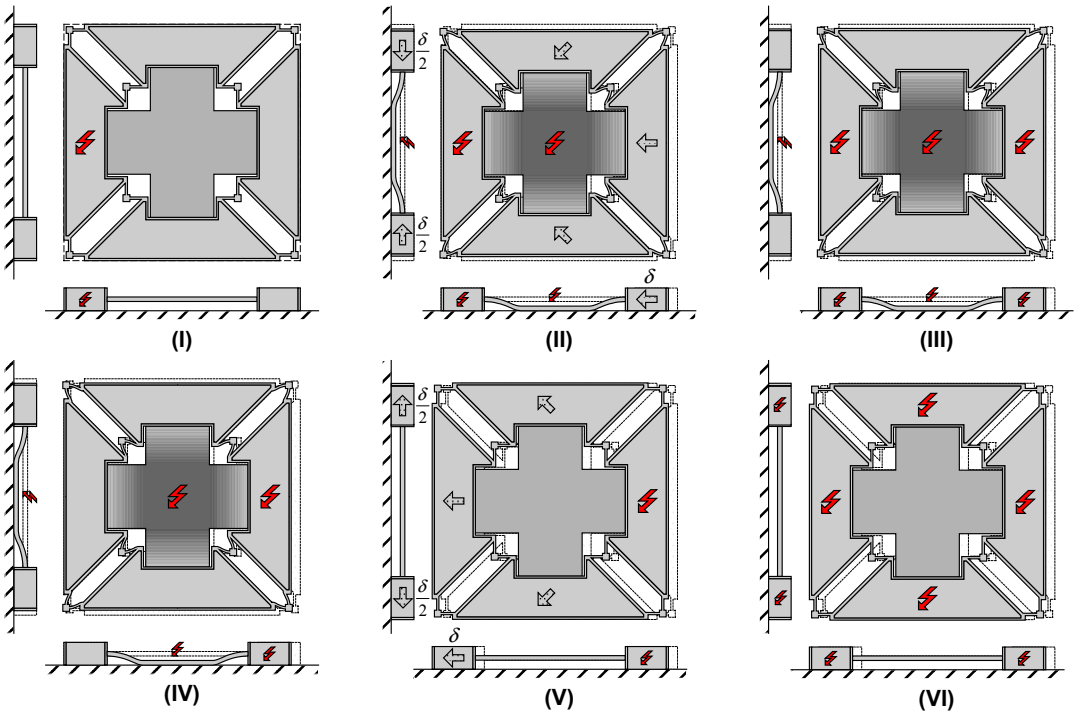

Figure 9.2: Voltage actuation sequence for a single step to the left: (I) Left clamp is activated, (II) Deflection of the cross plate causes a powerful contraction, (III) Right clamp is activated, (IV) Left clamp is released, (V) Stretching of the cross plate moves the clamps, (VI) All clamps activated.

The actuation sequence begins with activation of a first clamp by applying a voltage difference between the clamp and the grounded substrate (*I*). The applied voltage induces a normal electrostatic force that prevents sliding of the activated clamp. Subsequently, a voltage is applied on the cross-plate, causing a deflection

of the plate towards the substrate. The normal deflection of the cross-plate induces a lateral contraction of the entire motor, moving the inactive clamps closer to the activated clamp (*II*). Since the normal deflection is much larger than the induced contraction there is a built-in mechanical leverage, resulting in a small but powerful step. Next, a second clamp on the opposite side of the cross-plate is activated in the new position (*III*). The first clamp is then released (*IV*). The released cross-plate stretches and pushes the inactive clamps outwards (*V*). The actuation sequence is completed by activation of all clamps (*VI*). At the end of the actuation sequence, the entire motor is moved by a single step and is ready to make another step in a desired direction. A large displacement in a two-dimensional plane can be achieved by successively adding a large number of steps.

A 2DOF shuffle motor can be operated in different stepping modes by a simple adjustment of the voltage actuation sequence. The actuation sequences for full, half and diagonal stepping modes are shown in Figure 9.3.

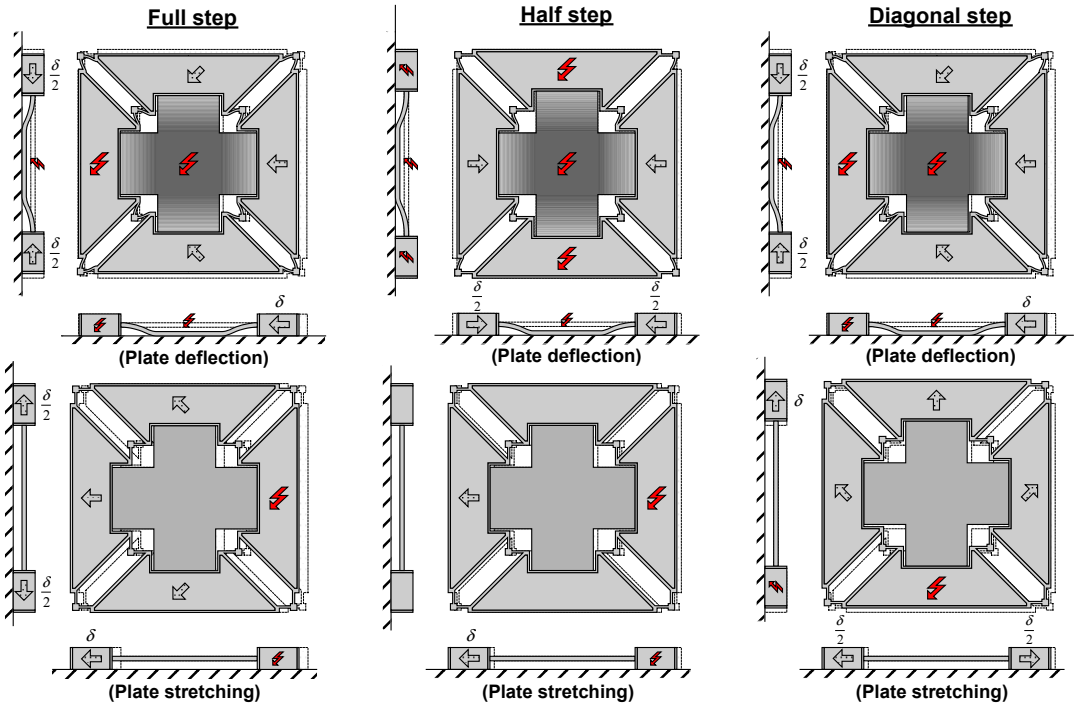

Figure 9.3: Voltage actuation sequences for full (left), half (middle) and diagonal (right) stepping modes.

9.3 FABRICATION PROCESS

We use vertical trench isolation combined with a conventional surface micromachining process, introduced in Chapter 2, to fabricate the proposed 2DOF shuffle motor. A relatively simple fabrication process, illustrated in Figure 9.4, employs four photolithographic masks and only two polycrystalline silicon device layers.

The fabrication process starts on a highly conductive silicon substrate. The selected substrate is coated with a 210 nm low-stress silicon nitride layer using Low Pressure Chemical Vapor Deposition (LPCVD). On the coated substrate, we deposit a first silicon oxide layer with a thickness of 1.55 μm by Plasma Enhanced CVD (PECVD). The silicon oxide layer is then patterned in a BHF solution to form molds for the clamp feet (*Step 1*). On the patterned surface, we deposit a second PECVD silicon oxide layer with a thickness of 0.5 μm (*Step 2*). The thickness of the second silicon oxide layer determines the distance between a non-activated clamp and the coated surface of the substrate. After formation of the molds, we deposit a first 1.15 μm polysilicon layer by LPCVD. The deposited polysilicon layer is then highly doped with boron using diffusion from a solid source. The thickness of the first polysilicon layer determines the thickness of the cross plate. On the first polysilicon layer, we deposit a 100 nm PECVD silicon oxide layer and pattern it by BHF to define the form of the cross-plate (*Step 3*). The thin silicon oxide layer serves as an etching mask in a subsequent plasma etching step (*Step 7*). In the next fabrication step, we deposit a second LPCVD polysilicon layer with a thickness of 4.35 μm, covering completely the patterned silicon oxide (*Step 4*). This polysilicon layer is then doped with boron using again diffusion from a solid source. The 5.5 μm aggregate thickness of the two polysilicon layers determines the thickness of the clamps. A large thickness is preferable in order to achieve mechanically stiff clamps. Next, we etch 2 μm wide isolating trenches in polysilicon by Deep Reactive Ion Etching (DRIE) (*Step 5*). They are refilled with low stress LPCVD silicon nitride. A 1.2 μm thick layer is employed in an effort to completely refill the isolating trenches. Silicon nitride from the top surface is removed by maskless RIE (*Step 6*).

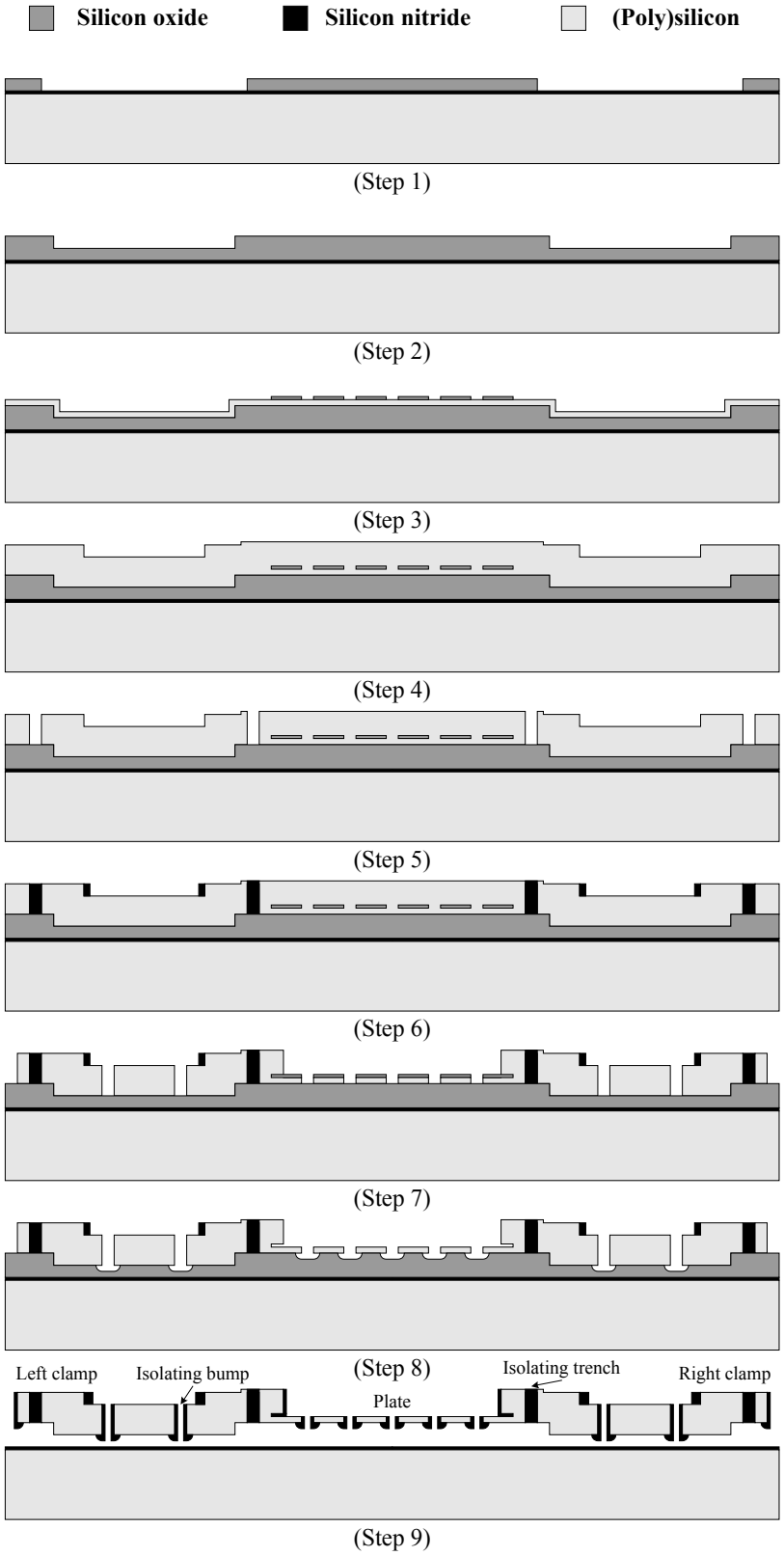

Figure 9.4: Condensed fabrication sequence of 2DOF shuffle motor.

In a second DRIE step, we machine the layout of the motor (*Step 7*). The silicon oxide mask, hidden between two polysilicon layers, protects the underlying polysilicon during plasma etching. In this way, we employ only a single plasma etching step to machine the flexible plate and stiff clamps. After plasma etching, isolating bumps [7] are created on the backsides of the clamps and cross-plate. A short isotropic etch of sacrificial silicon oxide is applied (*Step 8*), followed by deposition a low stress LPCVD silicon nitride layer. The top silicon nitride layer is removed by a maskless RIE step, leaving material on sidewalls and under the polysilicon layer.

In the last fabrication step, the motor is released by removal of the sacrificial silicon oxide layer in 50 % HF (*Step 9*). Fig. 9.4 shows a released 2DOF shuffle motor.

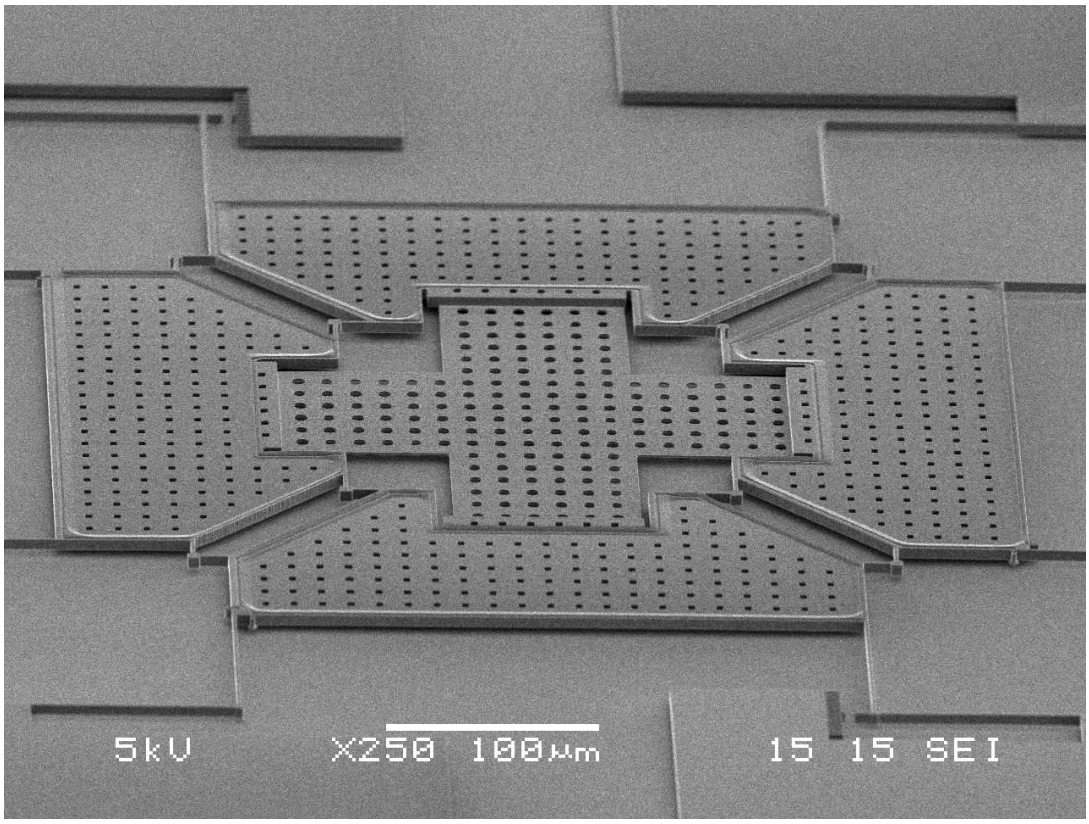

Figure 9.5: SEM micrograph a 2DOF shuffle motor after release.

9.4 FABRICATION RESULTS

A successfully fabricated 2DOF shuffle motor, with all components, is shown in Figure 9.6.

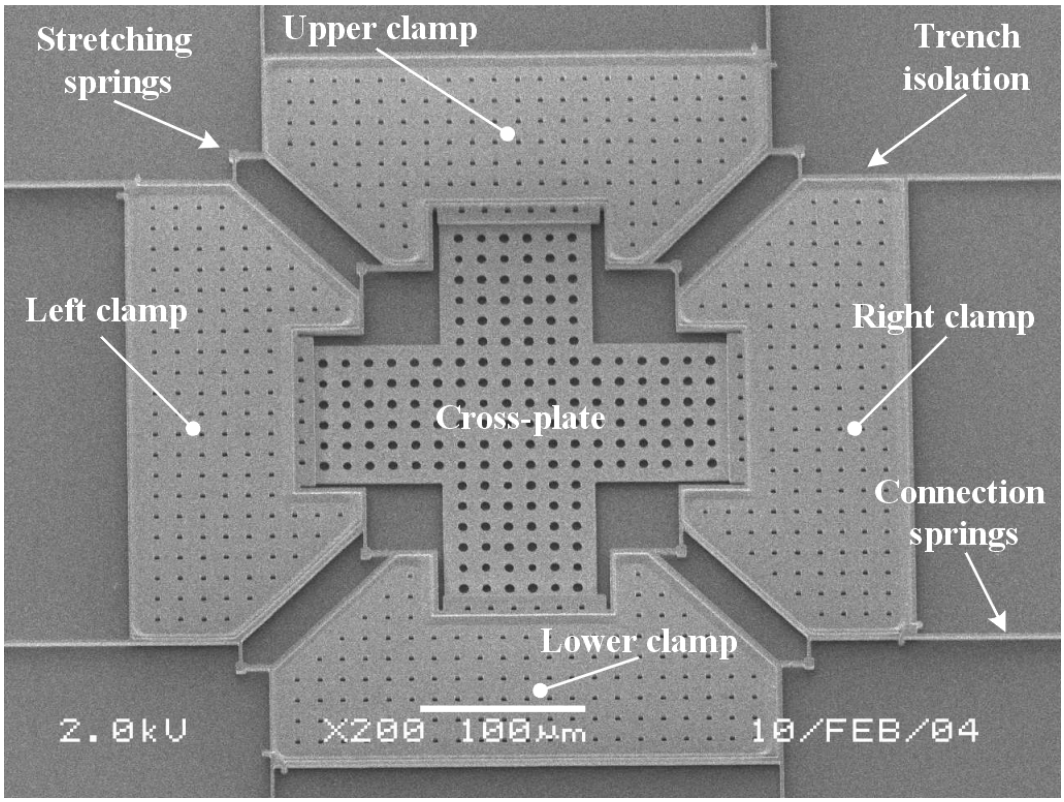

Figure 9.6: SEM micrograph of a fabricated 2DOF shuffle motor with all components.

The entire motor, including four clamps and a cross-plate, fits in an area of 482 µm x 482 µm. The legs of the cross-plate are 80 µm long and 94 µm wide. The thickness of the cross-plate is 1.15 µm. At the ends of the plate, four clamps are located. The total active area of a single clamp is approximately 32400 μm^2. The motor is mechanically suspended by 8 crab-leg flexures (2 flexures per clamp), which also provide the driving voltage to the clamps and plate. Both the thigh and shin segment of a crab-leg flexure are 100 µm long and 1.95 µm wide (1.65 µm polysilicon core with 165 nm silicon nitride faces). The flexure is 5.5 µm high and suspended 2.05 µm above the coated surface. The calculated stiffness of a single

crab-lag flexure in both X and Y directions is 5.73 N/m. The Young's modulus of 160 GPa for polysilicon and 290 GPa for silicon nitride was used in calculation.

Electrical insulation of a clamp from the cross-plate and other clamps was achieved by isolating trenches refilled with a low-stress silicon nitride, as shown in Fig. 9.7 (left).

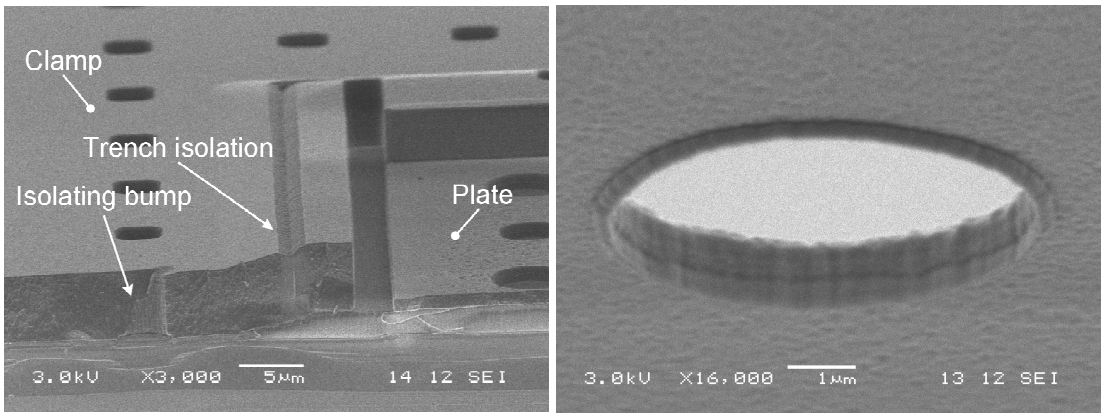

Figure 9.7: SEM micrograph of the cross-section of a 2DOF shuffle motor before the release (left) and isolating bump made of silicon nitride (right).

Isolating silicon nitride bumps are evenly divided over the backside surfaces of the clamps and the plate. An SEM micrograph of an isolating bump, located on the plate, is shown in Fig. 9.7 (right). During operation of the motor only isolating bumps make contact with the silicon nitride coating on the wafer surface, reducing charge accumulation. The contact area is significantly reduced due to the rounded shape of the rim of the bumps. The reduction of the contact area prevents stiction of the motor during fabrication and operation. The isolating bumps have a height of 210 nm. The height of bumps determines the distance between an activated clamp and the coated surface. Bumps placed on the backside of the cross-plate limit its maximum deflection. A maximum deflection of 1.55 µm was determined for an initial air gap of 1.76 µm between the plate and the substrate reduced by the bump height.

Dimensions of the fabricated 2DOF shuffle and its components are summarized in Table 9.1.

Table 9.1: Dimensions of the 2DOF shuffle motor.

Parameter	Symbol	Value [μm]
Dimension of motor		482 μm x 482 μm
Width of cross-plate leg	w	94 μm
Length of cross-plate leg	L	80 μm
Thickness of cross-plate	t	1.15 μm
Initial air gap (plate/substrate)	g_a	1.76 μm
Height of bump	b	220 nm
Thickness of insulation layer	t_d	210 nm
Total area of single clamp	A_c	32400 μm^2
Height of bump	b	210 nm

9.5 MODELLING

In order to predict performance characteristics of a 2DOF shuffle motor we have derived theoretical models to calculate the pull-in voltage of a cross-plate and step size of the motor as a function of applied voltage. The model of pull-in is based on the Displacement Iteration Pull-In Extraction (DIPIE) algorithm [1].

We consider a cross-plate with a thickness t suspended above an electrode coated with an insulating layer of thickness t_d. The legs of the cross-plate have a length L and width w. Exploiting symmetry we look only at one quarter of the cross-plate, as illustrated in Fig. 9.8.

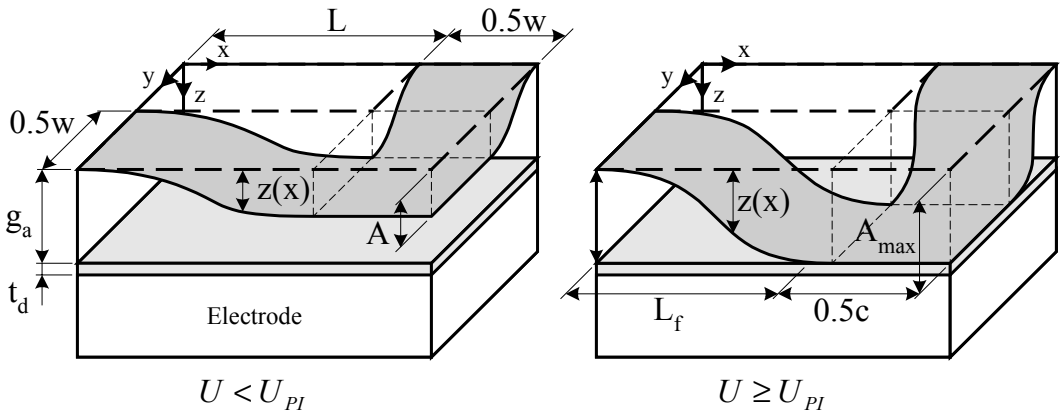

Figure 9.8: Schematic view of one quarter of a cross-plate, actuated bellow (left) and above (right) the pull-in voltage U_{PI}.

The algorithm for extracting the pull-in voltage begins with an assumed deflection of the cross-plate. We assume that the legs of the cross-plate are deformed, while the central part, with dimension *w* x *w*, moves as a rigid plate. The deflection profile *z*(x) of a leg can be approximated with the function:

$$z(x) = \frac{1}{2} A\left(1 - \cos\left(\frac{\pi x}{L}\right)\right) \qquad 0 \le x \le L \qquad (10.1)$$

where *A* is vertical displacement of the central part.

The deflection of the cross-plate gives rise to a mechanical restoring force F_m:

$$F_m = k \cdot A \qquad (10.2)$$

k is the stiffness of four legs of the cross-plate, given by:

$$k = 4\frac{E \cdot w \cdot t^3}{L^3} \qquad (10.3)$$

Next, a voltage *U* is applied on the cross-plate, inducing an electrostatic force. The electrostatic force, working on the deflected cross-plate, can be approximated as:

$$F_e = 4\int_0^L \frac{1}{2}\frac{\varepsilon_o \cdot w \cdot U^2}{\left(g_a - z(x) + \frac{t_d}{\varepsilon_r}\right)^2} dx + \frac{1}{2}\frac{\varepsilon \cdot w^2 \cdot U^2}{\left(g_a - A + \frac{t_d}{\varepsilon_r}\right)^2} \qquad (10.4)$$

where g_a is the initial air gap, ε_o is the permittivity of air and ε_r relative permittivity of the insulating layer.

By equating the mechanical restoring and electrostatic forces (F_m=F_e), the voltage required to induce the given displacement of the central part *A*, can be calculated. Sequentially increasing the displacement of the central part *A*, we can find the voltage corresponding to each deflected state *U*(*A*). The maximum value in the voltage-displacement curve corresponds with the pull-in voltage U_{PI}.

Fig 9.9 shows the required voltage as function of the displacement of the central part of the cross-plate, calculated for the fabricated 2DOF shuffle motor.

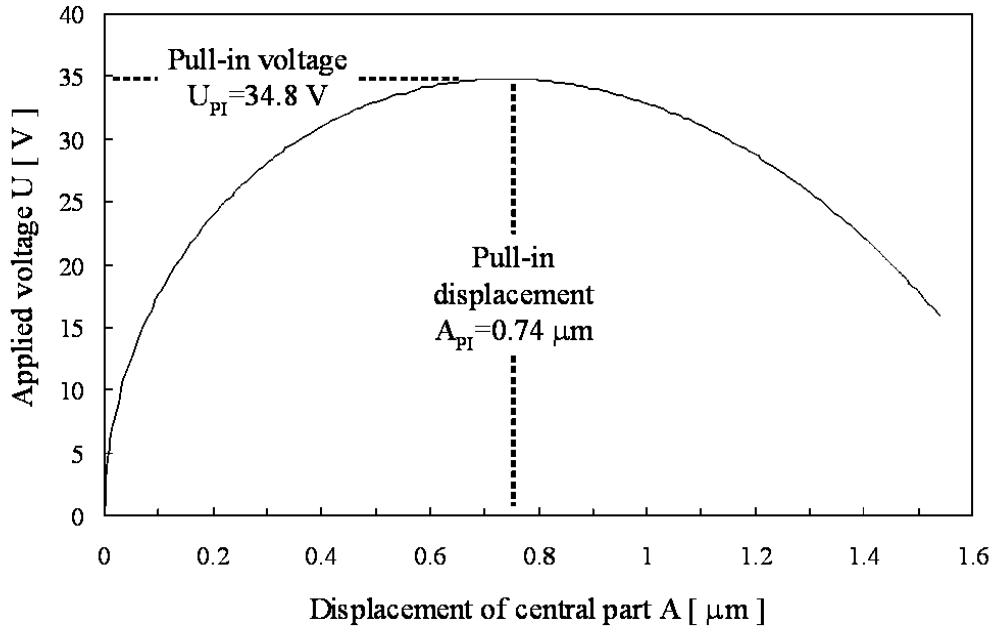

Figure 9.9: Calculated plate voltage as a function of the displacement of the central part of the cross plate.

The pull-in voltage of 34.8 V is calculated, corresponding with a displacement of the central part of 0.74 μm. The calculation is performed using the dimensions of the 2DOF shuffle motor given in Table 10.1. Young's modulus of polysilicon E of 160 GPa, air premittivity ε_o of 8.85 $\cdot 10^{12}$ and relative permittivity of silicon nitride insulating layer ε_r of 7.5 are used.

The step size of a shuffle motor can be approximated by the curvature shortening, discussed in Section 8.4.1. For an unloaded motor operating in the stable region, below the pull-in voltage U_{PI}, the longitudinal length reduction by contraction is expressed as:

$$\delta_f = \frac{\pi^2}{8}\frac{A^2}{L} \qquad (10.5)$$

Considering pull-in displacement of 0.74 μm, an expecting maximum step size for the fabricated 2DOF shuffle motor, operating bellow the pull-in instability, is around 8 nm.

When the applied voltage is equal or higher than the pull-in voltage ($U \geq U_{PI}$) the cross-plate snaps to the surface. The step size is than defined as (see Section 8.4.2):

$$\delta_c = \frac{\pi^2}{8} \frac{A_{\max}^2}{L_f} \tag{10.6}$$

where $A_{\max}$ is the maximum displacement of the central part, determined by the initial air gap g_a reduced for height of bumps b ($A_{\max}=g_a-b$). Free length L_f as a function of applied voltage can be calculated using the procedure explained in Section. 8.4.2. Employing this procedure we have calculated a step size from 44 nm to 62 nm for the fabricated 2DOF shuffle motor, operating above the pull-in voltage. The calculated step size corresponds with applied voltages from 35 V to 70 V.

9.6 MEASUREMENTS

The successful operation of the 2DOF shuffle motor is shown in Fig. 9.10.

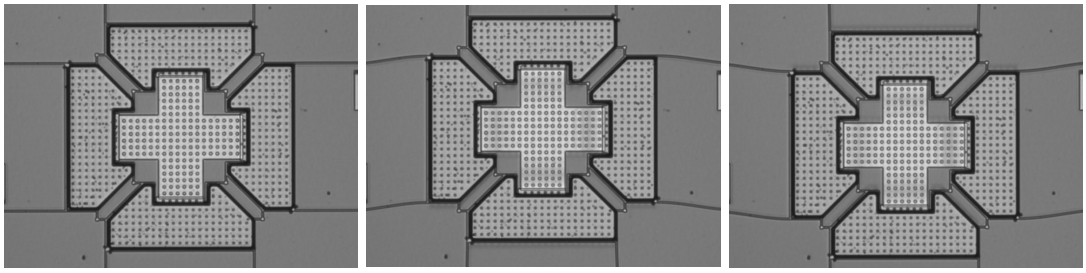

Table 9.10: Operation of a 2DOF shuffle motor: (left) at rest, (middle) moving up and (right) moving down.

An analog output card and a high voltage amplifier with high slew rate are used for generation of the required voltage sequences. Displacement of the motor is measured using video acquisition and an image processing technique [2]. This technique, based on the Fourier transform, allows in-plane sub-pixel displacement

measurements with a resolution of a few nanometers. Stepping motion in both X and Y directions was demonstrated, using the full, half and diagonal stepping modes. The maximum displacement range of the motor was limited to ± 30 μm by the design layout.

We have measured the displacement range of the 2DOF shuffle motor as a function of different actuation voltages on the clamps and cross-plate, ranging from 20 V to 36 V and 45 V to 50V, respectively. The motor was operated in the full stepping mode. The measured displacement range at a certain voltage level is related to the output force of the motor, using the calculated stiffness of the suspension. Since the motor works against six springs at the same time (an activated clamp shield two springs), the linear stiffness of six crab-lag flexures connected in parallel (34.38 N/m) was used.

The output force of the motor as a function of the driving voltage is shown in Fig. 9.11.

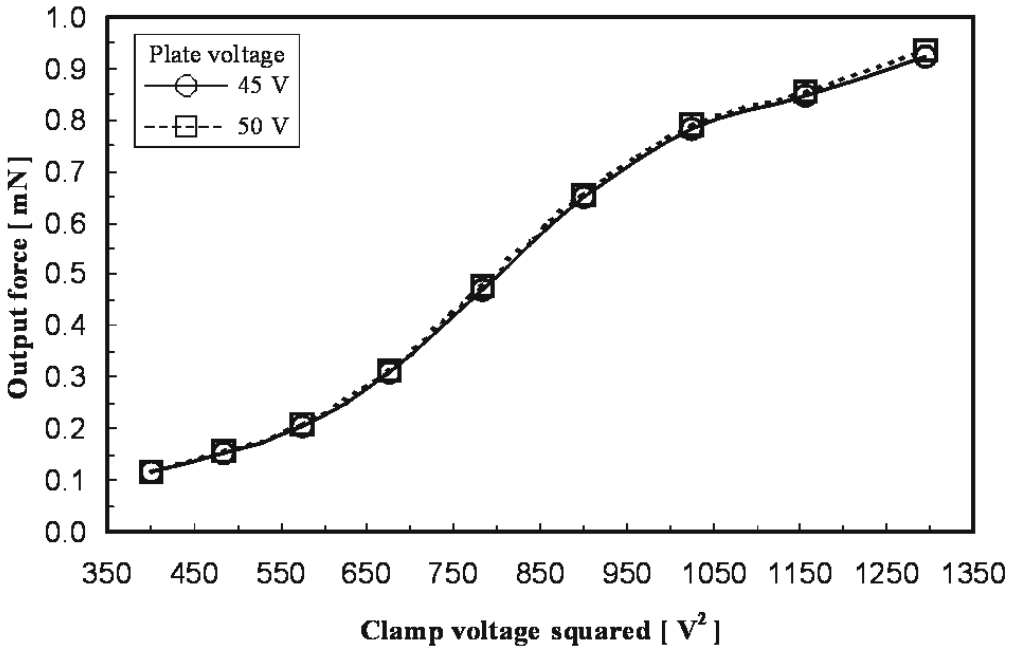

Figure 9.11: Output force determined from measured displacement of a 2DOF shuffle motor versus clamp voltage for different plate actuation voltages at cycle frequency of 200 Hz. The motor was driven in the full stepping mode.

The force increases with the clamp voltage squared, which is proportional to the normal force on the activated clamp. The maximum output force of 0.92 mN is measured using actuation voltages of 45 V on the plate and 36 V on the clamps. By increasing further the plate voltage to 50 V, the maximum output force was not altered.

The velocity of the motor as a function of the cycling frequency, measured for two stepping modes, is shown in Fig. 9.11.

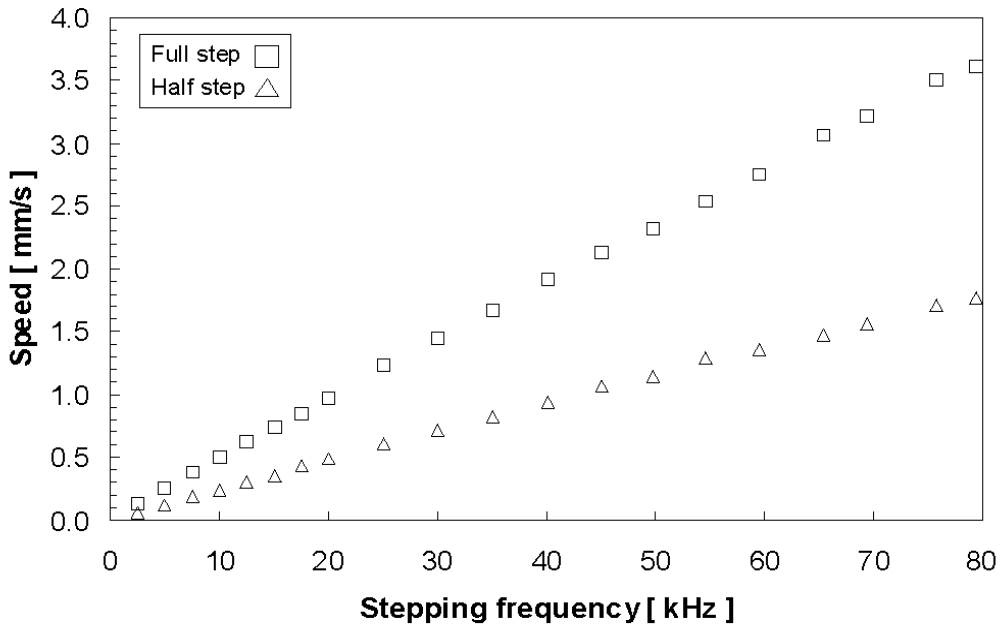

Figure 9.11: Measured speed of a 2DOF shuffle motor versus stepping frequency for full and half stepping modes. Measurement was performed at clamp and plate potentials of 45V.

The velocity measurements were performed on a motor operated with actuation voltage of 45 V, both on the plate and the clamps. The measurement curves show a fairly linear increase of the velocity with increasing cycling frequency in the measured frequency region. The maximum velocities of 3.6 mm/s (1.8 mm/s) were measured at the cycling frequency of 80 kHz. The maximum measured frequency of 80 kHz was limited by the available driving electronics. The slope of the curves

is a measure for the average step size, which is 48 nm for the full step mode and 23.5 nm for the half step mode. This is well within the predicted range.

The velocity of the 2DOF shuffle motor depends not only on the cycling frequency and the stepping mode but also on the average step size. The step size of the motor is a function of the degree of plate deformation, which is directly related to the plate actuation voltage, as shown in Fig. 9.12.

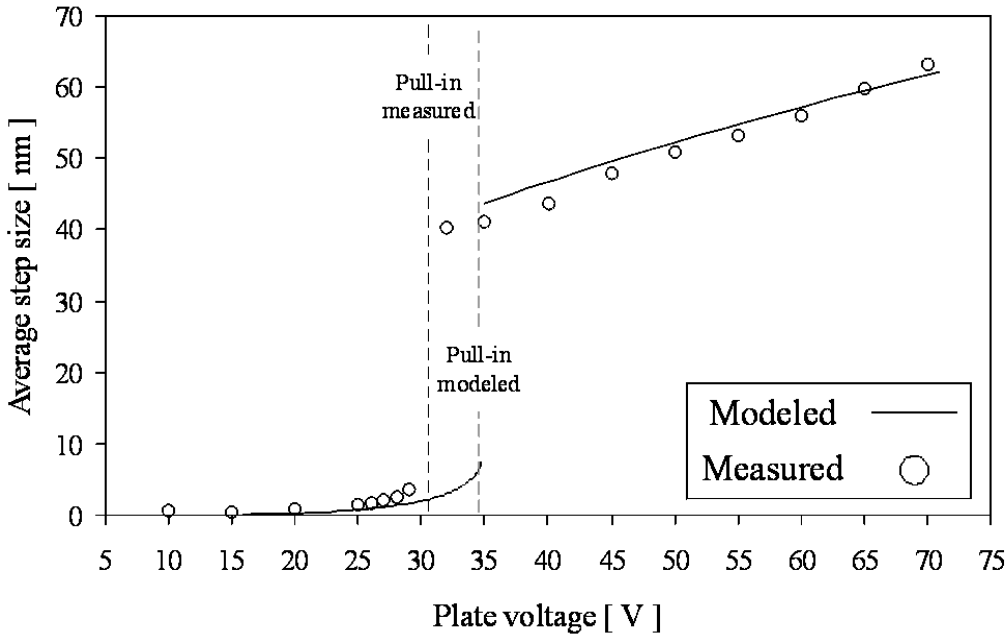

Figure 9.12: Measured average step size versus plate actuation voltage. Clamp voltage of 30 V and cycle frequency of 200 Hz are used. The motor was driven in the full stepping modes.

By applying a voltage difference between the plate and the substrate, normal deflection of the plate occurs, inducing an in-plane step. A higher actuation voltage causes a larger plate deformation, resulting in a larger step size. By increasing the actuation voltage above the pull-in instability, the electrostatic force between the plate and the substrate increases faster than the restoring mechanical force of the plate, resulting in the collapse of the plate on the substrate. This is associated with large deformation and significant increase in the step size, as shown in Fig. 9.12.

We found an average step size from 0.5 to 3.5 nm for the motor, operated below the pull-in voltage of the cross-plate. A pull-in voltage of 31 V was measured, which is in a relative good agreement with the model (34.8 V). By operating the plate above the pull-in, we have demonstrated adjustable nanometer-resolution steps ranging from 41 nm to 63 nm, corresponding to plate voltages between 32 V and 70 V. The measured step size for both operating ranges are in fair agreement with the theoretical prediction, as illustrated in Fig. 9.12.

It should be noted that the output force of the motor is related to the operating regime. A maximum output force of 0.14 mN was measured for the motor operating below the pull-in instability, which is roughly six times smaller than the maximum force above the pull-in (0.92 mN).

9.7 DISCUSSION AND CONCLUSIONS

In this chapter, we have proved the feasibility of an electrostatic linear stepper micromotor with two translational degrees of freedom. A simple model of the bending of a cross-plate is derived, giving a reasonable accurate prediction of the pull-in voltage and step size of the motor as function of the actuation voltage. We have demonstrated planar stepping motion in full, half and diagonal stepping modes at different stepping frequencies. The motor was driven in the frequency range up to 80 kHz, showing a fairly linear relation between the speed and stepping frequency. The motor was successfully operated below and above the pull-in instability of the cross-plate, resulting in the adjustable step size from 0.5 to 3.5 and from 41 nm to 63 nm, respectively. A relatively high output force of 0.92 mN was measured for the motor operating above the pull-in instability at 45 V on the cross-plate and 36 V on the clamps. The maximum displacement range of the motor was ±30 μm limited only by design layout.

Small size, large manoeuvrability and high performance characteristics in terms of speed, output force and positioning resolution makes this motor a promising candidate to perform positioning of the recording medium in probe-based data storage systems such as the micro Scanning Probe Array Memory (μSPAM).

Future work should determine positioning accuracy and coupling between motions in X and Y directions, which is primarily originating from the suspension,

we expect. Furthermore, one should consider fabricating a 2DOF shuffle motor with three in place of four clamps, which also allows a planar motion but reduces the complexity of driving signals.

9.8 REFERENCES

1 Bochobza-Degani O, Elata D and Nemirovsky Y 2002 An efficient DIPIE algorithm for CAD of electrostatically actuated MEMS devices *J. Microelectromech. Syst*. **11**(5) 612-620

2 Vanapalli S 2004 Techniques for characterization of in-plane displacement for microactuators *M.Sc Thesis* Department of Electrical Engineering, University of Twente, The Netherlands.

Chapter 10

Electrostatic contraction beams micromotor

Abstract

In this chapter, a novel electrostatic linear stepper micromotor is presented. The motor employs both a built-in mechanical transformation and a large number of contraction beams working in parallel to generate a large output force and high-resolution step. The motor is fabricated in a single polysilicon layer using vertical trench isolation technology. The entire motor, including the clamps and the contraction beams, fits in an area of 440 x 286 μm. Tests on the first prototype show an effective step size of 11 nm and a maximum generated force of 0.56 mN. Driving voltages of 45 V and 85 V are used for the clamping and contraction, respectively. A maximum displacement range of ±50 μm and speed of 0.6 mm/s are demonstrated.

10.1 INTRODUCTION

The shuffle motors presented in Chapter 8 and 9 employ deflection of an elastic plate toward the substrate to generate a single step and voltage-controlled clamps to achieve stepping motion. In this chapter, we present a novel electrostatic stepper micromotor, which also employs a built-in mechanical leverage to generate large output force and high-resolution step. In contrast to a shuffle motor, this motor employs an in-plane deflection of a large number of contraction beams working in parallel to generate a single motion step.

In the following sections, we present the working principle of the contraction beams motor and derive models to predict its performance characteristics. We prove the feasibility of step generation using a test contraction element with a large number of beams. As proof of principle, we demonstrate stepping motion of the motor and characterize its performance in terms of average step size, speed and output force.

10.2 CONTRACTION BEAMS MOTOR

A schematic view of a contraction beams micromotor and its operating sequence is depicted in Fig. 10.1. The design of the motor includes two electrostatic clamps and an electrostatic contraction element, which consists of a number of beams arranged in pairs. The beams are mechanically connected to the clamps but electrically insulated, allowing individual biasing of these components. In addition, the beams in each pair are mutually electrically insulated, allowing a pottential difference to be applied between them.

To create a single step, a voltage difference is first applied between the front clamp and the electrically grounded substrate, generating an electrostatic normal force (*A*). This force prevents sliding of the activated clamp by friction. A potential difference is then applied to the contraction element, deflecting the beams in each pair. Due to a built-in mechanical transformation, this lateral deflection induces a small but powerful longitudinal contraction, moving the clamps closer together (*B*). Next, the back clamp is activated in the new position (*C*) and the front clamp is released (*D*). The released beams stretch and push the front clamp forward (*E*). Finally, the front clamp is activated again (*F*) and one operational cycle is fully completed. The entire motor is moved by a single step. A

large stroke can be achieved by repeating the operational sequence. By reversing the sequence stepping motion in the opposite direction can be achieved without any additional complexity.

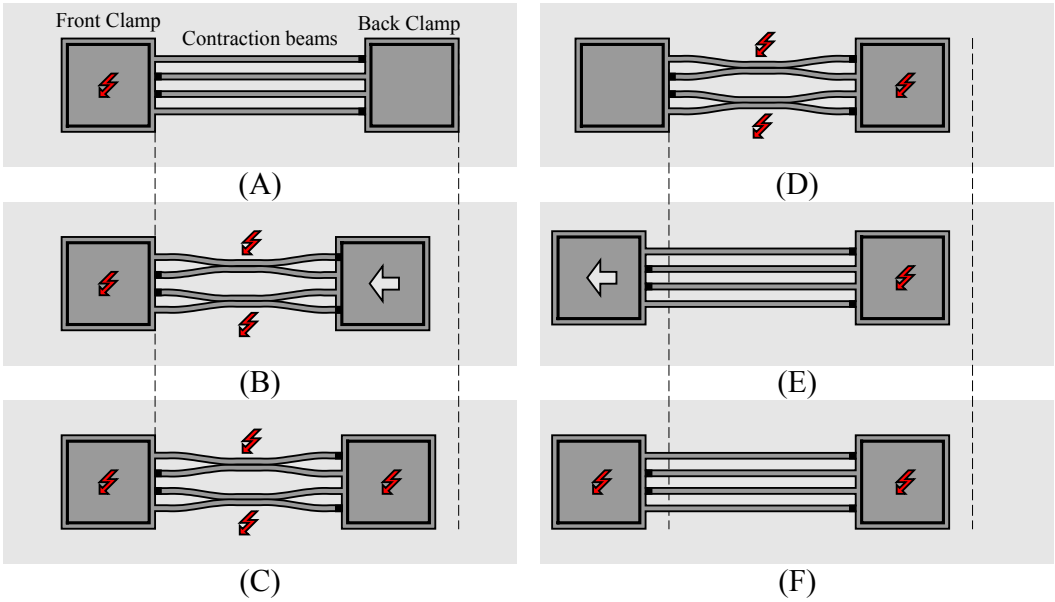

Figure 10.1: Actuation sequence of a contraction beams micromotor as seen from the top.

Step generation using pairs of beams with in-plane deflection has several advantages over single-plate deflection towards the substrate, which is used in a shuffle motor. First, an in-plane deflection does not generate a normal reaction force in a non-activated clamp (see Fig. 10.2). The reaction force induces an unwanted frictional force that opposes sliding motion of the clamp. Next, undesirable moment, which can significantly reduce the clamping force [1], is eliminated due to the symmetry. Furthermore, propulsion of the motor is decoupled from the substrate, allowing larger design freedom. Additionally, the motor has compelling scalability as the number of contraction beams operating in parallel can be chosen freely to obtain a desired output force. Finally, high-aspect-ratio contractions beams can be fabricated in monocrystalline silicon using bulk micromachining methods (see Section 4.4.4), which can result in a micromotor with a relatively high areal force density.

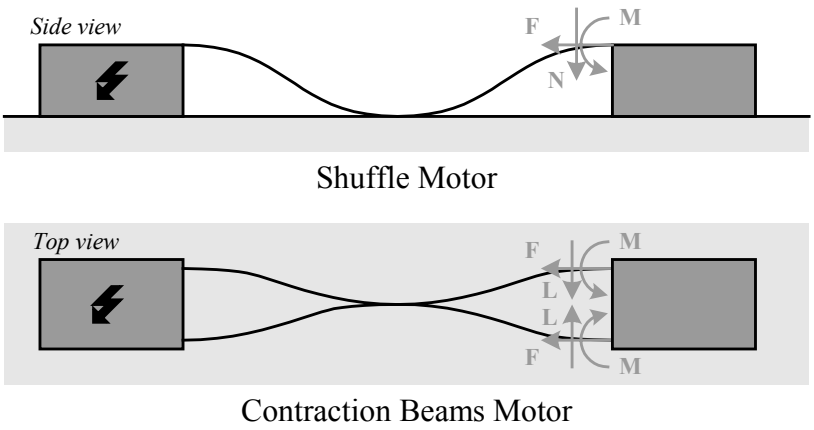

Figure 10.2: Schematic view of step generation in a shuffle motor and a contraction beams motor.

10.3 MODELLING

The step size and maximum output force of the contraction beams motor are primarily determined by the performance of the contraction element. A basic unit of the contraction element, shown in Fig. 10.3, is composed of a pair of conducting beams with length $2L$, width t and height h. The beams, separated by an air gap g_a, are electrically insulated, allowing individual biasing.

On application of the potential difference U an in-plane deflection of the beams occurs inducing a longitudinal displacement of the movable end δ. The magnitude of the longitudinal displacement can be approximated as the difference between the length of a deflected beam and the original length L (see section 8.4). A reasonable approximation of the beam deflection curve is given by the following function, which satisfies the boundary conditions:

$$y(x) = \frac{1}{2} A\left(1 - \cos\left(\frac{\pi x}{L}\right)\right) \qquad 0 \le x \le L \qquad (10.1)$$

where v is the center deflection of the plate.

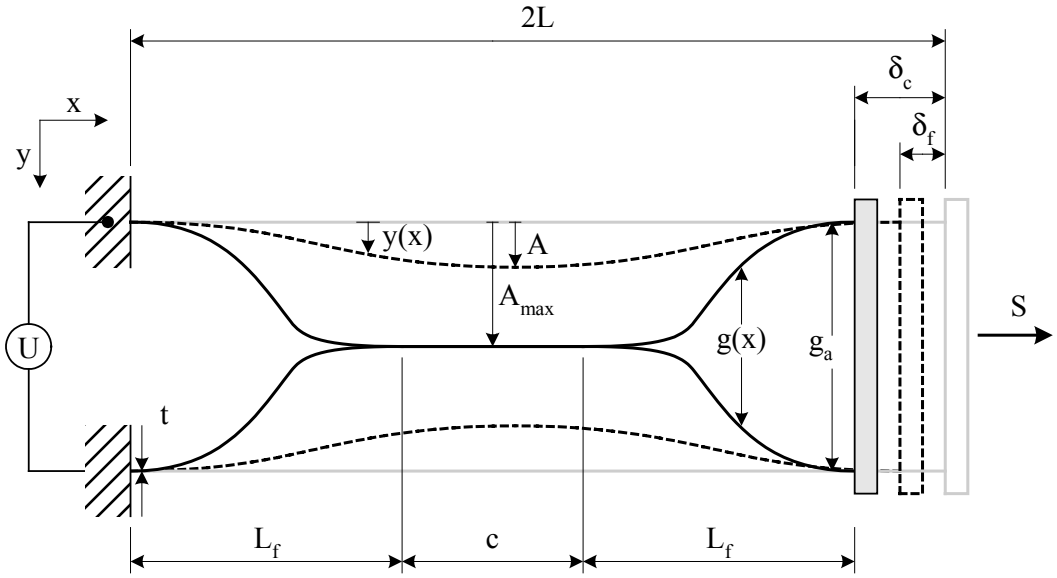

Figure 10.3:Physical model of a basic unit of the contraction element.

The longitudinal displacement of the motor, operating in the stable regime bellow the pull-in voltage, is (see section 8.4.1):

$$\delta_f = \frac{\pi^2}{8}\frac{v^2}{L} \tag{10.2}$$

When the actuation voltage equals or exceeds the pull-in voltage ($U \geq U_{PI}$) the beams are pulled together. A higher voltage increases the contact length c, providing a larger longitudinal displacement. The longitudinal contraction of the beams in contact can be estimated as (see section 8.4.2):

$$\delta_c = \frac{\pi^2}{8}\frac{A_{max}^2}{L_f} = \frac{\pi^2}{32}\frac{g_a^2}{L_f} \tag{10.3}$$

where $2L_f = 2L - c$ is length of the beam that is not in contact and A_{max} is the maximum displacement of the central part equal to half of the initial air gap g_a ($A_{max} = g_a/2$).

For typical dimensions of contraction beams L=200 μm and g_a=1.8 μm, a step size of 1.6 nm (12.5 nm) is calculated for a contraction element operating below

(above) the pull-in instability. The deflection of the beams at the midpoint and the contact length c are assumed to be 20 % of the initial gap g_a and 20 % of beam length L, respectively.

The maximum attainable force (force at zero displacement) is that required to elongate the beams an amount equal to the longitudinal contraction δ (see section 8.4.3):

$$S_{\max} = n\frac{EA}{2L}\delta \tag{10.4}$$

where n and E are the number of beams and the Young's modulus of the beams.

The generated force can be scaled up by increasing the number of beams working in parallel. For a contraction element with 16 polysilicon beams 200 μm long, 2 μm wide and 5 μm high, operating below (above) the pull-in voltage, an output force of 0.2 mN (1.6 mN) is expected. In this calculation a Young's modulus 160 GPa is used for the polysilicon beams.

An important design parameter for the proposed actuator is the pull-in voltage, the upper voltage limit beyond which the electrostatic attraction force between beams increases faster than the restoring elastic force causing instability and ultimately contact of the beams. The pull-in voltage U_{PI} for two parallel double-clamped beams can be expressed as [2]:

$$U_{PI} = \frac{1}{\sqrt{2}}\sqrt{0.75\frac{Et^3 g_a^3}{\varepsilon_0 L^4}} \tag{10.5}$$

where ε_o=8.85·10^{12} is permittivity of air. This predicts a pull-in voltage of 56 V for beams with dimensions used in the calculations of step size and output force above.

10.4 FABRICATION

A successful implementation of the contraction beams motor requires electrical insulation and mechanical interconnection between the clamps, contraction beams and between beams in each pair. We use vertical trench isolation in combination

with standard surface micromachining, introduced in Chapter 2, to satisfy these requirements. Vertical trench isolation employs trenches refilled with dielectric material to create insulation and interconnection between released microstructures in a single device layer.

The basic steps of a three-mask fabrication process of a contraction beams motor, are illustrated in Fig. 10.4. The fabrication process is started on a highly conductive silicon substrate that is coated with an LPCVD silicon nitride layer. On the coated substrate, a first silicon oxide layer is deposited using PECVD. In the first silicon oxide layer, molds for the clamp feet are patterned by BHF and subsequently covered with a second PECVD silicon oxide layer (*Step 1*). The thickness of the second silicon oxide layer determines the gap between released clamps and the coated substrate, and the aggregate thickens of the two silicon oxide layers determines the distance between the beams and the substrate. A large distance prevents the biased beams from being pulled into contact with the grounded substrate by electrostatic forces, assuring proper operation.

Subsequently, a thick LPCVD polysilicon layer is deposited on the patterned surface and heavily doped with boron (*Step 2*). The thickness of the polysilicon layer determines the height of all components. A thick layer assures mechanically stiff clamps and beams with high aspect ratio (height/width).

Next, isolating trenches with a slightly negative profile are etched in the polysilicon layer using deep reactive ion etching (DRIE) (*Step 3*). The etched trenches are completely refilled with an LPCVD low-stress silicon nitride layer. The silicon nitride layer is subsequently removed from the top by a maskless RIE (*Step 4*).

Subsequently, the layout of the motor is patterned in a second DRIE step. After structural etching, a short isotropic etch of the silicon oxide in BHF is performed to define molds for isolating bumps (*Step 5*). Hollow isolating bumps and silicon nitride sidewalls on the contraction beams to prevent short circuiting during operation are created by a thin nitride layer deposition followed by a maskless RIE etch step. Finally, the actuator is released with HF or BHF sacrificial silicon oxide etching (*Step 6*).

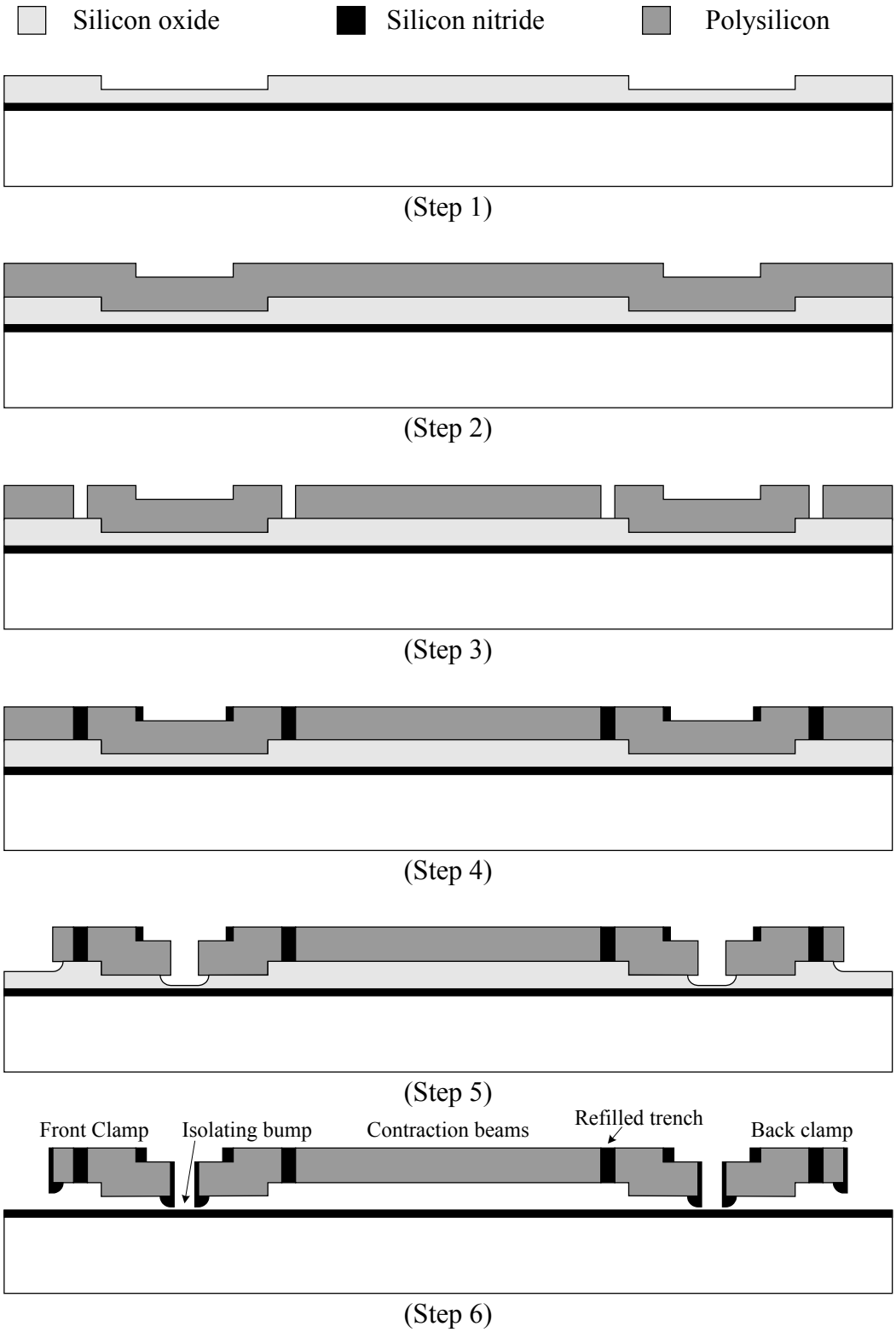

Figure 10.4: Fabrication sequence of a contraction beams motor.

The fabrication process is fully compatible with the one used for the manufacturing of the shuffle motors presented in Chapters 8 and 9. Fig. 10.5 shows a shuffle motor and a contraction beams motor realized in the same fabrication batch.

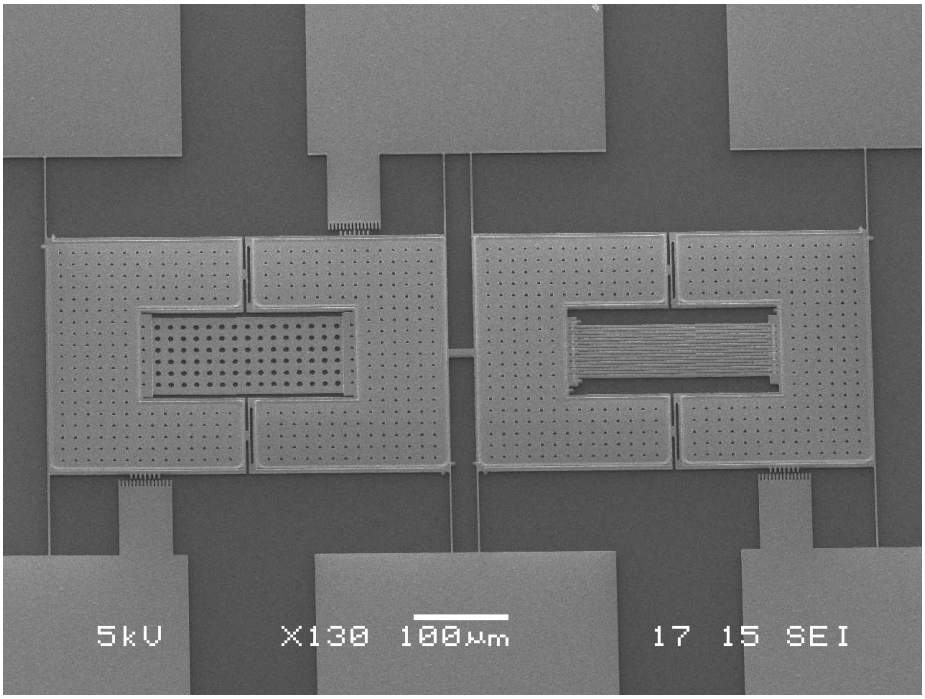

Figure 10.5: SEM micrograph a shuffle motor and a contraction beams motor fabricated in the same fabrication process.

10.5 RESULTS

Two different fabrication runs were performed. To demonstrate the feasibility of step generation, contraction elements with variable numbers of beams and gap sizes between beams were fabricated in the first run. In the second, two electrostatic clamps are added to the contraction element to achieve stepping motion.

10.5.1 Contraction element

Test contraction elements were fabricated in a highly doped, 5 µm thick polysilicon layer on top of a 2 µm thick sacrificial silicon oxide layer. The 2 µm width of the polysilicon contraction beams was limited by the available photolithographic resolution. The 100 nm thin LPCVD silicon nitride layer on

sidewalls was used to prevent short-circuiting between two beams at pull-in. Isolation trenches 2 μm wide and refilled with silicon nitride, provided electrical insulation between neighbouring beams, as shown in Fig. 10.6. Isolating trenches were arranged in such a way to insure proper electrical insulation between the beams in each pair, despite a potential mask misalignment.

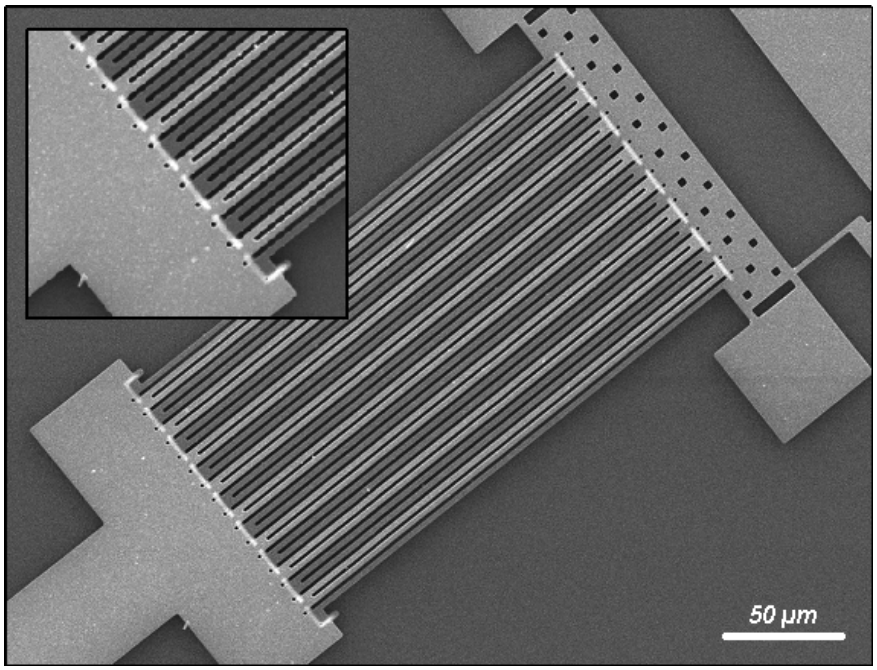

Figure 10.6: A test contraction element with 16 pairs of beams. Due to the charging during the SEM session distinct electrical domains, including refilled trenches, are clearly visible.

Contraction elements with different numbers of beam pairs (up to 16) were fabricated. The length of beams L ranged from 175 μm to 325 μm. The initial gap g_a between the beams was 1.8 μm, 2.3 μm and 3.3 μm. Contraction elements were operated in the unstable regime, above the pull-in voltage allowing, the beams to contact in order to increase the longitudinal displacement (see Fig. 10.7). A voltage higher than the pull-in voltage of an individual basic cell was applied to insure simultaneous operation of all basic cells in an actuator. The simultaneous operation of 16 pairs (32 beams) was registered. Actuators were operated with a harmonic voltage with amplitude from 30 V to 75 V, depending on the beam length and spacing.

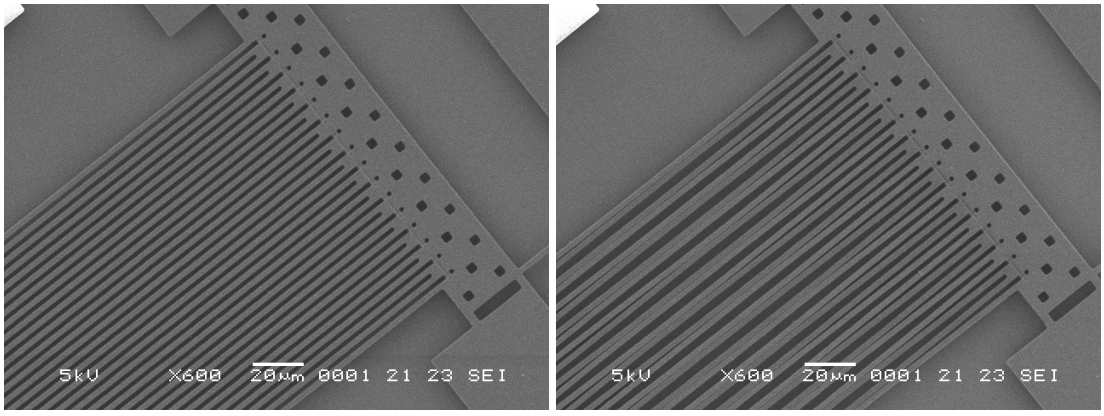

Figure 10.7: SEM micrographs of a contraction element with 16 beam pairs: (left) at zero voltage and (right) operated above the pull-in voltage at 70 V.

For operating voltages higher than 80 V we observed electric breakdown. Furthermore, the contraction beams longer than 250 µm were often sticking to each other, even after the actuation voltage was removed. Most reliable operation was observed for contraction beams from 200 µm to 250 µm long with a spacing of 1.8 µm.

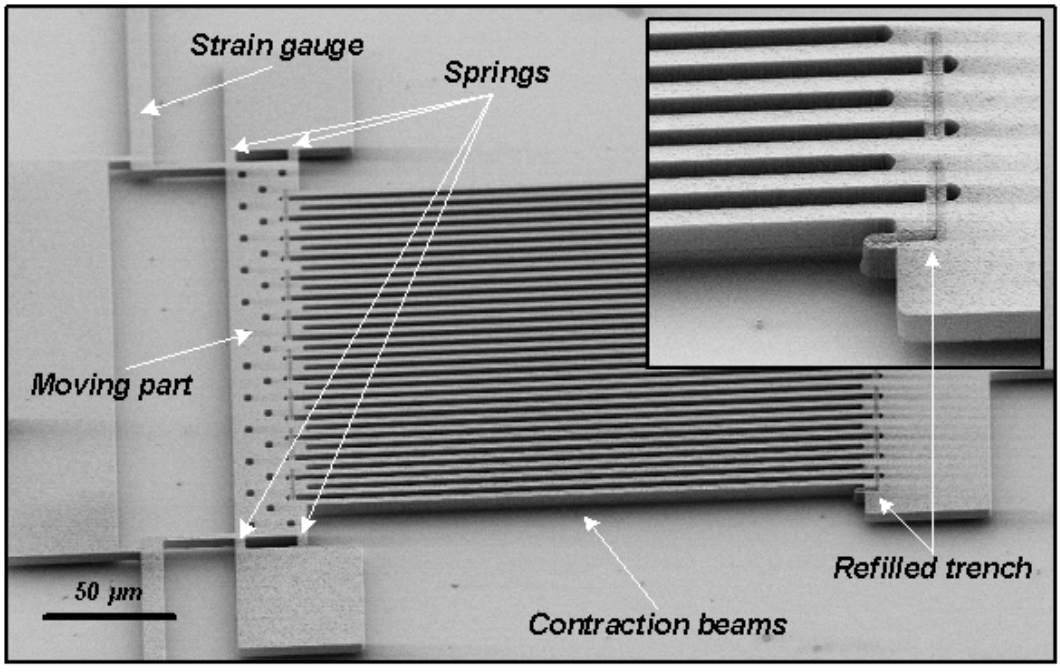

Figure 10.8: SEM micrograph a contraction element with a strain gauge attached to the movable end in order to observe the longitudinal contraction.

To observe a longitudinal displacement under an optical microscope, a strain gauge with a mechanical amplifier (40 x) was attached to the movable end of a contraction element (see Fig. 10. 8).

The movable end was suspended by springs of known dimensions in order to measure the output force. For an actuator containing 16 parallel beams, 2 μm wide, 200 μm long with 1.8 μm mutual distance between the beams, a maximum displacement of ~10 nm and an output force ~1 mN was estimated. To achieve the simultaneous operation of all beams, the actuation voltage (70 V) applied was higher than the pull-in voltage (57 V) measured for a single beam pair. The observed step size, output force and pull-in voltage were in the range predicted by modelling (see Section 10.3)

10.5.2 Stepping motion

In the second fabrication run, we added two electrostatic clamps to a contraction element to produce a stepper motor. A successfully fabricated actuator with all components is shown in Fig. 10.9.

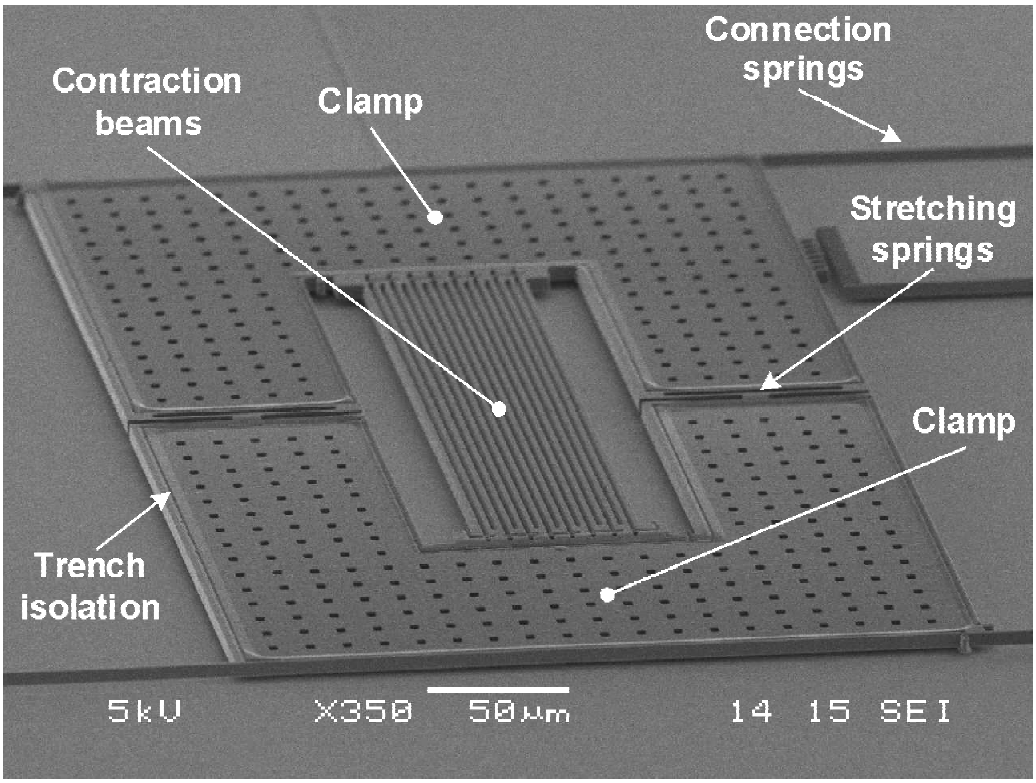

Figure 10.9: SEM micrograph a contraction beams motor with all components.

The moving parts of the motor consisted of two clamps and a contraction element. The entire motor was supported and guided by four springs, which also provided driving signals to the clamps and contraction element. It moves over the grounded silicon substrate, coated by a 210 nm silicon nitride layer. The completed motor fits in an area of 440 μm x 286 μm. The contraction element of the actuator contained 16 polysilicon beams, 212 μm long, 2 μm wide and 5.5 μm high. A 165 nm LPCVD silicon nitride layer was employed on the sidewalls of contraction beams to prevent short-circuiting at pull-in. The spacing between the neighbouring beams was 1.67 μm.

Isolation trenches, 2 μm wide, were refilled with a low-stress silicon nitride layer to assure the electrical isolation of beams, as shown in Fig. 10.10.

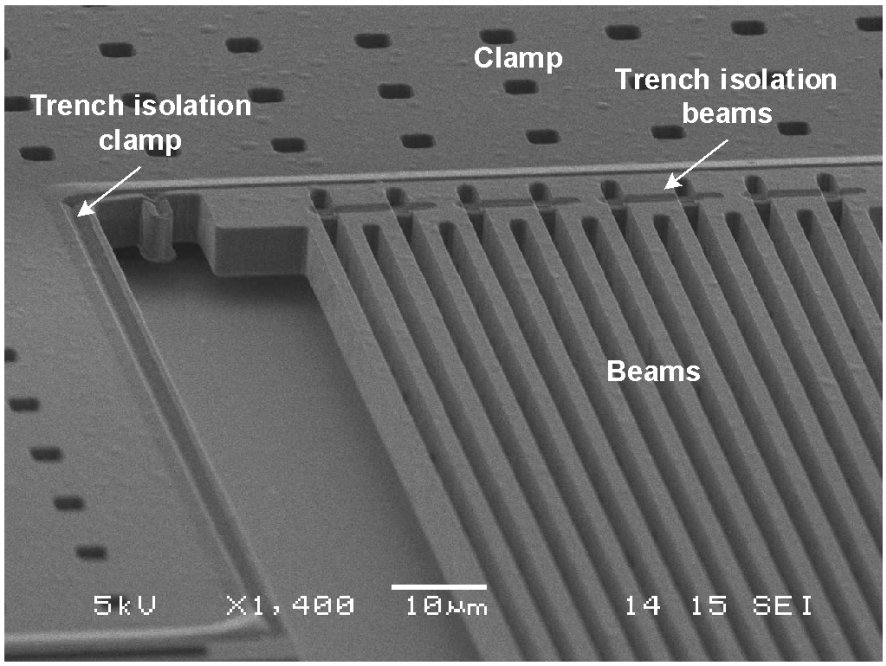

Figure 10.10: SEM micrograph of the connection between beams and a clamp.

The 210 nm gap between an activated clamp and the grounded substrate was determined by the height of isolating silicon nitride bumps evenly spaced on the back surface of the clamps. The isolating bumps, getting in contact with the silicon nitride coating on the substrate, reduce contact area between the clamps and the underground significantly preventing stiction during the fabrication and operation and limiting charge accumulation.

Bidirectional stepping motion of the actuator is successfully performed, as shown in Fig. 10.11.

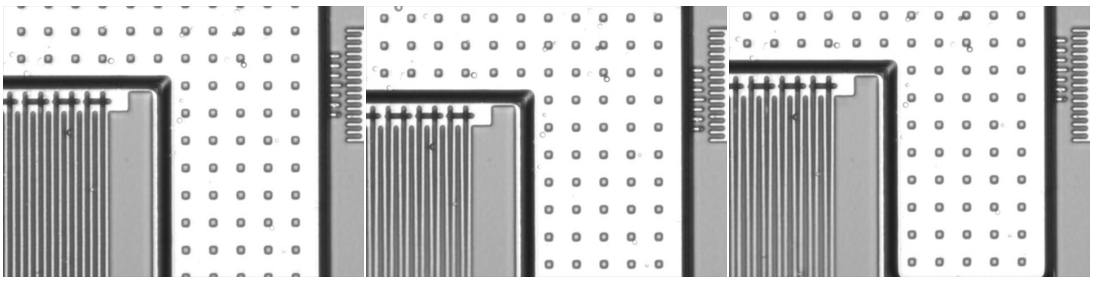

Table 10.11: Operation of a contraction beams motor: (left) initial position, (middle) motion down and (right) motion up.

In general, the displacement range of a contraction beam motor is only limited by the suspension. We demonstrated a maximum displacement range of ± 50 µm, using a compliant suspension. During motion experiments, the substrate and one half of the contraction beams were grounded. The tests were done using a voltage sequence shown in Fig. 10.12.

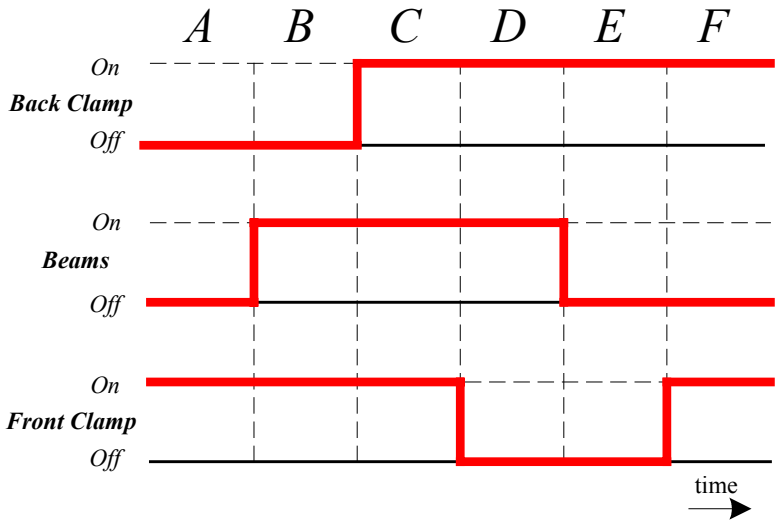

Figure 10.12: Voltage sequence applied to the motor to create stepping motion.

After each operation cycle, the polarity of the actuation voltage is reversed in order to reduce potential charge accumulation in the silicon nitride sidewalls of

beams and the silicon nitride coating on the substrate. The voltage sequence was generated using an analog output card and a high voltage amplifier with high slew rate.

Displacement of the motor is measured using an image processing technique with a resolution of few nanometers [3]. Fig. 10.13 shows typical measurement data.

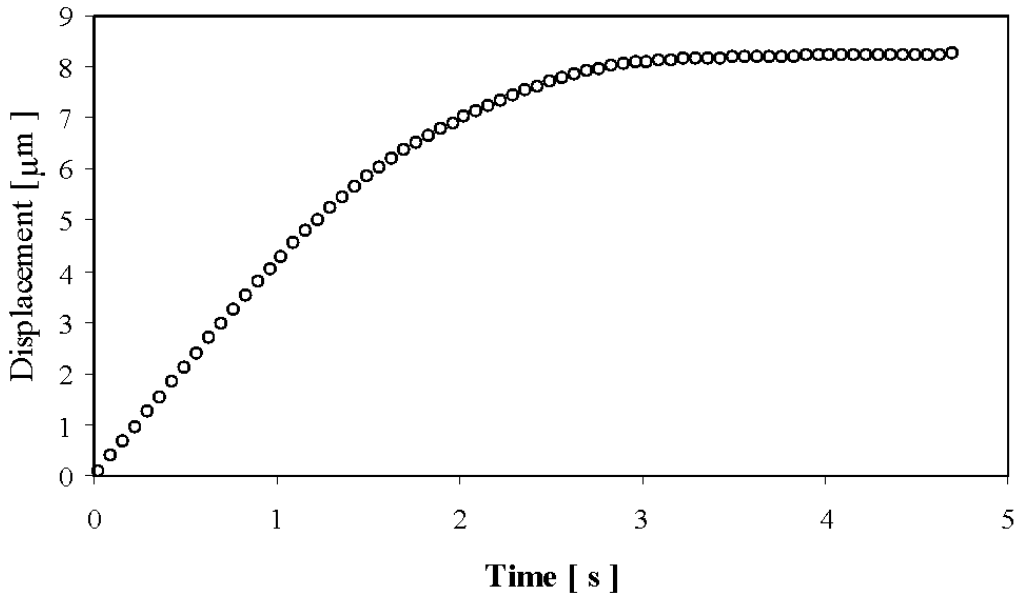

Figure 10.13: Displacement of a contraction beams motor versus time. Data were taken at cycling frequency of 500 Hz using beams and clamp potentials of 60V and 35 V respectively.

Fig. 10.14 shows the speed of the motor versus stepping frequency for different beam voltages (60 V and 75 V). We performed the speed measurements by operating the motor at a given frequency for a fixed number of steps (400 steps) and measuring the distance travelled. The speed is then calculated by dividing the travelled distance by the time of operation, derived from the cycling frequency and the number of steps. For each frequency, we took the average value of three measurements. The mean error for each measurement points was smaller than 0.9 %.

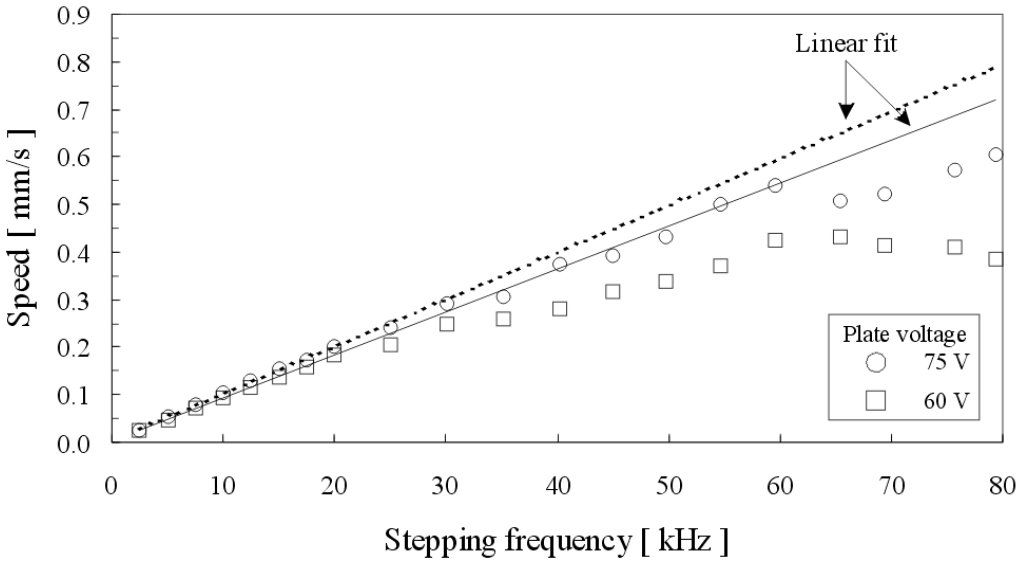

Figure 10.14: Measured speed of a contraction beams motor versus stepping frequency for beams potentials of 60 V and 75 V. Measurements were performed at a clamp potential of 45V.

The speed measurements for both actuation voltages have a well-behaved linear region below 20 kHz. The lines in Fig. 10.14 are a linear fit from this region, extended over the range of data. Above this region, a strong deviation from the linearity is observed. Considering the beam resonance frequency calculated to be more than 350 kHz, a considerable larger linear region was expected. The reason, we believe, is that the minimum time required to separate the beams in contact is limited due to adhesion forces. Therefore, the contraction beams, operated at frequencies above 20 kHz, remain continuously in contact. The stepping motion of the motor at these operating frequencies is generated by changing the contact length between the beams, instead of their snapping from the stretched position, resulting in a smaller effective step size. This can explain that the speed of the motor increases further with frequency at lower rate. Further investigation is required to confirm this assumption. A maximum speed of 0.6 mm/s at a cycling frequency of 80 kHz and the beam voltage of 75 V was measured.

The slope of the speed curves is a measure of the step size, which increases with beam voltage. An average step size as a function of the beam voltage is given in Fig. 10.15.

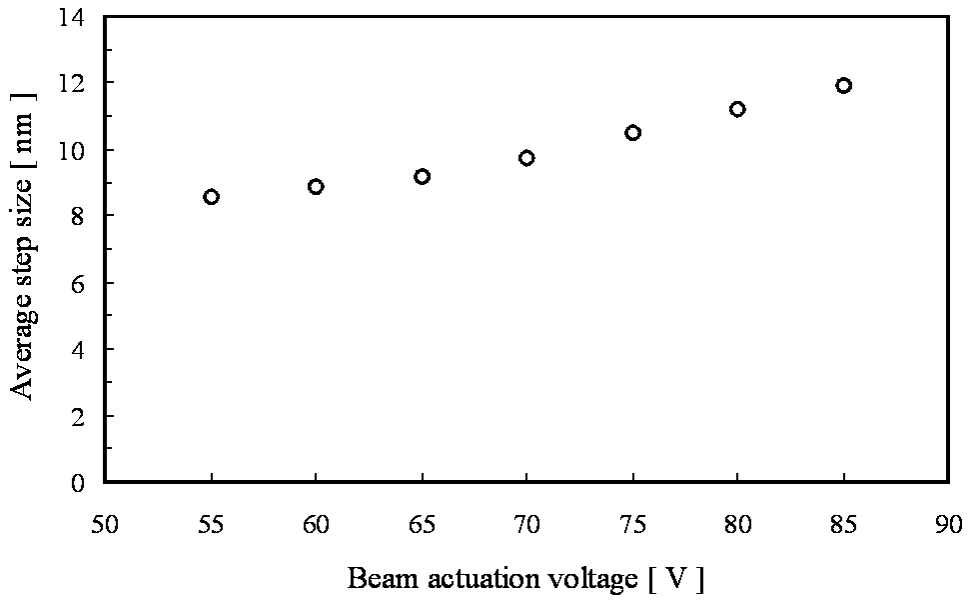

Figure 10.15: Average step size of the contraction beams motor versus the beam actuation voltage. Measurements were performed at stepping frequency of 200 Hz using a clamping voltage of 45 V.

The measurements of the step size were performed at the motor operating above the pull-in instability at 53 V. For reasons yet unclear no motion was observed when the actuator was operated below pull-in. The average step size ranges from 9 nm to 12 nm for voltages of 55 V to 85 V. The measured step size is in a reasonable agreement with a theoretically predicted step of ~10 nm.

Using in-plane displacement measurements and calculated stiffness of the suspension, we have determined the output force of the contraction beams motor. Data were taken on a motor with a rather stiff suspension in order to allow force measurements over a wide range of output forces. Fig. 10.16 shows the output force as a function of the clamp voltage with beams actuated from 60 V to 85 V.

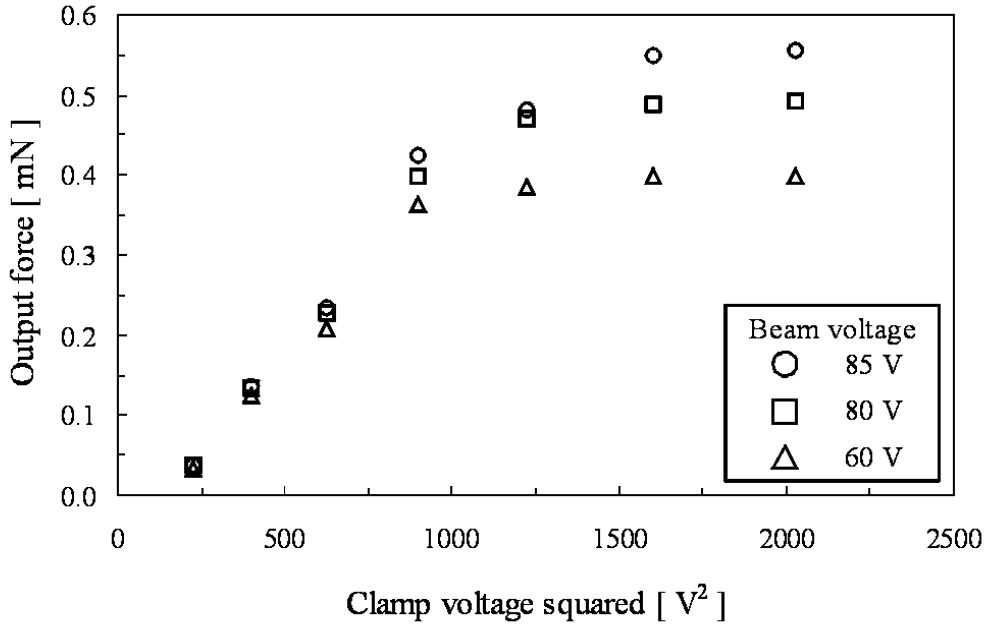

Figure 10.16: Measured output force of a contraction beams motor versus clamp voltage for different plate actuation voltage. Data were taken at a stepping frequency of 500 Hz.

The force graph indicates that for clamp voltages from 15 V to 30 V, the clamping force limits the output force of the motor. Above this region, the output force increases with beam voltage. A maximum output force of 0.56 mN is measured using actuation voltages of 85 V on the beams and 45 V on the clamps.

10.6 CONCLUSIONS

We have presented a novel electrostatic linear stepper micromotor, which employs both a built-in mechanical leverage and a contraction element consisting of large number of beams working in parallel, to achieve a relatively large output force and a high positioning resolution. We have successfully demonstrated stepping motion, generating a large stroke of ±50 μm. The motor was driven in a broad stepping frequency range, showing a linear increase of the speed with frequency in the range of 0 Hz to 20 kHz. We have measured a relatively high force of 0.56 mN at 85 V on the beams and 45 V on the clamps.

10.7 References

1 de Boer M P, Redmond J M and Michalske T A 1998 A hinged-pad test structure for sliding friction measurements in micromachining *SPIE proceeding v.3512, Materials and device characterization in micromachining* (Santa Clara, USA) 241-250

2 Sarajlic E, Berenschot E, Krijnen G and Elwenspoek M 2003 Low volume, large force (>1mN) and nanometer resolution, electrostatic microactuator for low displacement applications *Nanotechnology Conference and Trade Show* (NANOTECH 2003) (San Francisco, USA) **1** 637-640

3 Vanapalli S 2004 Techniques for characterization of in-plane displacement for microactuators *M.Sc Thesis* Department of Electrical Engineering, University of Twente, The Netherlands

Chapter 11

Conclusions and future prospects

Abstract

In this final chapter, we summarize the work presented in this thesis and give general conclusions and recommendations for future work.

11.1 OVERVIEW

This thesis focused on the development of microactuators and micromachining methods for their fabrication. The aim was to produce small microactuators (<1 mm^2), with large output force (mN range) and stroke (hundreds of μm), good positioning resolution (nm range) and speed (mm/s range) at low power consumption. There are numerous possible applications of microactuators with such performance characteristics, including data storage, microassembly, microscopy, robotics and optical systems. The performance goals for our microactuators were motivated by their potential use in a magnetic memory based on scanning probe technology, the micro Scanning Probe Array Memory (μSPAM).

We have concentrated on *electrostatic linear stepper micromotors with built-in mechanical leverage* as potential candidates to satisfy demanding target specifications of the μSPAM. Due to its favorable scaling properties, electrostatic actuation allows large energy density, fast response and low power consumption at the micron scale. Deflection of an elastic plate (beam) by electrostatic force is employed to generate a longitudinal contraction of the motors. Since this deflection is much larger than the induced contraction there is a built-in mechanical leverage, resulting in a powerful, high-resolution step. A voltage controlled clamping mechanism is employed to add small steps in sequence, creating large displacements, limited only by the dimension of the guidance.

We devised and presented three different electrostatic linear stepper micromotors: a shuffle motor, a 2DOF shuffle motor and a contraction beams micromotor.

The shuffle motor, measuring 412 μm x 286 μm, achieved a travel range of ± 70 μm. Depending on the plate actuation voltage, two operation modes were demonstrated with adjustable step sizes from 0.6 to 7 nm and 49 to 62 nm. The motor was operated up to a cycling frequency of 80 kHz, which was limited only by the driving electronics. Output forces of 1.7 mN were measured at 55 V for both the clamping and propulsion. The motor has travelled a cumulative distance of more than 1500 m in 34 billion steps without observable deterioration in

performance. The motor achieved the highest force and power densities published so far for electrostatic microactuators

The operation of existing shuffle motors was limited to bidirectional motion along a single axis, whereas implementation of the μSPAM concept requires planar motion. We designed and fabricated the first electrostatic shuffle motor with two translational degrees of freedom, a 2DOF shuffle motor. This compact motor (482 μm x 482 μm) was successfully operated below and above the pull-in instability of the actuation plate, resulting in adjustable step sizes from 0.5 to 3.5 and from 41 nm to 63 nm, respectively. By adjustment of the actuation sequence we have demonstrated planar stepping motion in full, half and diagonal stepping modes at different stepping frequencies. The motor was driven in the frequency range up to 80 kHz, showing a fairly linear relation between speed and stepping frequency in different stepping modes. A relatively high output force of 0.92 mN was measured for the motor operating above the pull-in instability at 45 V on the cross-plate and 36 V on the clamps. The maximum displacement range of the motor was ± 30 μm for both in-plane directions, limited only by design layout.

Normal deflection of a plate towards the substrate, used in shuffle motors to generate steps, induces an unwanted frictional force in the inactivated clamp that opposes sliding motion and generates a moment in the activated clamp that reduces the clamping force. To eliminate these undesirable effects, we designed and successfully fabricated a novel electrostatic contraction beams micromotor, which employed in-plane deflection of a large number of beams working in parallel to generate a high-resolution step and large force. The motor has compelling scalability as the number of contraction beams operating in parallel can be chosen freely to obtain a desired output force. The entire motor, including its clamps and 16 contraction beams, fit in an area of 440 μm x 286 μm. Tests on the first prototype showed an effective step size of 11 nm and a maximum output force of 0.56 mN. Driving voltages of 45 V and 85 V were used for the clamping and propulsion, respectively. A maximum displacement range of ±50 μm and speed of 0.6 mm/s were demonstrated.

Successful operation of these motors and electrostatic microactuators in general requires proper electrical insulation between mechanically connected components. The widely accepted surface micromachining approach uses stacks of

many dielectric and conductive layers connected by vertical conduction paths. We made a radical departure from this by employing *vertical trench isolation*. This technique utilizes trenches refilled with dielectric material to create electrical insulation between mechanically joined components in a single conductive layer. In this way, distinct electrical domains can be defined on both fixed and movable parts, allowing a large freedom of design. In this thesis we extensively explored the use of vertical trench isolation in both surface and bulk micromachining.

First, we described the use of vertical trench isolation in surface and SOI-based micromachining for the fabrication of electrostatic microactuators. We created new design opportunities by adding extra features, such as isolating structures and bumps, to the basic trench isolation process. The trench isolation technology complemented with the abovementioned features is a powerful platform for microactuator fabrication. In addition to its potential for simplifying fabrication and improving performance of existing devices, this technology allows design of new types of microactuators, as successfully demonstrated.

Furthermore, we developed a bulk micromachining process for fabrication of single-crystal, high-aspect-ratio microstructures in a standard silicon wafer by combining vertical trench isolation with plasma release. A significant advantage of this process is that etching, passivation and release of microstructures take place in a single plasma system during one etch run. This bulk micromachining technology is an attractive platform for both fabrication and rapid prototyping of micromechanical devices. This is due to its short processing time, large freedom of design, process flexibility, and low-cost of the starting standard silicon substrate relative to SOI substrates. Several example microstructures demonstrating the capabilities of this technology were successfully fabricated.

Despite the many advantages of this technology, there are also some drawbacks, which are directly associated with the use of the isotropic plasma etching to release the microstructure. A mesh-like design is required to release large area microstructures, which makes the technology less suitable for applications that require micromechanical structures with a large non-perforated area e.g. in data storage to maximize the effective recording area. We introduced a bulk micromachining technology, based on standard single crystal silicon wafers, which combines backside etching with vertical trench isolation. Backside etching

permits a dry release of high-aspect-ratio microstructures with a large non-perforated area. Vertical trench isolation ensures electrical insulation of microstructures from the bulk material, and also between mechanically linked movable microstructures with flexible or rigid connections. Electrostatic XY-scanners driven by comb drive actuators with a large non-perforated central shuttle were successfully fabricated using this technology.

Subsequently, we presented another bulk micromachining technology, based on vertical trench isolation, for fabrication of two-level MEMS in a standard monocrystalline silicon substrate. This technology employs double-sided processing to completely release micromechanical structures machined in the bulk silicon. Etching and release of microstructures are performed in a single plasma chamber allowing dry, low temperature processing. Utilizing double-side release, high-aspect-ratio monocrystalline MEMS with integrated vertical electrical insulation were fabricated on one side of the wafer and, at the same time, mechanically and electrically coupled with released micromechanical structures on the opposite side. This opens new design opportunities to improve performance and functionality of MEMS devices. As proof of principle, this technology was employed for fabrication of an electrostatic two-level XY-scanner with a significantly larger effective recording area.

Microfabrication techniques based on vertical trench isolation require at least two distinct patterning steps, one to define trench isolation and a second to pattern the structural layout. We introduced a refill method based on conformal deposition and isotropic removal that allows selective refill of isolating trenches with a combination of a dielectric and a poorly conducting material. The selective refill method replaces two previously required patterning steps with one, enabling single-mask fabrication of high-aspect-ratio monocrystalline MEMS with integrated vertical trench isolation on both standard silicon and SOI substrates.

The selective trench refill method employs isotropic etching to remove a layer of material conformally deposited on a patterned surface. When the isotropic etch clears the deposited material from planar surfaces, a portion of the material remains in the concave corners. We exploited this etching artifact to controllably form nanometer scale structures in three dimensions (3D) with well-defined position and orientation. Advantages of this new top-down approach to the

fabrication of 3-D nanostructures include process simplicity, compatibility with conventional micromachining, straightforward use of photolithography, and the ability to fabricate three-dimensional structures in a wide range of materials. The resulting structures are addressable by other functional components, such as bond pads, cantilever beams, membranes and bridges, complex spring constructions, microactuators and sensors, etc.

1.2 GENERAL CONCLUSIONS AND OUTLOOK

The electrostatic linear stepper micromotors for positioning of a recording medium in the micro Scanning Probe Array Memory have been devised, fabricated and operated. The required specifications for small size (< 1 mm^2), high output force (> 1 mN), large stroke (> 100 μm), good positioning resolution (< 100 nm) and high read/write speeds (> 1 mm/s) have successfully been fulfilled. The feasibility of stepping motion along two axes, required in the μSPAM, was demonstrated with success. The requirement for seek speed of 40 mm/s was the only one not reached by the fabricated motors. We believe that these speed ranges should be achievable by improving the driving electronics and optimising the motor design.

In this thesis we derived the quasi-static models to determine the required driving voltage and to predict the average step size and maximum output force performance of the fabricated micromotors. To further improve our understanding of these motors an appropriate dynamic model of the mechanical response to an applied voltage sequence is required. This will allow for an investigation of the influence of various parameters on the performance of the motors, allowing design optimization. While speed is an obvious goal in optimization, one should also strive to decrease the actuation voltages to within the voltage range of standard integrated control electronics, which is limited to approximately 15 V for CMOS technology. This would simplify the driving electronics and allow their on-chip integration, permitting higher cycling frequencies and thereby increasing the micromotors speeds.

The fabricated prototypes of the motors should be used not only to validate the derived models but also to improve their accuracy by collecting experimental data. Friction studies are particularly important, as the clamping action in the motors is based on frictional forces. Experimental investigations of friction, which are

necessary due to lack of accurate friction modeling in the micro domain, will lead to better understanding of friction and wear at this scale, resulting in further improvement of the performance and reliability of stepper micromotors.

During the course of research new microfabrication methods, based on vertical trench isolation, were developed, allowing fabrication of high-aspect-ratio monocrystalline MEMS with integrated electrical insulation on both fixed and movable parts. These methods open new design opportunities for fabrication of electrostatic microscanners for positioning of the recording medium in the μSPAM.

Microscanners with an integrated medium sled that completely covers the scanner area can be realized by the micromachining technology presented in Chapter 5. By hiding microscanners beneath a medium sled, a large area otherwise required for the driving components of the scanner (microactuators and flexure suspension) can be efficiently used for data storage. This allows further miniaturization of the medium scanners, and thereby an increase in speed, without compromising recording area efficiency. In this way, a large number of fast medium scanners with a large recording area, required in the μSPAM, could be fabricated Furthermore, the electrostatic scanners reside beneath the recording medium, preventing a potentially harmful interaction between the microactuators and micromechanical probes used for recording. The microscanners can be operated by diverse laterally driven microactuators, including electrostatic comb drive actuators and linear stepper motors [1]. Alternatively, the electrostatic contraction beams motor, devised in this thesis, may be employed. Its successful implementation would require an in-plane clamping mechanism. Due to the increase beam height, achievable in this technology, an increase in the output force and power densities is expected.

11.3 REFERENCES

1 Yeh R, Hollar S and Pister K S J 2002 Single mask, large force and large displacement electrostatic linear inchworm motors *J. Microelectormech. Syst.* **11**(4) 330-336

APPENDIX A

Table A.1: Micromachined electrostatic linear micromotors with large output force.

Authors	Akiyama et. al. 1996	Li et. al. 2002	Yeh et. al. 2002	Tas et. al. 1998	de Boer et. al. 2004	Sarajlic et. al. Chapter 8	Sarajlic et. al. Chapter 9	Sarajlic et. al. Chapter 10
Type of motor	Scratch Drive	Scratch Drive	GCA Inchworm	Shuffle Motor	Shuffle Motor	Shuffle Motor	2D Shuffle Motor	Contraction Beams Motor
Dimensions [µm x µm]	60 x 75	60 x 75	2500 x 1500	560 x 400	1500 x 200	412 x 286	482 x 482	440 x 286
Output force [mN]	0.063	0.25	0.26	0.043	0.45	1.7	0.92	1.7
Travel range [µm]	100	60	80	43	200	140	60	100
Speed [mm/s]	0.008	0.25	4	0.1	3	3.6	3.6	0.6
Frequency range [kHz]	0.1	10	1	1.16	80	80	80	80
Step size [nm]	80	25	4000	86	38	45	45	8
Driving voltage[1] [V]	112 (_)	200 (_)	33 (33)	40 (25)	150 (65)	55 (55)	36 (45)	45 (85)
Force density[2] [N/(m^{3}V^2)]	2232	2778	159	363	260	9651	4829	2107
Power density[2] [W/m^3]	2.24 x 10^2	2.78 x 10^4	6.93 x 10^2	3.84 x 10^1	9.00 x 10^3	1.05 x 10^5	2.85 x 10^4	5.39 x 10^3

[1] Clamping voltage (Propulsion voltage) *[2] Volume includes substrate thickness of 500 µm*

REFERENCES

1 Tas N, Wissink J, Sander L, Lammerink T and Elwenspoek M 1998 Modeling, design and testing of the electrostatic shuffle motor *Sensors and Actuators* A **70** 171-178

2 de Boer M P, Luck D L, Ashurst W R, Maboudian R, Corwin A D, Walraven J A, Redmond J M 2004 High performance surface-micromachined inchworm actuator *J. Microelectormech. Syst.* 13 63-74

3 Akiyama T, Collard D and Fujita H 1997 Scratch drive actuator with mechanical links for self-assembly of three-dimensional MEMS *J. Microelectormech. Syst.* **6**(1) 10-17

4 Li L, Brown G and Uttamchandani 2002 Study of scratch drive actuator force characteristics *J. Micromech. Microeng.* **12** 736-741

5 Yeh R, Hollar S and Pister K S J 2002 Single mask, large force and large displacement electrostatic linear inchworm motors *J. Microelectormech. Syst.* **11**(4) 330-336

ACKNOWLEDGMENTS

The research presented in this thesis is the result of work carried out in the Transducers Science and Technology Group within micro Scanning Probe Array Memory (μSPAM) project. Completing this thesis would not have been possible without the support and assistance of many people. Hereby I wish to thank all who contributed in some way to this work.

First and foremost I would like to thank my supervisor Gijs Krijnen for his guidance, insights and critical reviewing of my manuscripts and thesis. I am grateful to him for his encouragement and support during the long period of thesis writing.

Furthermore, I acknowledge my advisor, professor Miko Elwenspoek, for creating an inspiring and creative atmosphere within the group. I have particularly enjoyed a freedom granted to me in conducting this research. I thank him for his confidence and trust.

A special word of thanks to Leon Abelmann for organizing and managing the μSPAM project. I am thankful for his enthusiasm and the unforgettable workshop at IBM in Zurich. Also, I thank other μSPAM-ers, in particular Mihai, Alexander, Martin and Stefano.

I am grateful to Erwin Berenschot, Meint de Boer and Henri Jansen for their tremendous contribution in development and implementation of the microfabrication methods presented in this thesis. Some of the most pleasant moments in the past years were our discussions on microtechnology and time that we spent in the clean room realizing our ideas.

I thank Niels Tas and Toon Kuijpers for many discussions on micromotors, and Remco Sanders and Theo Lammerink for their contribution to the measurements. Furthermore, I am grateful to the students that have contributed to this research: Mink Hoexum and Srinivas Vanapalli.

The staff of the MESA+ clean room, Peter, Huib, Gerard, Marion, Samantha, Hans, Bert, Eddy and Marc, were extremely helpful and supportive during fabrication.

A portion of the research, presented in this thesis, was performed at Fujita Lab, University of Tokyo, Japan. I gratefully acknowledge all lab members there. I

would like to thank professor Fujita in particular for his kindness and financial support during my stay in Tokyo.
I thank all my current and former colleges from the micromechanics group for a pleasant and enjoyable time: Alex, Boudewijn, Dannis, Deladi, Dennis, Dick, Doekle, Duy, Florian, Fran, Hanh, Henk van Wolferen, Henk Wensink, Hien, Imran, Ingrid, Jeroen, John, Joost, Judith, Kees, Laura, Luis, Marcel, Marco, Philip, Remco Wiegerink, Rik de Zager, Roald, Saravanan, Satya, Sim, Vitaly.
I want to acknowledge my sister Edina Sarajlic and Nate Gemelke, both from Stanford University, USA, for reading the thesis and correcting my English.
Finally, I would like to express my gratitude to my wife Aida Hadzibeganovic for her unconditional support and encouragement and my daughter Lamia Sarajlic for her smile.

BIOGRAPHY

Edin Sarajlic has received his M.Sc. degree (Cum Laude) in Mechanical Engineering in May 2001 from the University of Twente, The Netherlands. His M.Sc. thesis '*Interior radiation modes - numerical and experimental approach*' dealt with active acoustic structural control. The M.Sc. thesis was a result of the research carried out at the Anti-Noise Department of the TNO Institute of Applied Physics (TNO-TPD) in Delft, The Netherlands. Since May 2001, he joined the Transducer Science Technology Group, MESA+ Research Institute, University of Twente, The Netherlands as doctoral student, working on electrostatic microactuators within Micro Scanning Probe Array Memory (μSPAM) project.